Mémoire d'Habilitation à Diriger des Recherches

"ETUDE DE LA MICROSTRUCTURE ET DES PHENOMENES DE TRANSPORT DANS LES POLYMERES A HAUTES PERFORMANCES PAR DYNAMIQUE MOLECULAIRE"

Sylvie NEYERTZ

Maître de Conférences - 33ème Section CNU

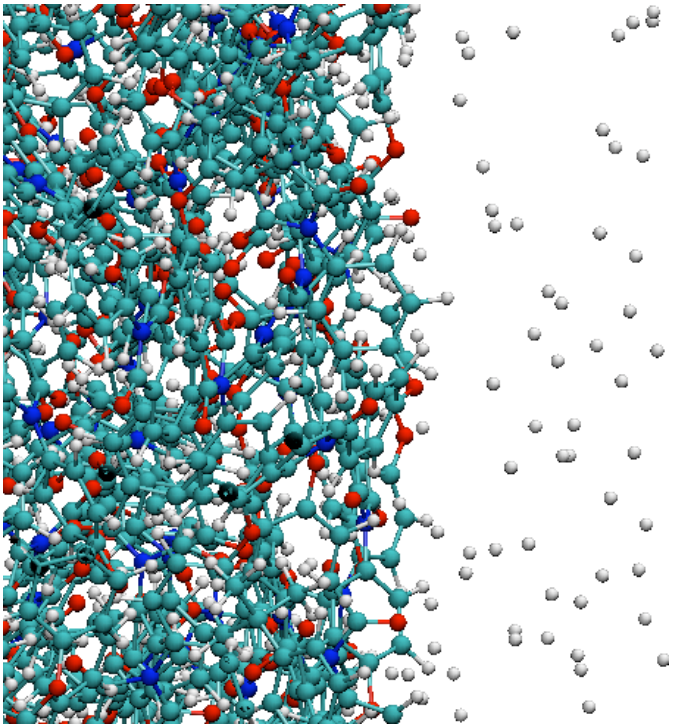

Université de Savoie, 2006

"A MOLECULAR DYNAMICS STUDY OF MICROSTRUCTURE AND TRANSPORT PHENOMENA IN HIGH-PERFORMANCE POLYMERS"

A SUMMARY OF RESEARCH ACTIVITIES

by

Sylvie NEYERTZ

To Hélène and Aurélie

TABLE OF CONTENTS

1. INTRODUCTION

This manuscript is an extended summary of my research activities over the years 1995-2006. Its general theme is the approach by classical molecular simulations of the microstructure and transport phenomena in high-performance polymer-based materials, which is mainly used here in order to complement experimental evidence. Most of the work has been carried out within the framework of molecular dynamics (MD) simulations,[1] which integrate Newton's equations of motion for all the atoms in a system and can thus provide direct structural and dynamical information at the atomistic level. However, a prerequisite of any realistic MD simulation is a good model, and sophisticated preparation procedures and interaction potentials will be needed to properly represent systems as complex, as versatile and as large as polymers.

The macromolecules under study as well as the general forms for the interaction potentials are presented in Section 2. The preparation of dense samples of long-chain polymers in the amorphous state is a major difficulty in the field of molecular simulation and we have developed a generation procedure based on a combination of Monte Carlo (MC)[2] and MD simulations, which allows for chain configurations characteristic of the equilibrium melt to be created at the required temperature. This technique will be described in detail in Section 3, along with its extension to an original procedure based on the experimental solvent-casting for preparing model films and the introduction of curved interfaces due to solid fillers. The crystalline state will also be briefly commented. Further sections concern applications of the MD simulation technique to the transport of small molecules within an amorphous polymer matrix. Section 4 is devoted to ionic transport in flexible polymer electrolytes, whereas Section 5 and 6 analyse respectively gas and water transport in rigid glassy polymer membranes. Section 7 describes the specific interactions between silica nanoparticles and flexible oligomers, as a first step towards reinforcement of membranes by solid fillers. Some current projects are summarized in Section 8.

2. MOLECULAR MODELS

2.1. Chemical structures

Despite different structural and dynamical features, most of the polymers presented here[3-25] are at the basis of advanced technological applications because of their ability to efficiently transport selected small species within the macromolecular matrix. From their chemical structures and glass-transition temperatures (Tg), it is possible to differentiate between relatively low-Tg "flexible" and high-Tg more "rigid" materials.

Flexible polymers have received considerable attention as solid electrolytes, ever since their potential for dissolving ionic species and forming highly conductive materials was first reported.[26] Our studies have mostly focused on poly(ethylene oxide):

PEO 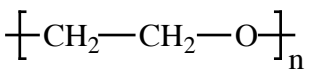

which is a well known ion-conducting polymer host used in a variety of applications such as thin-film batteries, electrochromic devices and sensors.[3-7,9,10,12,14,22] While optimizing the generation procedure for creating long-chain PEO models, we have tested a similar approach on isotactic poly(vinyl chloride):[11]

PVC 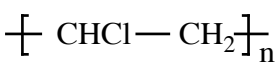

and, more recently, we have developed a model for poly(tetrafluoroethylene):[27]

PTFE

as a first step towards the proton and water-conducting Nafion® membrane used in hydrogen fuel cells.[28]

As far as rigid polymers are concerned, most of the attention has been devoted to the class of glassy polyimides,[15-18,20,21,24,25] which exhibit significant gas selectivities and can thus be used as dense membranes for gas separation.[29] We have examined several chemical structures based on either the pyromellitic (PMDA), the 4,4'-oxydiphthalic (ODPA) or the bicyclo(2.2.2)-oct-7-ene-2,3,5,6-tetracarboxylic (BCDA) dianhydrides. The diamines were

respectively the 4-4'-oxydi(phenylamine) (ODA), the 2-trifluoride-4-4'-oxydi(phenylamine) (CF_3ODA), the 2-methoxy-4-4'-oxydi(phenylamine) (MeOODA) and the 1,3-bis-4-aminophenoxy benzene diamine (PDB):

PMDA-ODA

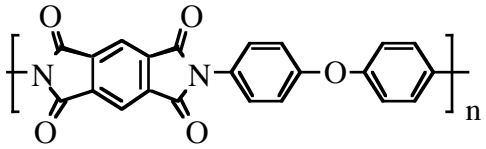

ODPA-ODA

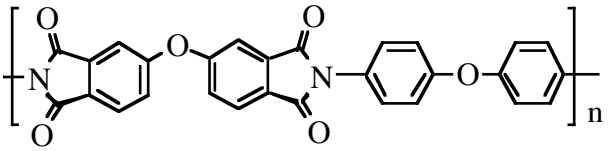

BCDA-ODA

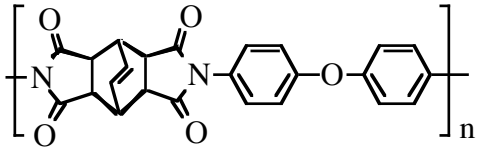

(ODPA/BCDA)-ODA

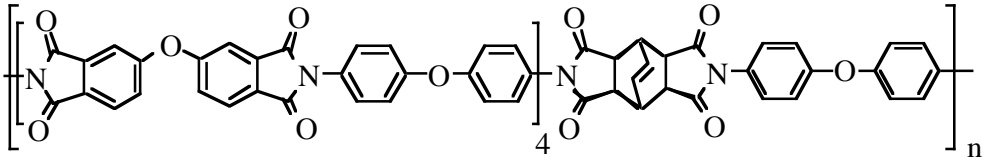

(ODPA/BCDA)-CF_3ODA

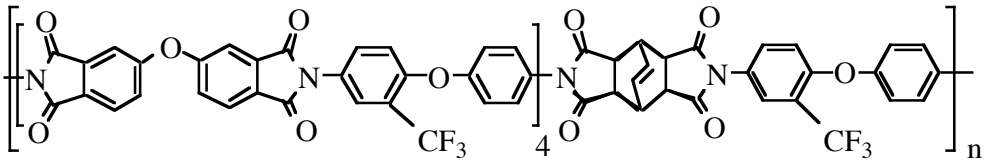

(ODPA/BCDA)-MeOODA

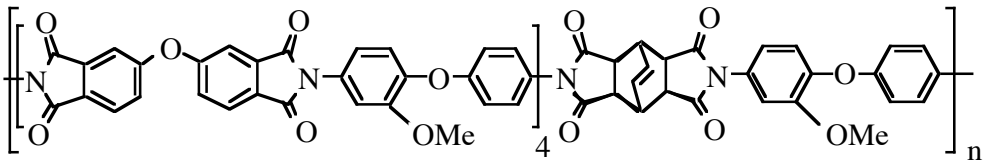

ODPA-PDB

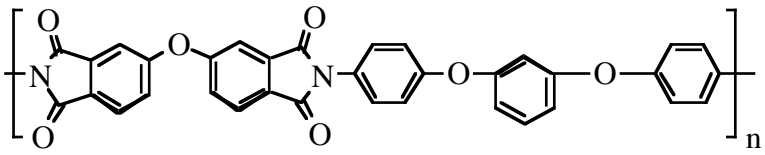

Other polycyclic polymers under study have included poly(ether ether ketone),[15] cellulose[13,23] and a poly(3-acetamido-undecanoic-succinimidyl-thiophene):[19]

PEEK

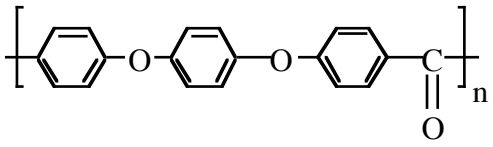

cellulose

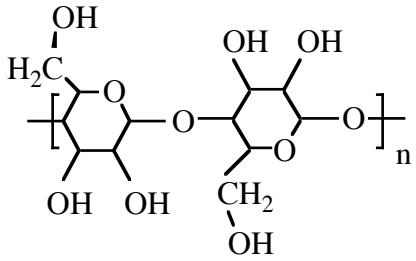

polythiophene

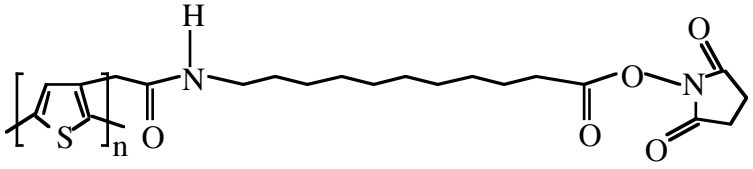

2.2. Potentials

The force-field describes the potential energy of a system as a superposition of simple analytical functions which are presented in this section. In polymer simulations, high-frequency modes, such as bond stretching or fast motions of the hydrogens in explicit CH_2 and CH_3 groups, can be removed using rigid constraints.[30] It both allows for the use of a reasonable time step in the MD integration algorithm, *i.e.* usually $\Delta t = 10^{-15}$ s, and avoids problems of equipartition. This approximation is justified by the fact that backbone bending and torsion modes are sufficiently decoupled from the higher frequency modes.[31]

A typical functional form of the total potential U_{pot} for macromolecules is:

$$U_{pot} = \sum_{\theta} U_{bend}(\theta) + \sum_{\tau} U_{tors}(\tau) + \sum_{i-sp^2} U_{oop}(i) + \sum_{(i,j)_{nb}} U_{vdw}(r) + \sum_{(i,j)_{nb}} U_{coul}(r) \qquad (1)$$

The first three terms refer to the "bonded" potentials of U_{pot} and arise from near-neighbour connections in the structure:

(A) describes the polymer angle-bending deformations by a harmonic function in the cosine of the bond angles, θ:

$$U_{bend}(\theta) = \frac{k_\theta}{2} (cos\theta - cos\theta_0)^2 \quad (2)$$

(B) represents the torsional motions around the dihedral angles τ by a sixth-order polynomial in $cos\,\tau$:

$$U_{tors}(\tau) = \sum_{n=0}^{6} a_n \cos^n \tau \quad (3)$$

(C) keeps sp^2 structures planar by using a harmonic function in the distance d from the i-sp^2 atom to the plane defined by its three attached atoms:

$$U_{oop}(i - sp^2) = \frac{k_{oop}}{2} d^2 \quad (4)$$

Atoms belonging to the same chain (but separated by more than two bonds[17] or by more than three bonds[3,4] depending on the lack or inclusion of 1···4 interactions in the torsional potential) and atoms belonging to different molecules also interact through the following so-called "non-bonded" potentials, which depend on the distance r between two interacting sites:

(D) describes the van der Waals interactions, either through the Lennard Jones (LJ) form,

$$U_{vdw}(r) = U_{LJ}(r) = 4\varepsilon \left(\left(\frac{\sigma}{r}\right)^{12} - \left(\frac{\sigma}{r}\right)^{6} \right) \quad (5a)$$

either through the Buckingham (Buck) form,

$$U_{vdw}(r) = U_{Buck}(r) = D_{Buck} \exp\left(\frac{-r}{\rho_{Buck}}\right) - \frac{E_{Buck}}{r^6} \quad (5b)$$

or through a shorter range form, the purely repulsive Weeks-Chandler-Andersen (WCA) potential:

$$U_{vdw}(r) = U_{WCA}(r) = 4\varepsilon \left(\left(\frac{\sigma}{r}\right)^{12} - \left(\frac{\sigma}{r}\right)^{6} \right) + \varepsilon \quad \text{when r} \le 2^{1/6}\sigma$$
$$U_{vdw}(r) = U_{WCA}(r) = 0 \quad \text{when r} > 2^{1/6}\sigma \quad (5c)$$

with ε being the well-depth of the potential, σ the distance at which the potential is zero and (D_{Buck}, ρ_{Buck}, E_{Buck}) the specific parameters for the Buckingham potential.[32]

(E) accounts for Coulombic interactions in the same conditions than (D) with q_i and q_j being charges on atoms *i* and *j* respectively, and ε_0 being the vacuum permittivity:

$$U_{coul}(r) = \frac{q_i \, q_j}{4 \, \pi \, \varepsilon_0 \, r} \qquad (6)$$

In bulk models, the electrostatic potential is calculated using the Ewald summation method.[33,34] However, in the larger membrane models which are only periodic in two dimensions, the Ewald sum is difficult to converge[2] and can become totally prohibitive in terms of computational time. It can be replaced by a particle-mesh technique using an iterative solution of the Poisson equation,[35] which separates the Coulombic interaction into two parts, a short-range term and a smoothly decaying long-range term. The short-range contribution is calculated directly as a sum of pair interactions in real space. Unlike the Ewald summation, the long-range part is also handled in real-space with a smooth projection of discrete point charges onto a grid[36] followed by a multigrid-approach.[37] The advantages of such a technique are:- (i) it becomes progressively more efficient than Ewald as system sizes increase, (ii) it can be parallelized within a domain decomposition approach, and (iii) it is equally applicable to periodic, partially periodic, or non-periodic systems.[35]

The force-field parameters used for the various polymers were either empirically optimized (PEO, cellulose, PTFE),[3,4,13,23,27] either taken from a specific force-field available in the literature (PVC)[11] or from a generic one such as the TRIPOS 5.2 force-field which has been tested on a large number of cyclic compounds (polyimides, PEEK, polythiophene).[11,15,17,18] The charges were obtained by performing *ab initio* calculations on representative three-monomers fragments of the structures under study using the *Gaussian* computer program[38] at the B3LYP/6-31G** level. Partial charges in the central moities of the model fragments, q_i/e, were then extracted by an ESP-fitting procedure.[39] The cross-terms for the van der Waals parameters (Eq. 5) were obtained from standard combination rules.[1]

The calculations were performed using successive versions of either the scalar *gmq* suite of programs[40] or of its parallel version based on the domain decomposition approach,[41] *ddgmq*. Computational time was obtained from the CINES (Montpellier, France) and IDRIS (Orsay, France) supercomputing centres as well as from local resources at the University of Savoie (Le Bourget-du-Lac, France), the University of Nancy I (Vandoeuvre, France), UMIST (Manchester, UK) and the University of Uppsala (Uppsala, Sweden). Most atomistic representations are displayed using the VMD 1.8.2 software.[42]

3. STARTING STRUCTURES FOR POLYMERS

3.1. Bulk models of amorphous polymers

Timescales currently spanned by MD methods are of the order of 10^{-9} to 10^{-8} s for large molecular systems, and are hardly compatible with the relaxation times of high molecular-weight polymers, which can reach the order of 1 s or more.[43] The starting structures for simulations of amorphous polymer chains must thus already be fairly relaxed. Various computational methods have attempted to solve this problem, *e.g.* modified rotational isomeric state (RIS),[44] reptation,[45] reverse,[46] end-bridging and other connectivity-altering[47-64] MC moves, soft-core potentials,[65] Gaussian lattice algorithms,[66] as well as multi-scale techniques involving coarse-graining and reverse-mapping back to the atomistic scale.[67,68]

We have continuously developed a highly-efficient fully-atomistic technique based on a hybrid Pivot Monte Carlo (PMC)-Molecular Dynamics (MD) single-chain sampling procedure, referred to as "hybrid PMC-MD", which allows for chain configurations characteristic of the equilibrium melt to be created at the required temperature.[4,10,11,15,17,21,24,69-71] Like many single-chain models,[44,72,73] it is based on the assumption by Flory[74] that long-range interactions in pure melts composed of homopolymers are completely screened and that their configurations can be described by considering isolated molecules with only a certain number of specific near-neighbour intramolecular interactions. In the PMC-MD approach, the configurational phase-space of the polymer is sampled using pivot Monte Carlo (PMC) moves[75] for rotatable torsions, while standard MD algorithms are used to explore the various oscillatory modes of the chains. In agreement with Flory's theory of a "local energy approximation", only highly localized interactions are taken into account.

The strength of this technique is that it is *systematically* validated for a given polymer by undertaking separate molecular dynamics simulations of bulk melts for short-homologue chains which can be fully relaxed using MD on its own. Their conformational and configurational statistics are then compared to those obtained using PMC-MD sampling.[9-11,15,69-71] Once validated, the hybrid PMC-MD single-chain sampling has proven very

successful to create appropriate starting configurations for long-chain polymers.[6,7,9,12,17,21,24] In the mid-nineties, separate codes specific to the polymer under study had to be developed.[4,10,11,69-71] However, the PMC-MD algorithm has now been implemented into the generalized code *gmqpmc*,[40] which allows for arbitrary connectivity.

3.1.1. The hybrid PMC-MD method for single-chain sampling

The starting point is to create an arbitrary configuration for a polymer chain by using equilibrium bond lengths and angles. All torsions τ, which are significant with respect to the global configurations of the chains, are then identified. Essentially, this includes all backbone torsions, with the exception of those within rings which cannot be changed independently whilst keeping all bond lengths constant. This has presented no problem for the rings in the polycyclic chains under study up to now, since none of them could interconvert between different isomeric forms. Nevertheless, it is clear that for certain non-planar rings such as cyclohexane-types (which have the possibility to interchange between boat and chair conformations), it would require the incorporation of correlated torsion pivots into the algorithm. To avoid the low acceptance rates of pivot moves implied by sampling evenly in τ, "smart tables" of cumulative relative Boltzmann factors[76,77] are built for each different type of pivotable torsion. With k_B being Boltzmann constant, these smart-table functions $S(\tau)$ are defined from the appropriate torsional potential at a temperature T as:

$$S(\tau) = \frac{\int_{-\pi}^{\tau} \exp(-U_{tors}(\tau')/k_B T)\, d\tau'}{\int_{-\pi}^{\pi} \exp(-U_{tors}(\tau')/k_B T)\, d\tau'} \qquad (7)$$

and are used subsequently throughout the whole sampling procedure for choosing new angles. As shown in Fig. 1, a new dihedral angle τ_{new} can be obtained from a random number R_n sampled evenly from the range $0 \le R_n < 1$. Although in principle all values of τ can be selected, the smart table ensures that τ_{new} is most often chosen in a region of high probability. Please note that in the convention used in *gmq*, the dihedral angle τ varies from -180° to +180°, with 0° corresponding to the *trans (T)* conformation, *i.e.* all four atoms lie in the same plane and atoms at either end are at their furthest distance apart. However, we usually use a broader definition for the state of the dihedrals with $-60° < \tau < 60°$ being considered as

"*trans*". Similarly, the *gauche*$^-$ (G^-) and *gauche*$^+$ (G^+) conformations are those angles situated either in the $-180° \leq \tau \leq -60°$ or in the $60° \leq \tau \leq 180°$ intervals, respectively.

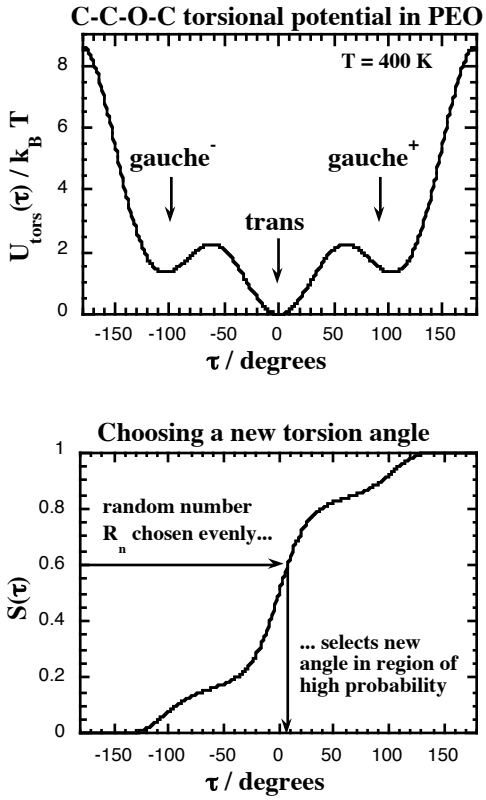

Fig. 1 *An example of smart table for a pivotable torsion. The backbone C-C-O-C potential is from our optimized force-field for poly(ethylene oxide).*[3,4]

Once built, the single chain is then subjected to a series of attempted PMC moves at regular intervals of *e.g.* ~100 MD dynamics steps. MD alone is very good at sampling the various oscillatory modes of a molecule but, in single-chain sampling, it is quite inefficient at exploring the torsional phase-space and at crossing the barriers to internal rotation. PMC, on the other hand, is specifically designed to overcome those torsional barriers and, in single-chain sampling, is highly efficient. Both are carried out within the framework of Flory's "local energy approximation", *i.e.* all intermolecular interactions are switched off and the range of interactions along the chain is set by a "local energy parameter" referred to as n_{bonds}. It represents the maximum number of bonds allowed between two non-pendant atoms which can interact through the non-bonded potentials (Eqs. 5&6). To define the interacting neighbours, a search of the connectivity first takes place for each backbone atom and

effectively leads to full interactions between groups separated by n_{bonds} backbone bonds (Fig. 2):

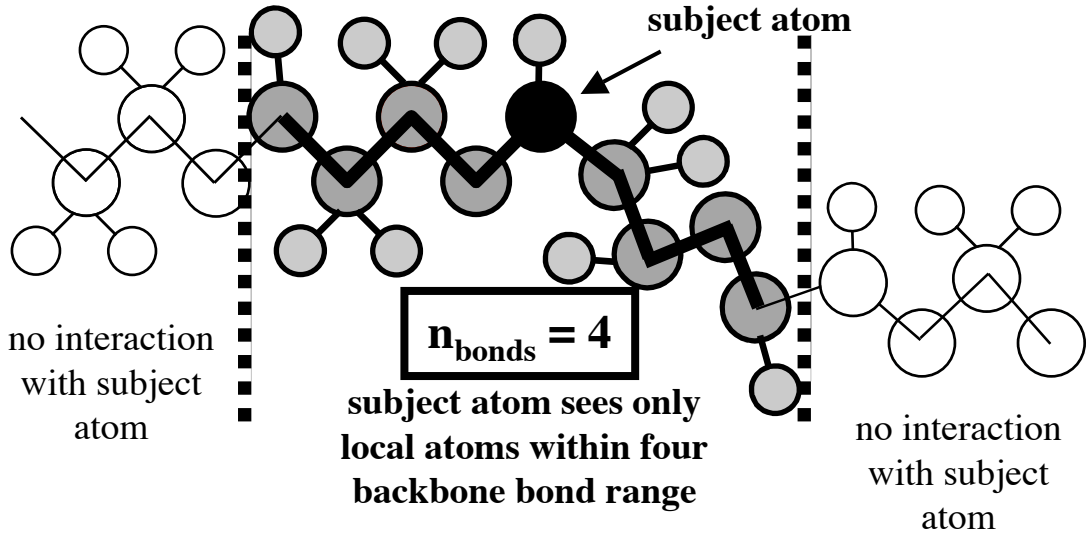

Fig. 2 *A schematic representation of the local energy approximation using $n_{bonds} = 4$*

A punctual drawback associated with the use of the PMC-MD single-chain sampling is the exact definition of the local energy parameter. While it can be simply approximated by the local energy originating directly from the interaction potential of the input model, our experience is that n_{bonds} is not universal and has to be optimized depending on the chemical structure of the molecule under study (Table I):

Table I*The optimal local energy interaction parameter as a function of the polymer*

Macromolecules	**Optimal n_{bonds}**	**References**
n-alkanes and PE	4	[69-71]
PEO	4	[4,10]
PVC	5	[11]
SBR	6	unpublished
BCDA-ODA	4	[15]
ODPA-PDB	4	[15]
PEEK	4	[15]
PBMA	4	[78]
cellulose	7	[79]
PTFE	5	in preparation
perfluoroethers	6	to be confirmed

Although it is clear that the value of $n_{bonds} = 4$ is often encountered, there are enough "exceptions" to recommend that, prior to using PMC-MD sampling for creating long-chain configurations, this parameter should be thoroughly checked. There might be some indications from the chemical structure: for example, it should be significant that PVC and PTFE which both carry strongly-negative halogen atoms, have the same n_{bonds} parameter. The same goes for the polyimides and PEEK, where the interactions between the hydrogens situated immediately on either side of an ether or a ketone bridge are obviously very important; these pendant hydrogens are bonded to carbons in the two linked rings which are themselves separated by four bonds, hence $n_{bonds} = 4$. More complicated chemical structures such as cellulose or perfluoroethers will tend to have larger n_{bonds}. However, there are, up to now, too few examples to draw definite conclusions. Systematically increasing n_{bonds} is not a solution either as it ultimately leads to sampling the ideal gas phase where the chains undergo a collapse transition.[4] As will be shown later, this n_{bonds} parameter can be unambiguously determined by comparing single-chain-sampled configurations with those in the bulk melt for chains which can be decorrelated using MD on its own. Once this has been done, the optimized value can then be used with confidence in the rest of the procedure for arbitrary chain lengths.

Each time a PMC move is attempted, a torsion angle is chosen randomly from the list of pivotable ones created at the start and its new value is obtained from the smart table (Fig. 1). The energy difference between the pivoted $U_{pivoted}$ and unpivoted chain $U_{unpivoted}$, $\Delta U = U_{pivoted} - U_{unpivoted}$, is then calculated. The only contributions that need to be taken into account are the non-bonded terms within the definition of the local energy (*i.e.* in the absence of any cutoffs others than n_{bonds}) and those resulting from torsions which share the same central bond as that being pivoted. Coulombic interactions can be calculated directly using the 1/r form. If ΔU is less than $5k_BT$ (the limit leading to the breakdown in the dynamic algorithm), then this PMC move is submitted to a standard Metropolis acceptance criteria:[80] another random number R'_n is chosen such that $0 \leq R'_n < 1$, and the new configuration of the chain is accepted if $exp(-\Delta U/k_BT) > R'_n$. In the case where an attempted pivot is accepted, new randomized

velocities are selected from a Boltzmann distribution corresponding to the required temperature. The MD then continues for this chain until the next attempted pivot. In the case where the change in energy is not accepted, the MD simply continues unperturbed. Although decorrelation from the initial structure usually occurs within a few thousand pivot moves, PMC-MD single-chain sampling can be carried out for millions of steps in order to acquire good statistics.

The procedure described above has actually slightly evolved over the years, originating from a PMC-only single-chain sampling for both bend and dihedral angles[4,10,11,69-71] and including the MD at a later stage.[15] MD proving as good as PMC to sample the harmonic bending angle phase-space (Eq. 2), the code has been simplified by removing the pivot moves for the bends. Note that the acceptance criterion was not affected since only PMC moves are subject to it. However, one concern was that the MC pivot moves are based on a sampling of the canonical NVT ensemble, while standard MD would correspond to an NVE ensemble, except that velocity resampling takes place at relatively frequent intervals. One could expect a reasonable equivalence between the two methods, but this needed to be checked. Another concern was related to the rigid constraints that were applied in the MD. In the PMC algorithm, there is an implicit assumption that coordinates and momenta are strictly independent variables and that the atoms are held together by flexible, even if very stiff, bonds. For a model in which rigid bond constraints are used, this assumption of independence is no longer valid. In the hybrid PMC-MD method, there is obviously an incompatibility between the way the pivots are done (bonds assumed flexible) and the fact that bonds are treated as rigid in the MD.

In order to assess whether these points had a significant influence, several calculations on n-alkanes,[69,70] PEO[4,10] and PVC[11] short-chain homologues, which all originated from a PMC-only approach, were redone using the hybrid PMC-MD code.[15] The average percentage of angles in the *trans* state, $<\%trans>$, the mean square radii of gyration $<S^2>$ and the mean square end-to-end distances $<R^2>$ for the chains were analysed. Comparative results are presented in Table II for a rigid-bond united-atom model of a linear 20-site-alkane system[69,70]

at both 500 K and 1500 K using n_{bonds} =4.[15] In addition, an extra PMC-MD simulation was performed at the highest temperature with the same model, except that the rigid bonds were replaced by harmonic springs with a force constant of 440 kg s^{-2}.

Table II *Results obtained for single-chain sampling of a linear 20-alkane model using either a pure PMC algorithm or the hybrid PMC-MD technique at both 500 K and 1500 K. At 1500 K, an extra PMC-MD run was made with flexible bonds.*[15]

	500 K		**1500 K**		
	PMC-only	**PMC-MD**	**PMC-only**	**PMC-MD**	**PMC-MD flexible bonds**
<*%trans*>	72.1±0.1	72.2±0.2	56.7±0.1	57.2±0.1	56.7±0.1
$<S^2>$ / $Å^2$	36.2±0.1	36.2±0.1	29.9±0.1	30.1±0.1	30.2±0.1
$<R^2>$ / $Å^2$	313±1	313±2	236±1	238±1	238±1

Table II shows that the agreement is very satisfactory. In addition, probability density distributions of the torsion angles, S^2 and R^2 were found to be superimposable for both methods, thus proving that the PMC-only approach can be safely replaced by the hybrid PMC-MD. Because of the subtleties regarding the treatment of the bonds, a slight difference is evident for <*%trans*> between the rigid and the flexible bonds models at high temperatures, but it is clear that it remains very limited.

3.1.2. Preparing bulk models

A series of uncorrelated chains are generated by PMC-MD single-chain sampling at a temperature T corresponding to the melt of the polymer while using an appropriate local energy parameter (Table I). For long-chain polymers, T is usually chosen as being slightly above their glass-transition temperature. The chains are randomly orientated and distributed in a periodic cubic MD box in order to give an initial density typically equal to either ~1 g cm^{-3} or to the experimental density if available.[17] However, single-chain sampling completely ignores intermolecular and all "non-local" intramolecular interactions. As a consequence, the

initial structures usually have huge overlap energies, which must first be relaxed while maintaining as well as possible the carefully-prepared configurations.

The most reliable way to remove these overlaps has been found to be *via* the progressive introduction of the excluded-volume during short MD simulations under constant-volume and temperature conditions (*NVT*).[4,10,11,15] The bending, torsions, out-of-planes and constraints are switched on, while the van der Waals potential is introduced very gradually, *i*.e. it is scaled up by a factor varying linearly from 0 to 1 over a limited period. At this stage, a short potential truncation radius can be used and velocities are rescaled at each time step to compensate for the large amount of heat produced in the system. For cyclic molecules, additional problems were found to occur in that a bond spanning the plane of a ring could become trapped in an unphysical configuration with the two atoms of the bond on either side of the ring or, alternatively, different rings could be interlocked. This is a well-known artefact reported in *e.g.* other simulations of polyimides,[81] and was solved here by introducing "phantom atoms" at the centre-of-coordinates of each six-membered or five-membered ring upon completion of the generation procedure. The presence of this extra interaction centre occupying the space in the middle of the rings is sufficient to prevent the unphysical spearing and interlocking.[15] It should also be noted that it is in principle possible to replace the progressive introduction of the excluded-volume potential by its purely repulsive WCA form (Eq. 5c), as has been recently done for PTFE.[27] However, the WCA potential can also affect the configurations if it is applied for too long and this has to be checked on a case-by-case basis. In a similar vein, the WCA potential can be used in place of the other more realistic non-bonded forms in order to speed-up the calculations. For example, PMC-MD sampling has been carried out for the 40-*mers* ODPA-ODA polyimide using different combinations of the non-bonded potentials. The mean-square radii of gyration, $<S^2>$, were found to be respectively 58.4 Å using U_{LJ} and U_{coul} (Eqs. 5a&6), 62.5 Å using only U_{LJ} (Eq. 5a) and 62.0 Å using U_{WCA} (Eq. 5c) on its own, while the corresponding distributions overlapped well. ODPA-ODA configurations are thus mostly governed by the excluded-

volume repulsive interactions, which means that WCA is a good approximation for these single-chain-sampled polymers.[21]

Following the introduction of the excluded-volume potential, phantom atoms (if applicable) are removed and electrostatic interactions are switched on. The non-bonded cutoff is set to its final value and the Ewald parameters are optimized.[8,82] Long-range corrections to the energy and the pressure are added using the approximation that the radial distribution functions are equal to unity beyond the cutoff.[1] The simulation continues at constant-volume in order to relax hot-spots and to allow the bulk melt to come to thermal equilibrium. The temperature is maintained by loose-coupling to a heat bath[83] with a constant usually equal to 0.1 ps.

The consequences for the chain conformations of such an introduction of the full potential were originally reported for relatively flexible united-atom *n*-alkanes.[70] It was found that $<S^2>$ for n=50 chains was reduced by about 5% during this step and that it could not be improved by a number of slight variations, such as initially energy-minimizing the system. Perturbations subsequently diminished with time but it seemed hard to avoid this being governed by the natural relaxation times of the polymer. This problem has recently been thoroughly studied by Auhl et al.[84] in model bead-spring chains. A fast introduction of the full interaction potential for initially non-interacting chains leads to increases of the average intramolecular distances in the 2-100 monomers ("intermediate") length scale.[84] The range affected was independent of chain length although the degree of perturbation increased with chain length. Significant amelioration could be obtained by first smoothing the density distribution by rigid body motions of the initially randomly inserted chains and by adjusting the speed at which the excluded volume is introduced. It seems reasonable to assume that stiffer more realistic chains are less prone to deformation in the first place on such intermediate length scales. However, this remains to be seen, as does the actual sensitivity of the physical properties to such variations in the preparation procedure.

Simulations can then be switched to either *NpT* conditions, in which the isotropic pressure is maintained by loose-coupling and the simulation box is kept cubic, or to ***NPT***

conditions, in which the on-diagonal and off-diagonal components of the pressure tensor are also maintained by loose-coupling but the simulation box is allowed to relax towards its equilibrium shape and density. The loose-coupling constant for the pressure is typically equal to 5 ps.[85] Equilibration runs are carried out until the densities are stabilized, after which the production run continues up to several nanoseconds (Fig. 3).

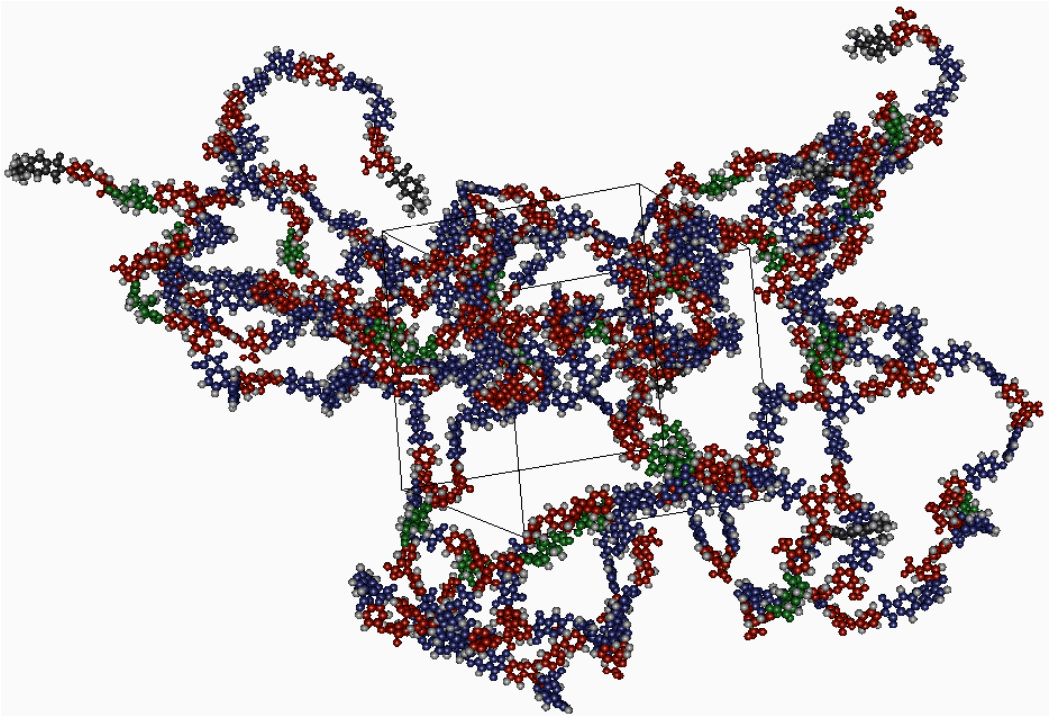

Fig. 3 *A schematic representation of a 6522-atom (ODPA/BCDA)-CF_3ODA polyimide simulation box.*[17]

If the system is required at a lower (resp. higher) temperature, it is progressively cooled down (resp. warmed up) at a typical rate of -1 (resp. 1) K ps^{-1}. Configurations and thermodynamic data are stored at preset intervals for post-analysis.

3.1.3. The short-homologue tests: validation of the preparation procedure

As noted before, the PMC-MD single-chain sampling procedure has been tested for all polymers given in Table I on short-homologue chain lengths for which full relaxation can be achieved in a reasonable MD simulation time alone. If the comparison proves favourable, single-chain sampling can be used to generate longer chains for which direct relaxation by MD is currently out-of-reach. MD equilibrium calculations have thus been carried out for

series of short-homologue melts at adequate temperatures, with the simulation boxes being initially prepared as described in Section 3.1.2.[4,10,11,15,69-71,78,79]

To assess the degree of conformational equilibrium in the bulk melt systems, correlation functions of the form:

$$R_{TT}(t) = \left\langle H_T\{\tau_i(0)\} H_T\{\tau_i(t)\} \right\rangle \tag{8}$$

where $\tau_i(t)$ is the value of the dihedral angle i at time t and $H_T\{\tau_i(t)\}$ the associated characteristic function of the *trans* state ($H_T\{\tau_i(t)\} = 1$ if $-60^\circ < \tau_i(t) < 60^\circ$ and zero otherwise), are calculated for the different types of significant dihedral angles. $R_{TT}(t)$ can be normalized according to:

$$C_{TT}(t) = \frac{R_{TT}(t) - \langle X_T \rangle^2}{\langle X_T \rangle - \langle X_T \rangle^2} \tag{9}$$

with $\langle X_T \rangle = R_{TT}(0)$ being the mean fraction of the angle in the *trans* conformation. This method is known to provide a reliable evaluation of the extent of conformational relaxation.[86,87] Configurational relaxation is evaluated by calculating the normalized autocorrelation function $C_R(t)$ for the square end-to-end distance of the individual chains as a function of time t, $R_i^2(t)$:

$$C_R(t) = \frac{\left\langle R_i^2(0) R_i^2(t) \right\rangle - \left\langle R_i^2 \right\rangle^2}{\left\langle R_i^4 \right\rangle - \left\langle R_i^2 \right\rangle^2} \tag{10}$$

or from the corresponding $C_{RV}(t)$ related to the end-to-end vector as a function of time, $\mathbf{R}_i(t)$, which characterizes the orientation:

$$C_{RV}(t) = \frac{\left\langle \mathbf{R}_i(0) \mathbf{R}_i(t) \right\rangle - \langle \mathbf{R}_i \rangle^2}{\left\langle \mathbf{R}_i^2 \right\rangle - \langle \mathbf{R}_i \rangle^2} \tag{11}$$

The $C_{TT}(t)$, $C_R(t)$ and $C_{RV}(t)$ functions, averaged over all molecules (or dihedrals) and over all time origins, usually provide different relaxation times since the conformational degrees of freedom decorrelate much faster than the configurational properties (Fig. 4). They are also highly dependent on the chemical structure, on the chain length and on the temperature under study:

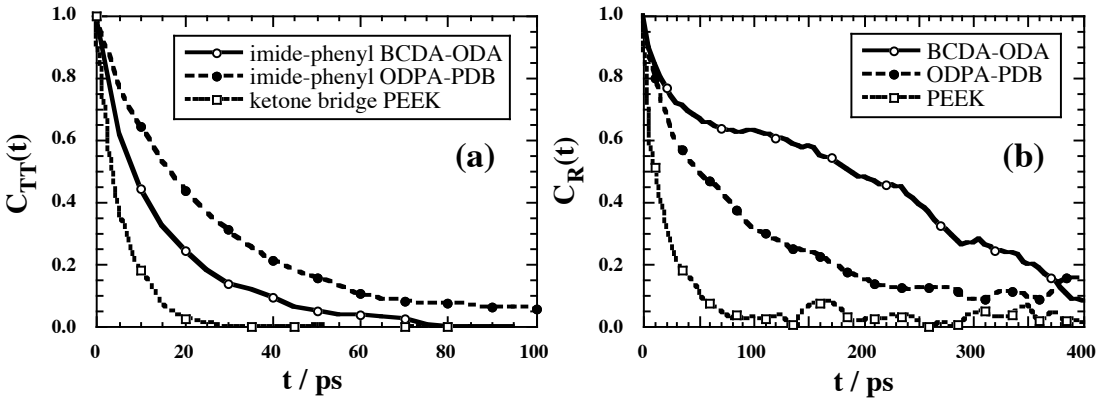

Fig. 4 *Normalized relaxation functions for (a) the trans state of torsion angles around polycyclic pivot bonds and (b) the square end-to-end distances at 1000 K in MD simulations of short oligomers.*[15]

The longest relaxation time will be used to identify the start of the MD production run for the bulk melt systems. It ensures that the timescale used is long enough to provide a proper sampling of the configurational phase-space. In the meantime, PMC-MD calculations are carried out over several nanoseconds at the same temperature with a preset value of n_{bonds}, the same potential and for the same chain length than those of the corresponding bulk melts. Table III shows the very good agreement in the results obtained from both methods for different chain lengths of PVC-homologues, using $n_{bonds} = 5$ in the PMC-MD sampling.

Table III *<%trans> for backbone torsions around C-C bonds, $<S^2>$, and $<R^2>$, for single-chain sampled ($n_{bonds} = 5$) and the corresponding bulk-melt MD simulations at 600 K. The molecules are small PVC-homologues with n_b being the number of backbone sites per chain. There are respectively 90, 60, 25, 15 and 11 molecules in the bulk melt systems.*[11]

	Single-chain sampling			**MD multi-chain bulk melt**		
n_b	<%trans>	$<S^2>$ / Å^2	$<R^2>$ / Å^2	<%trans>	$<S^2>$ / Å^2	$<R^2>$ / Å^2
7	48.64±0.03	6.180±0.001	37.78±0.02	48.4±0.2	6.16±0.02	39.1±0.2
15	50.97±0.02	19.28+0.01	153.8±0.3	50.6±0.2	19.5±0.1	158±3
23	51.48±0.02	36.92±0.05	296.6±0.9	51.1±0.2	37.1±0.6	303±10
31	51.71±0.02	57.2±0.1	447±2	51.5±0.2	57±1	449±20

Other values than 5 for n_{bonds} give poorer results, as displayed in Fig. 5 by the variation at 600 K of the PVC characteristic ratio C_n:

$$C_n = \frac{\left\langle R^2 \right\rangle}{\left(n_b - 1\right)\left\langle l^2 \right\rangle} \tag{12}$$

with $(n_b - 1)$ being the number of C-C backbone bonds and $\langle l^2 \rangle$ their mean square bond length.[74] PMC-sampling with $n_{bonds} = 4$ clearly underestimates the bulk results.

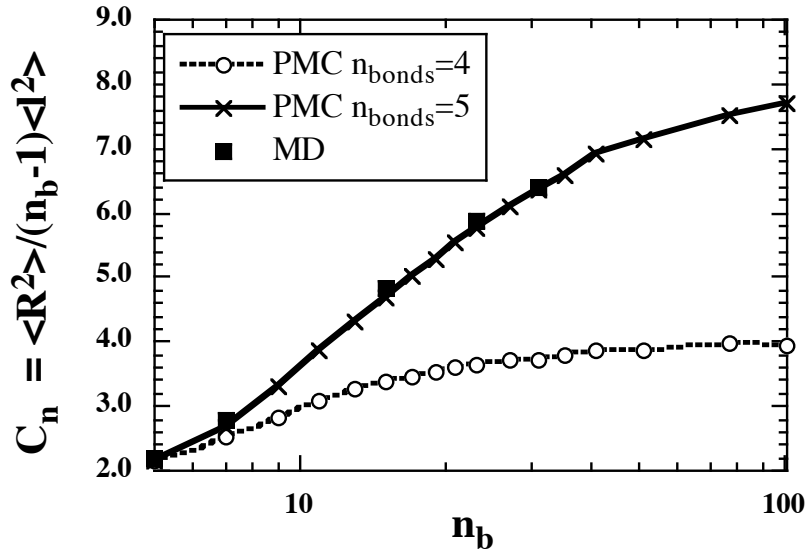

Fig. 5 *C_n as a function of n_b for single-chain-sampled PVC configurations with $n_{bonds} = 4$ (circles) and $n_{bonds} = 5$ (crosses), compared with those relaxed by MD (squares).*[11]

The probability density distributions for the distances between backbone atoms separated by exactly four and five bonds, the so-called "1···5" and "1···6" distances were analysed in order to explain Fig. 5. They revealed that coiled local structures corresponding to a succession of *gauche* conformations form when $n_{bonds} = 4$ and result in an overlap between "1···6" groups. This artefact is readily removed by allowing the "1···6" groups to interact, and leads to a much better agreement between configurations sampled with $n_{bonds} = 5$ and those relaxed by MD.[11] However, in the case of polycyclic molecules, $n_{bonds} = 4$ is good enough to provide an adequate representation of relaxed chain configurations by PMC-MD sampling (Fig. 6):[15]

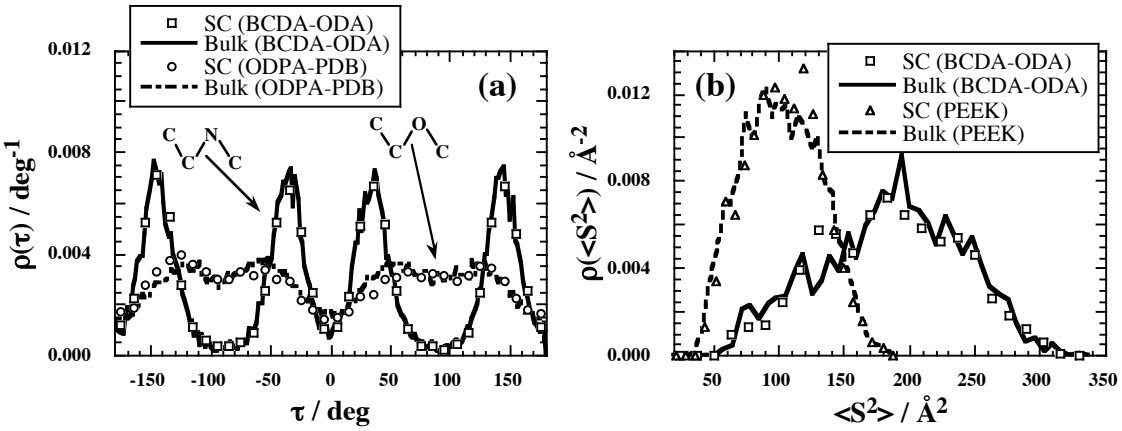

Fig. 6 *Single-chain-sampled (SC) vs bulk melt probability densities for (a) torsions and (b) mean square radii of gyration of polycyclic molecules at 1000 K using* $n_{bonds} = 4$.[15]

Although a general level of agreement of over ~95% between single-chain-sampled and bulk-melt-relaxed chains has been found,[11,15,69-71] we have encountered one exception up to now, *i.e.* the short homologues of polar poly(ethylene oxide), PEO. In that case, the agreement was at a level of ~70%-80% with $n_{bonds} = 4$, and the structural properties all indicated a tendency for the chains to relax towards more open configurations over the MD runs. The MD-relaxed limiting characteristic ratio in the melt was found to be ~5.5, *i.e.* very close to experimental evidence[4,88] and to connectivity-altering MC simulations of end-capped PEO.[62] Using larger values of n_{bonds} in the PMC-MD procedure did not help, but the discrepancy disappeared when all PEO partial charges were set to zero.[9,10] It was eventually traced to the competition in the bulk melt between attractive intramolecular "1···5" C-H···O and intermolecular C-H···O interactions. The latter are obviously missing from the single-chain sampling procedure and the *gauche* effect, *i.e.* the fact that torsions around C-C bonds tend to favour a *gauche* state in polyethers,[89] is subsequently slightly overestimated.[11] While this pointed out one of the limitations of Flory's approximation, the PEO chain structures grown using this technique are very flexible and can at least be conformationally and locally relaxed on a reasonable timescale. In addition, they lead to model densities very close to experiment[4,6,9,10] and those obtained using other generation procedures.[62,89] It should also be noted that several features considered in extended studies of connectivity-changing moves[47-49,53,55] have not yet been tested in our PMC-MD procedure. While the local energy parameter

appears to be independent of chain length (except for very short chains), it is clear that including polydispersity should be handled properly.[47,48] In the same vein, the possibility of adding a small tensorial field in order to orient the chains and study for example the viscoelastic properties[50,51] has not yet been assessed.

However, despite the reservation with respect to PEO, the excellent agreement obtained for all the other polymers of Table I proves that the PMC-MD generation technique, once tested on short-chain oligomers, can be used to reliably sample the configurational phase-space of molecules of arbitrary length in the bulk melt phase. Indeed, it has proven an excellent starting point for configurations of long-chain polymers.[6,7,9,12,17,21,24] For glassy systems such as polyimides, it is a lot easier than the succession of temperature annealing-cooling and compression-decompression stages used by Hofmann and coworkers.[81,90-95] Its reproducibility has also been checked, *e.g.* for a series of eight independently-prepared 40-*mers* ODPA-ODA polyimide models. Table IV shows that the preparation procedure is fully reproducible:[17]

Table IV *The average densities* $<\rho>_{model}$ *and nearest-neighbour intermolecular distances,* $r_{0.5}$*, defined from the indiscriminate intermolecular radial distribution function* g_{inter} *as* $g_{inter}(r_{0.5}) = 0.5$*, at 300 K for eight independently prepared ODPA-ODA packing models. The experimental density is 1.368 g* cm^{-3}.

System	$<\rho>_{model}$ / *g* cm^{-3} *(±0.001)*	$r_{0.5}$ / *Å* *(±0.05)*
(ODPA-ODA)-1	1.348	3.20
(ODPA-ODA)-2	1.395	3.10
(ODPA-ODA)-3	1.368	3.10
(ODPA-ODA)-4	1.345	3.25
(ODPA-ODA)-5	1.360	3.25
(ODPA-ODA)-6	1.368	3.20
(ODPA-ODA)-7	1.343	3.30
(ODPA-ODA)-8	1.355	3.15

3.2. Planar interfaces for amorphous polymers

Flory's local energy approximation[74] holds well for homogeneous systems and bulk periodic models can thus be considered as being representative of the amorphous core of a polymer membrane. However, the chemical structure is only one of the factors underlying the transport properties,[96] and it is well-known that a considerable number of other parameters will influence diffusion, selectivity or other physical properties over the entire processing stage. Among those, the so-called "skin-effects" are related to the differences between the surface layers and the core of a membrane.[96-100] It will thus be necessary to create atomistic models containing actual surfaces, *i.e.* where the chains cannot *a priori* be considered as equivalent and the periodicity is only effective in two dimensions.

Relatively few fully-atomistic techniques to prepare long-chain polymer films have been described in the literature. One approach is that of extending the *z*-axis in order to eliminate interactions of the parent chains with their images in one direction.[101-105] However, it is very unlikely that rigid chains, such as polyimides, would relax much at ambient temperatures in the timescale of a few nanoseconds. This also applies to the so-called healing method where a snapshot from an equilibrated bulk film is duplicated in the *z* direction and the two films are merged, thus increasing the thickness of the film.[104] The use of a repulsive wall in order to compress a bulk polyisoprene chain might appear more promising,[106,107] although it is likely to requires significant relaxation as well.

We have designed an original procedure loosely based on the experimental solvent-casting process for creating a fully-atomistic polyimide membrane model.[24] In reality, 40-*mers* ODPA-ODA polyimide films are processed[108-112] by preparing a 10% (w/w) solution of the polymer in *m*-cresol and casting it onto a clean glass plate. Solvent is subsequently removed through an appropriate heat treatment and the film is peeled off the glass plate by immersion in water. Since $<S^2>^{1/2}$ is usually quoted as being the minimum distance for the influence of the interface,[113-120] we based the size of our membrane model on a length of $\sim 2<S^2>^{1/2}$, *i.e.* a total of 141100 atoms in 68 ODPA-ODA chains. If the experimental

dimensions are respected, the model needs to be over 20-50 times larger than the typical sizes for glassy systems,[17,95] *i.e.* an enormous size for such simulations.

The solvation procedure was mimicked by choosing an initial volume for the 68-chain simulation box corresponding to the density of a 10% (w/w) solution. Since solvent evaporation occurs mostly through the uppermost surface of a film, the basis vectors in the *x* and *y* direction were left at the value expected from the experimental ODPA-ODA density whilst the basis vector in the *z* direction was increased to lead to a (virtual) solution density of an ideal (90% *m*-cresol / 10% ODPA-ODA) mixture. The 68 chains were then generated independently using hybrid PMC-MD single-chain sampling, randomly reoriented and distributed in the 10% solution simulation box. The excluded volume was progressively introduced and the "solvated system" was cooled down to the ambient temperature. A ten-layer diamond-lattice impenetrable wall was subsequently added on one side of the system. The wall-atom parameters were chosen so that the tetrahedral network was maintained and no interactions between polymer chains on either side of the box at all subsequent stages were possible, due to a judicious choice of the cutoff despite the continued imposition of periodic boundary conditions (Fig. 7).

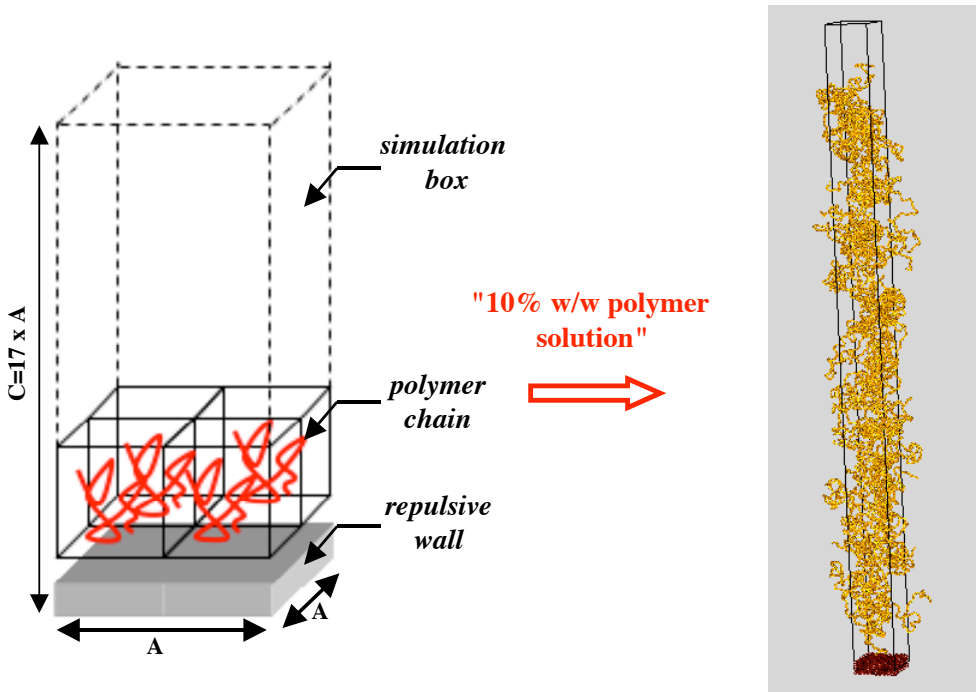

Fig. 7 *The creation of a virtual 10% (w/w) solution box for the ODPA-ODA polyimide.*[24]

It could be argued that inserting and then removing slowly explicit solvent molecules would have been preferable but this would have further increased the number of atoms and it is simply out-of-reach in terms of current computational resources.

The process of densification resulting from solvent evaporation was modeled by compressing the wall+polymer system. Since the surface area of a film remains quasi-constant throughout the experimental process, only the length of the cell in the z direction was progressively shrunk, whilst rescaling the z-positions of all atoms at each time step in an affine manner. The target box length was chosen in order to take into account the dimensions expected from the experimental ODPA-ODA density.

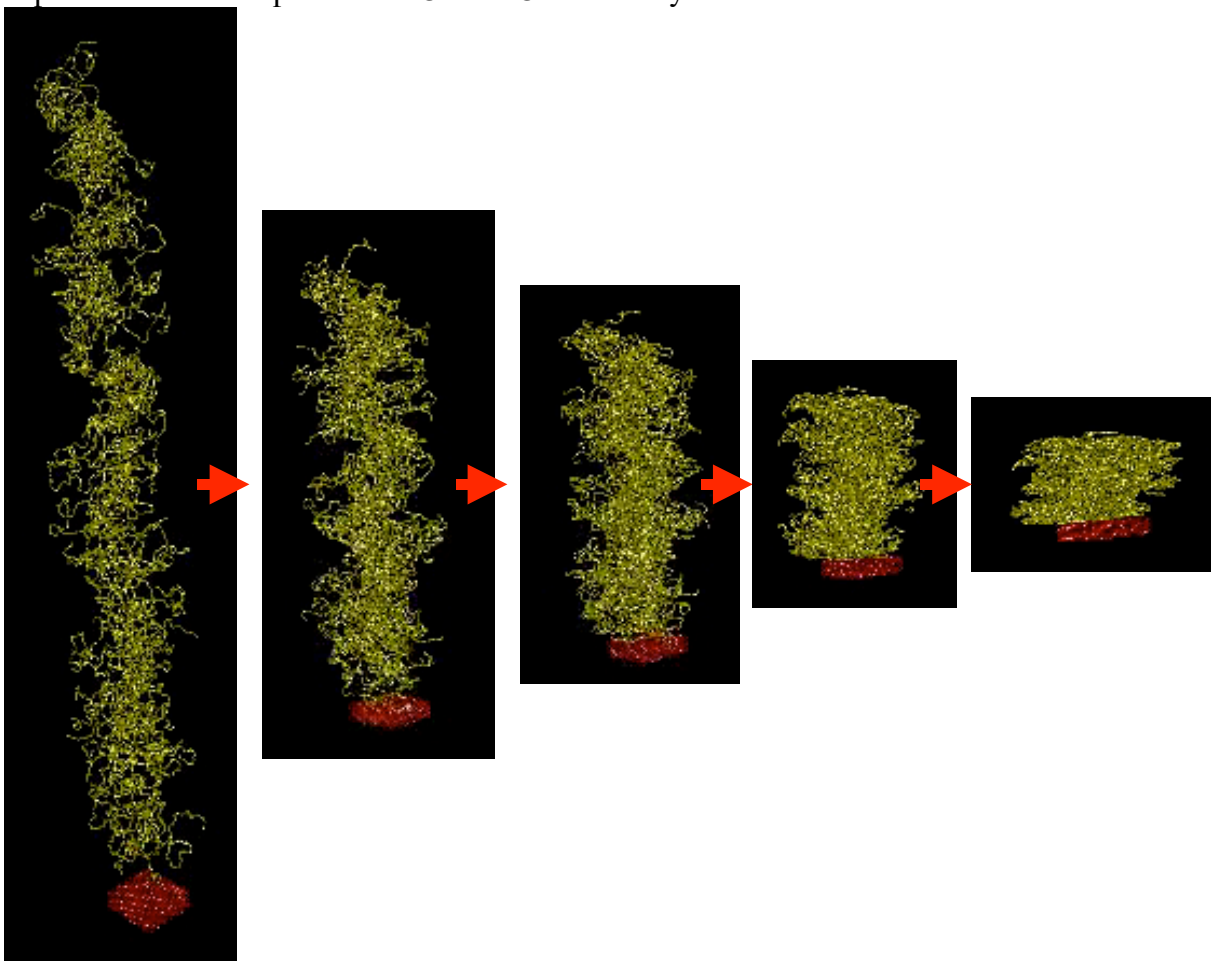

Fig. 8 *The compression phase designed to mimick the solvent evaporation process.*[24]

Here again, one word of caution is in order since the influence of an ever-changing concentration on the conformational properties of the chains remains rather unknown and is difficult to incorporate *a priori* in any simulation given the very slow relaxation times.

Experimentally, once most of the solvent has been evaporated at ambient conditions, the membranes are heat-treated to remove residual solvent and to relax internal stresses. High-temperature NVT runs were thus carried out at 700 K and the membrane was subsequently cooled down to 300 K. The dimensions of the box were slightly re-adjusted to have the bulk density in the middle part of the polymer.[24] This model was then used as the basis for two different studies. In the first one,[24] the polymer film with a width of ~130 Å was left effectively confined by the impenetrable wall. This "confined membrane" leads to high-density regions at the interfaces and is consistent with the fact that the real polyimides were cast on a glass plate (Fig. 9).[110] In order to insert gas probes between the wall and the polymer, the four middle layers of the wall were set to be impenetrable to both polymer and gas, while the three wall layers closest to each wall/polymer interface were impenetrable to the polymer but invisible to the gas.

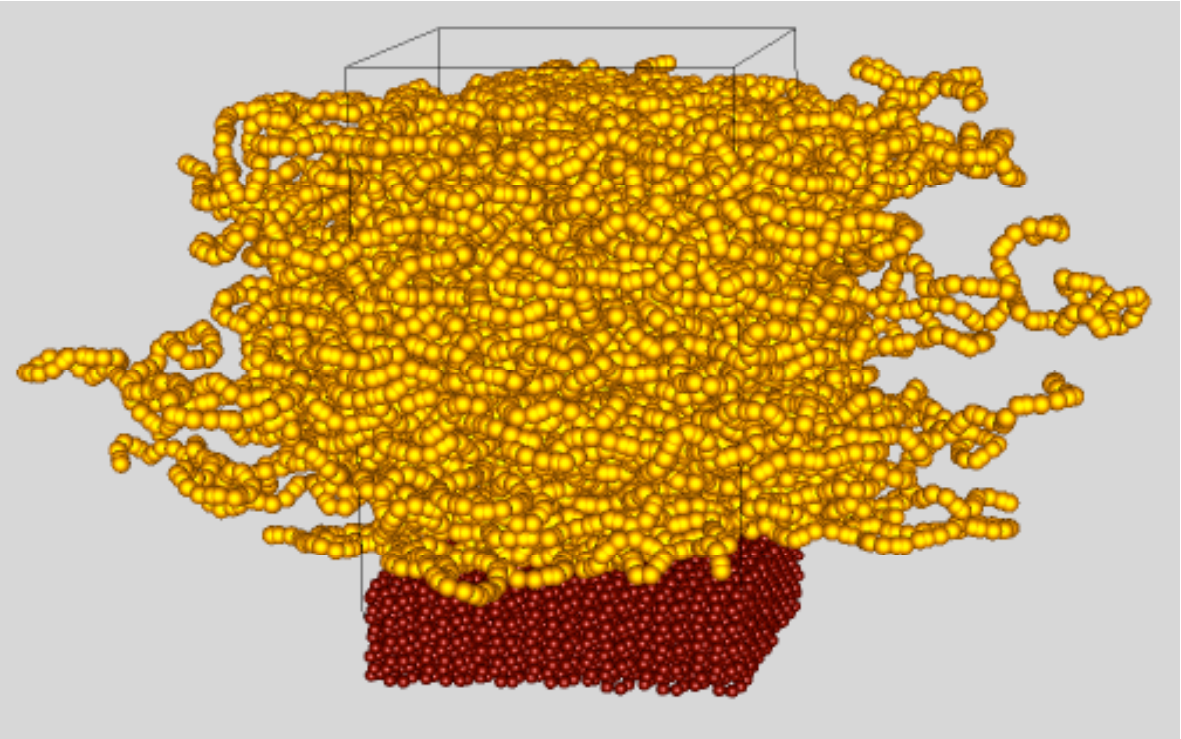

Fig. 9 *The confined ODPA-ODA polyimide model membrane.*[24]

In the second study,[25] the part of the wall which was constraining the polymer but was invisible to the gas probe was removed. Only the middle four layers of the initial diamond lattice arrangement were retained in order to prevent gas probes from escaping into the

vacuum, but there were no interactions left between the wall and the polymer. Upon removal of the wall constraint, the polymer was found to relax in the *z*-direction from a total length of ~130 Å to ~140 Å, thus leading to a free-standing membrane.[25]

In both cases, the polymer chains are significantly oriented and flattened.[24,25] This is in good agreement with published results on confined[113-115,117-119,121] and free-standing membrane models,[102-106,120,122-129] although most of them deal with shorter or more flexible polymers. However it is clear that the question of the preparation procedure of fully-atomistic glassy models remains open, and in the future, it would be interesting to compare it to a coarse-graining approach.[23,79,125,130] The drawback of multiscale approaches is that they require well-parametrized coarse-grained models of the polymers, something which we do not have yet for our polyimides. Coarse-graining has actually been applied elsewhere to three BPDA-based polyimides bulk models,[131] but the obtained model densities were surprisingly low, thus suggesting that it is not particularly straightforward.

3.3. Curved interfaces for amorphous polymers

Curved interfaces are typically found in simulations of solid nanoparticles embedded in a polymer matrix. Please note that we restrict ourselves here largely to fairly spherical fillers and do not consider particular cases such as, for example, nanotubes.[132] Much work has been reported on particles of different geometric forms and without much atomistic details combined with short polymers. For example, Monte Carlo calculations have been carried out on dense polymer melts containing solid spherical nanoparticles in continuous space.[115,117,133-137] MD has also been used on fairly coarse-grained models of icosahedral[138-140] or spherical[141,142] particles in order to investigate particle-polymer interactions, aggregation/dispersion as well as viscoelastic properties. Unfortunately, calculations become a lot more expensive when nanoparticles are to be described with atomistic details and, thus, the simulation boxes usually only contain one nanoparticle surrounded by the polymer matrix. Brown et al. have carried out MD simulations of a purely-ionic silica nanoparticle of diameter ~4.4 nm embedded in a 30000-sites united-atom CH_2 matrix.[143] A more realistic model of the silica particle, consisting of an amorphous core linked to a surface coating, was then designed

and inserted into a ~26400-atom model of PBMA in order to compare MD simulations to real PBMA-silica composites.[78,144] The long and stiff polymer chain was found to adapt badly to the inclusion on the MD timescale and remained highly correlated to its starting structure.[78,144]

As in the case of planar interfaces, specific techniques obviously need to be developed to eliminate this artefact. Within this context, we have recently built a realistic model of the silica nanoparticle,[78,144] but by considering shorter (9 monomers) and flexible PEO chains in the melt so that complete decorrelation of the starting structures could occur on the timescale available to standard MD simulations. The idea was to compare two types of end-groups for the PEO chains, $-CH_3$ and $-CH_2-OH$, and to characterize their respective influence on adsorption at the silica surface, which has been shown experimentally to be significant.[22,145-151] PEO melts with different end-groups were prepared using the hybrid PMC-MD sampling technique and then totally decorrelated at 400 K.[22]

The silica nanoparticle is an hybrid model[22] consisting of an amorphous ionic core[152] described by the BKS model[153] for pure SiO_2, which is linked to an actual surface coating. Specific intramolecular and partial charge interactions[143,154] are added to all atoms being defined as part of the surface, *i.e.* the surface silicons, the oxygen atoms bridged between two surface silicons, the non-bridging oxygens atoms linked to only one surface silicon and the silanols hydrogens linked to the non-bridging oxygens. This fully-atomistic description allows for fine-tuning of the surface thickness and number of OH groups *per* unit surface area whilst maintaining the ionic characteristics of the silica core.

The creation of a nanoparticle was carried out in several steps (Fig. 10). A cubic box of α-quartz was first built and simulated at room temperature using the BKS model.[153] It was then softly « amorphised » by modifying the non-bonded parameters in order to decrease the interactions between Si and O. Following compression back to ~2200 $kg\,m^{-3}$,[155] the full potential was progressively reintroduced. In order to create a roughly spherical silica filler, a series of initial particles were cut out with target radii of 15-17 Å and the connectivity of each surface layer was progressively defined by an iterative algorithm using 1.9 Å as a bonding criteria. Following the surface reorganization, the final nanoparticle had a radius of ~15 Å,

consisted of 1093 atoms and presented a α_{OH} = 4.4 OH nm^{-2}, *i.e* very close to the experimental Zhuravlev constant of α_{OH} = 4.6 OH nm^{-2} for a surface hydroxylated to the maximum degree.[156] It represented a volume fraction of ~8% in the PEO-silica mixtures. Another advantage of this fine-tuning procedure is that the different types of silanol groups could be distinguished. Our model nanoparticle had 82% ≡SiOH, 17% =Si(OH)$_2$ and 1% -Si(OH)$_3$. This is in good agreement with the experimental results which give roughly 87% ≡SiOH and 13% =Si(OH)$_2$ for α_{OH} = 4.6 OH nm^{-2}.[156] It is also worth noting that the nanoparticle obtained in this way had a certain roughness, as should be expected:

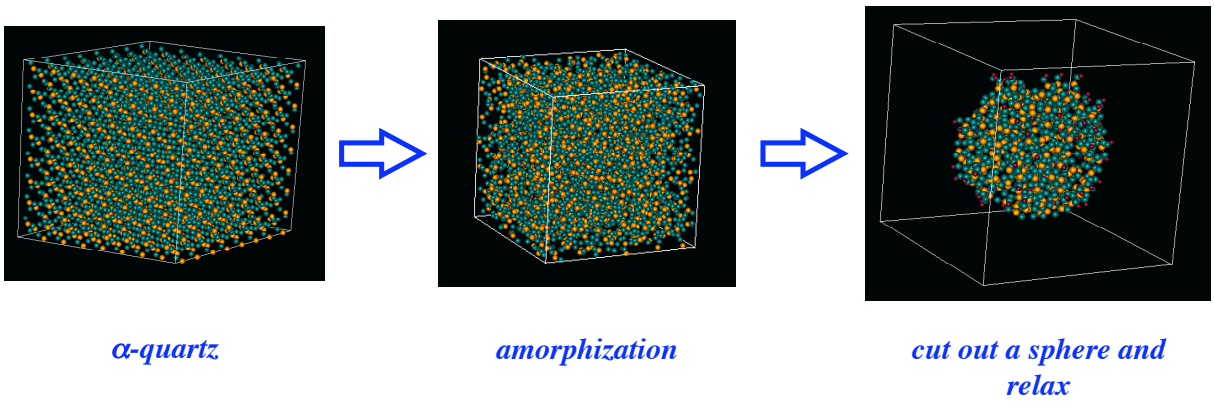

Fig. 10 *Creating a realistic model of a silica nanoparticle.*[22]

The technique for merging the nanoparticle with the polymer melt is described in detail elsewhere[143] and is summarized in Fig. 11:

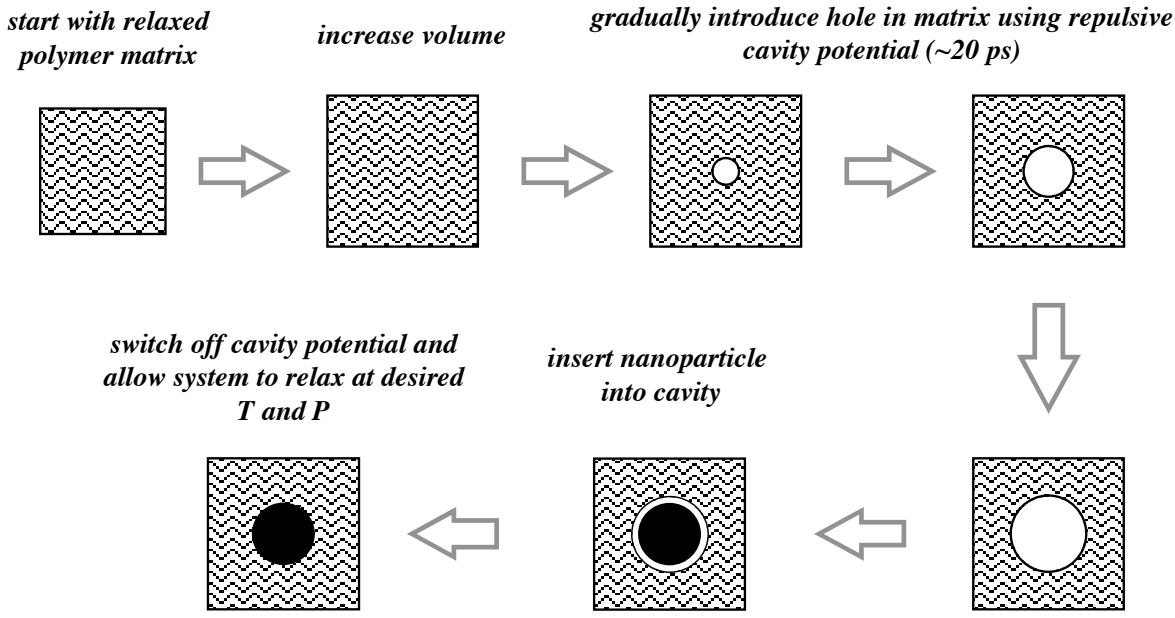

Fig. 11 *Insertion of the nanoparticle into the polymer matrix.*[22]

The pre-prepared relaxed polymer matrix is expanded and a cavity slightly bigger than the nanoparticle (radius of ~17 Å) is progressively created in its center using a soft repulsive potential U_{cav}:

$$U_{cav}(r_i) = \frac{1}{2} k_{cav} \left(\left| r_i - R_0 \right| - r_{cav} \right)^2 \; for \left| r_i - R_0 \right| < r_{cav} \qquad (13)$$

where k_{cav} is an arbitrary force constant equal to 50 kg s^{-2}, r_i is the current position vector of polymer atom i, R_0 is the centre of the MD box and r_{cav} is the current radius of the cavity. The nanoparticle is then inserted into the spherical cavity. Following the definition of appropriate cross-terms for PEO-nanoparticle interactions[22] and a short minimization run, the systems are switched to *NpT* conditions at the appropriate temperature. In that specific case, the equilibration runs were carried out until the PEO chains were totally decorrelated from their starting structure, *i.e.* of the order of one or two nanoseconds at 400 K. Production runs were then extended and a schematic representation of the hydroxyl-terminated PEO-silica system is given in Fig. 12:

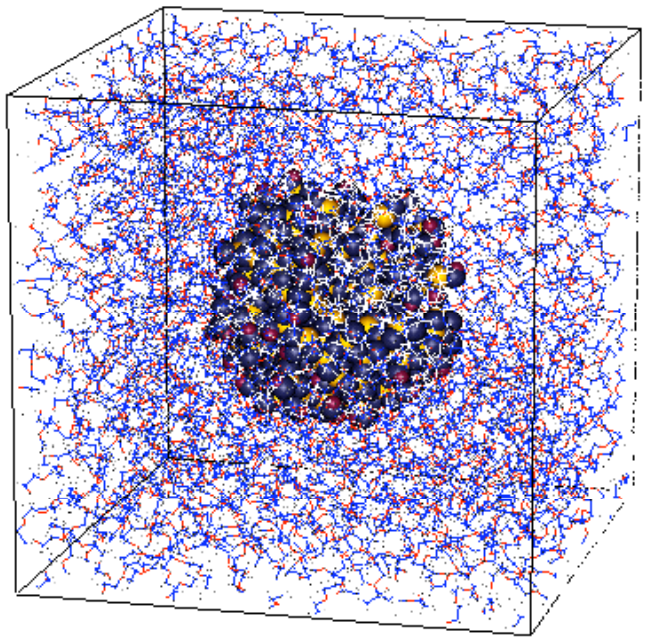

Fig. 12 *A 270-chain 22693-atom PEO-silica simulation box. The polymer and nanoparticle are represented in wire-frame and space-filling models respectively. PEO molecules in the top front right corner have been removed in this display in order to better reveal the nanoparticle.*[22]

3.4. Crystalline polymers

Crystalline polymer models are *a priori* a lot easier to set up, since the atomic coordinates are usually based on data obtained from X-ray experiments. In addition to specific properties of polymer crystals, the structure can then be used to optimise and validate a particular force-field. We have first developed a specific force-field for pure PEO[3,8] by comparing the simulation data to the experimentally determined geometry of the crystallographic monoclinic unit cell:[157] a = 8.05 Å, b = 13.04 Å, c = 19.48 Å and β = 125.4° (Fig. 13):

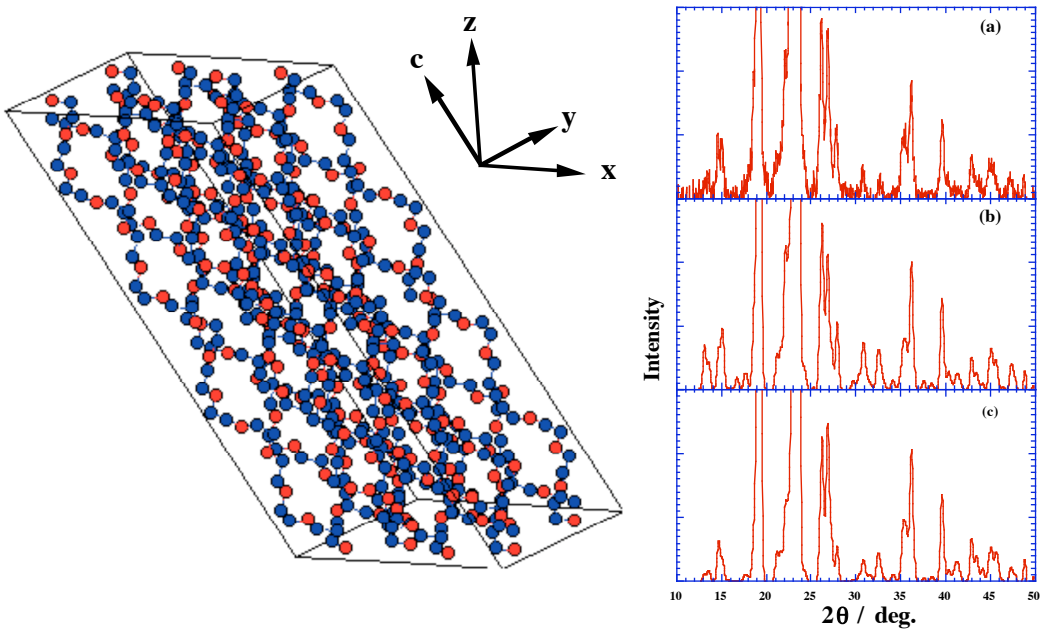

Fig. 13 *Left: crystalline PEO (blue = C, red = O, H not shown) in an MD box constructed from eight crystallographic unit cells. Right: X-ray powder diffractograms for PEO: (a) experimental; (b) calculated using the published refined coordinates[157] (c) calculation as in (b) but using average atomic coordinates obtained from MD calculations with the optimised selected force-field.[3,8]*

This pure PEO force-field was then transferred to describe PEO-PEO interactions in a known PEO/salt crystal structure, PEO_3NaI.[158] Additional ion-ion and ion-polymer interactions had to be adjusted in order to give a realistic model of PEO_3NaI in the crystalline phase (Fig 14):[5]

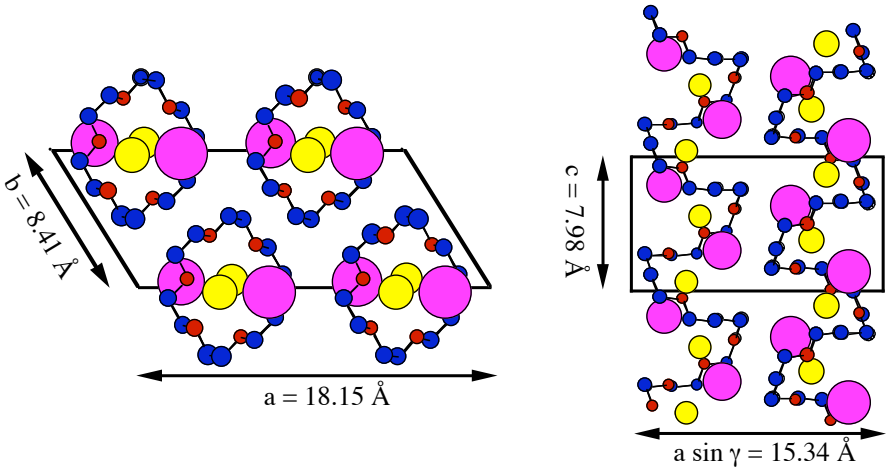

Fig. 14 *Crystalline PEO_3NaI (blue = C, red = O, H not shown, yellow = Na, purple = I) viewed down the c axis (left) and along the b axis (right). The cell parameters are a = 18.15 Å, b = 8.41 Å, c (fibre axis) = 7.98 Å, γ = 122.3°.*[158]

Both the PEO and PEO/NaI models were later found to transfer very well too to the corresponding amorphous phases,[4,6,7,9,10,12,14,22] thus showing the strength of force-field verification based on known crystalline structures. Similar approaches have also proven successful for PEEK and more recently for PTFE (Fig. 15):

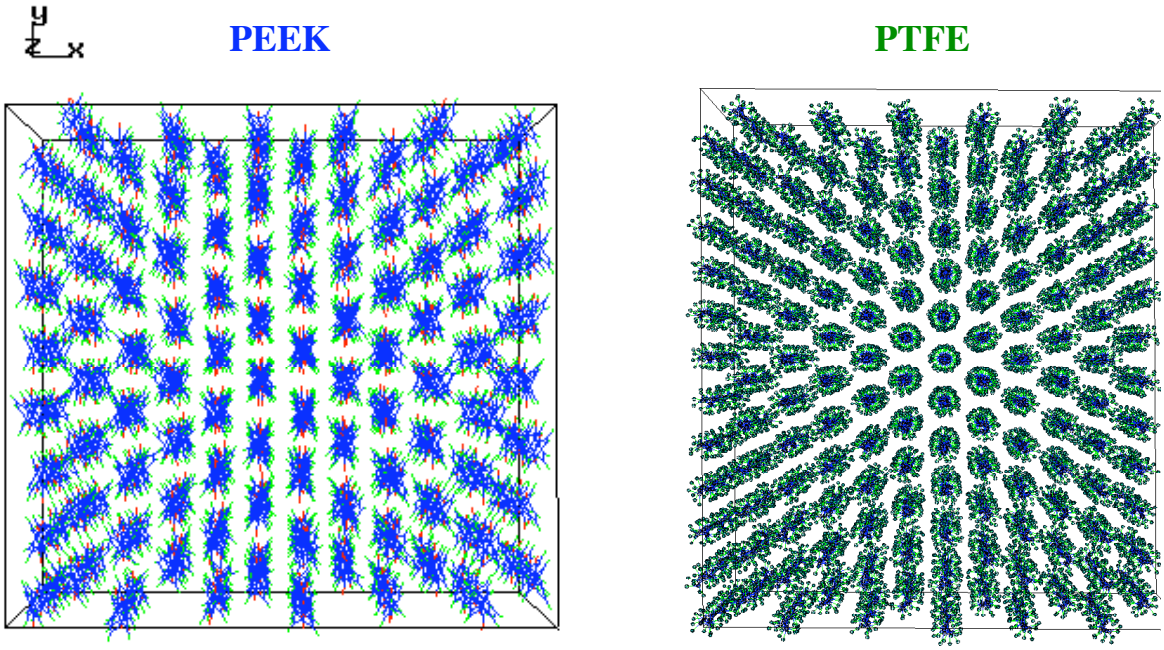

Fig. 15 *MD simulation boxes based on experimentally refined X-ray data for PEEK*[159,160] *and for the phase II of PTFE (T<273 K).*[161]

On the other hand, we have attempted to reproduce the phases of the native I-α and I-β forms of crystalline cellulose I using the only available crystal data at the time,[13] *i.e.* the probable dimensions and shapes of the unit-cells[162] in the absence of any published refined coordinates.[13] Following more recent *ab initio* work on the energy of rotation around the C5-C6 bond in α-D-glucose,[163] the torsional potential of the hydroxymethyl group had to be re-parametrised,[23] thus casting doubts on the results predicted by the original force-field.[13] It is clear that the experimental data must be fairly reliable in order to be able to carry out such validations.

With respect to the problems encountered with crystalline cellulose, it should be mentioned that, in principle, MD can be used in the absence of any structural information to predict *ab initio* polymer crystal structures. However, such simulations require that a certain number of basic hypotheses are made concerning the crystal structure and that only a small number of plausible starting structures are considered. An example is the synthesis at the LMOPS of a poly(3-acetamido-undecanoic-succinimidyl-thiophene) in order to understand how the side chain would affect its molecular structure.[19] In that specific case, powder X-ray diffraction gave limited information, with only the average interlayer spacing being easily accessible. Since regioregular polythiophenes are known to pack relatively easily,[164-167] it was assumed that the side chains would be stretched out on either side of the polythiophene backbone and that the polymers would align such that their backbones were either parallel or antiparallel to each other. In addition, various numbers of 20-*mers* molecules were considered along the *x* and *y* axis, but the order was 1 along the *z* axis. Using the generic TRIPOS force-field,[168] the lowest energy structure was found to be an antiparallel one as schematised in Fig. 16.[19] Stability was achieved by interpenetrating the acetamido-undecanoic-succinimidyl side-chains. A comparison of a X-ray diffractogram derived from the MD-averaged positions of the atoms with the experimentally-obtained pattern supported the conclusion that the model presented in Fig. 16 is indeed a good candidate for the crystalline structure of poly(3-acetamido-undecanoic-succinimidyl-thiophene):

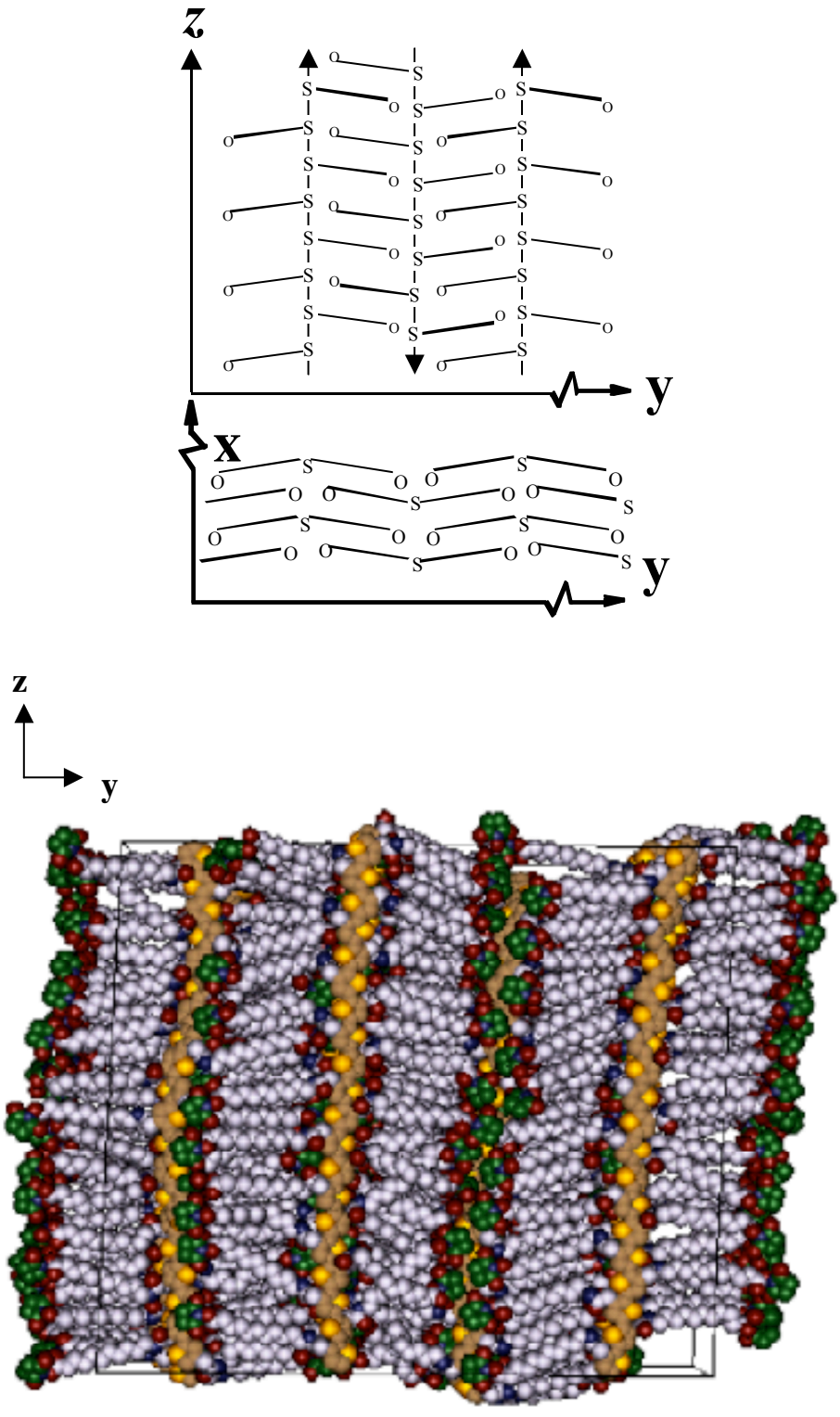

Fig. 16 *Prediction of the crystalline structure of poly(3-acetamido-undecanoic-succinimidyl-thiophene): white = alkyl C, red = O, blue = N, green = succinimide ring C, yellow = thiophene ring S, beige = thiophene ring C. The model shown is that with the highest final degree of order.*[19]

4. IONIC TRANSPORT IN PEO-BASED POLYMER ELECTROLYTES

Flexible polar polymers are often used as the basis for solid electrolytes, since they can dissolve ionic species and form highly conductive materials.[26] High molecular-weight PEO is especially suited as a polymer host in ion-polymer batteries because of its availability, low toxicity, high chemical stability, and its ability to solvate a wide variety of inorganic salts ranging from alkali, alkaline earth, lanthanide to transition metals.[169-173] The distance between electron-donor oxygens on the PEO backbone is optimal for them to efficiently coordinate with the cations and compensate for the lattice energy of the salts.[170,174] In addition, the low barriers to rotation around the polymer backbone bonds (2.26 kcal mol^{-1} for C-C bonds and 1.75 kcal mol^{-1} for O-C bonds)[175] should allow for substantial mobility in the amorphous phase.[172,174] The major drawback of PEO lies in its tendency to crystallize in helical structures under ambient conditions.[157,169,172,173] Crystallinity can be reduced by adding plasticizers,[176] irradiation crosslinking[177] or limiting the oxyethylene lengths in a variety of copolymers.[178] Related systems based on completely amorphous polymers such as poly(propylene oxide), PPO,[179] have also been investigated, but they usually do not exhibit the same combination of properties as PEO.

It has been known from fairly early on that ionic transport in PEO-based systems is likely to involve correlation between ion and polymer motion,[170,172,174] but the situation is further complicated by ion association[174,180-183] and a range of other processing factors such as storage or hydration.[178,184-188] The actual mechanisms of lithium motion at the atomic level were first examined in the mid-nineties by Müller-Plathe et al., using MD with adequate preparation procedures and simulations times in a series of simulations of PEO/LiI systems[89,189,190] and later confirmed.[191]

About the same time, we transferred our force-field optimized on crystalline PEO [3] and crystalline PEO_3NaI [5] (see Section. 3.4.) to amorphous PEO_xNaI systems, in order to examine their local structure and mobility as a function of both ionic concentration and temperature.[6,7,9,12] An amorphous relaxed chain of PEO was generated at 400 K by PMC sampling[4,10] and found to relax towards an average density for the bulk melt of 1092±2

kg m^{-3}.[4] Despite the reservations detailed in Section 3.1. about the application of our generation procedure to the specific case of PEO, the fact that the density of the amorphous model agrees with experimental evidence[4,192,193] and that the P-V curve is also well reproduced[14] is reassuring. In addition, the PEO chains are flexible enough to relax locally and conformationally on the MD timescale at 400 and 500 K, and the main interest lies in the local structure and dynamics of the ions within the polymer matrix. Na^+ and I^- ions in appropriate numbers were then distributed randomly in the periodic MD box of the PEO-sample at 400 K in order to create amorphous PEO_xNaI systems at three EO:NaI ratios (x = 48, 20 and 3). At the same time, further runs were carried out at 500 K along with separate simulations of pure NaI at both 400 and 500 K. A comparison of the specific volumes and the energies for pure and mixed systems supported the visual evidence that all PEO_xNaI systems (see Fig. 17 for PEO_3NaI) were single-phase under the conditions specified.[6,7,9]

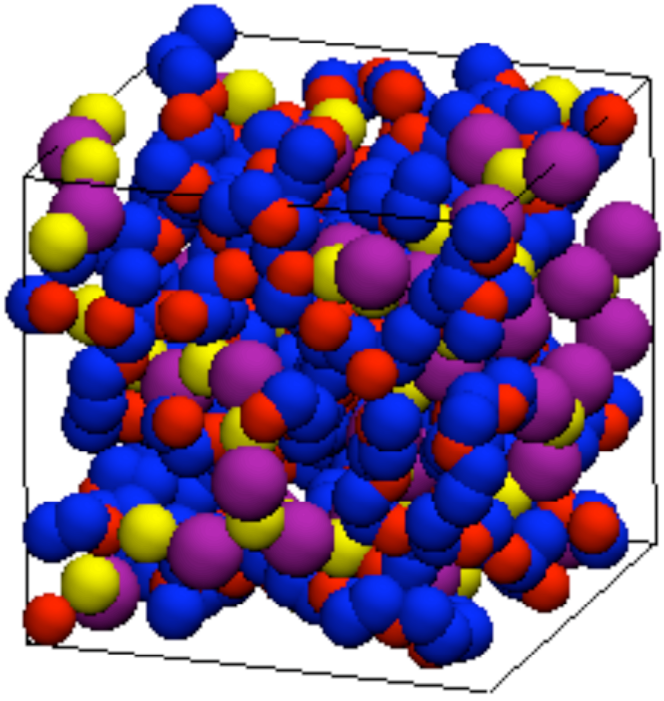

Fig. 17 *A schematic representation of the PEO_3NaI polymer electrolyte (blue = C, red = O, H not shown, yellow = Na, purple = I). The atoms have been "folded back" into the cubic periodic box.*

4.1. Polymer flexibility

The conformation of the polymer upon ion introduction remains on the whole relatively similar to that of pure PEO.[6] In all cases, the backbone CCOC angles were mainly found in the *trans* well, while the OCCO stayed mostly *gauche*.[89,194-196] To evaluate the effect of salt concentration and temperature on chain mobility, the normalized autocorrelation functions $C_{TT}(t)$ for the *trans* state of the CCOC angles were calculated using the form given in Eq. 9. For statistical reasons, the $C_{GG}(t)$ for the *gauche* state of the OCCO angles were defined in the same way from:

$$R_{GG}(t) = \frac{\left\langle H_{G-}\{\tau_i(0)\}H_{G-}\{\tau_i(t)\}\right\rangle + \left\langle H_{G+}\{\tau_i(0)\}H_{G+}\{\tau_i(t)\}\right\rangle}{2} \qquad (14)$$

with $H_{G-}\{\tau_i(t)\}$ and $H_{G+}\{\tau_i(t)\}$ being the characteristic functions of the *gauche- and gauche+* states respectively for dihedral τ_i at time t. The normalized form of the correlation function, $C_{GG}(t)$ is given by:

$$C_{GG}(t) = \frac{R_{GG}(t) - \langle X_G\rangle^2}{\langle X_G\rangle - \langle X_G\rangle^2} \qquad (15)$$

with $\langle X_G\rangle = R_{GG}(0)$ being half the mean fraction of the angles in the *gauche* conformation. These normalised relaxation functions are displayed in Fig. 18 for pure PEO and the three salt concentrations:

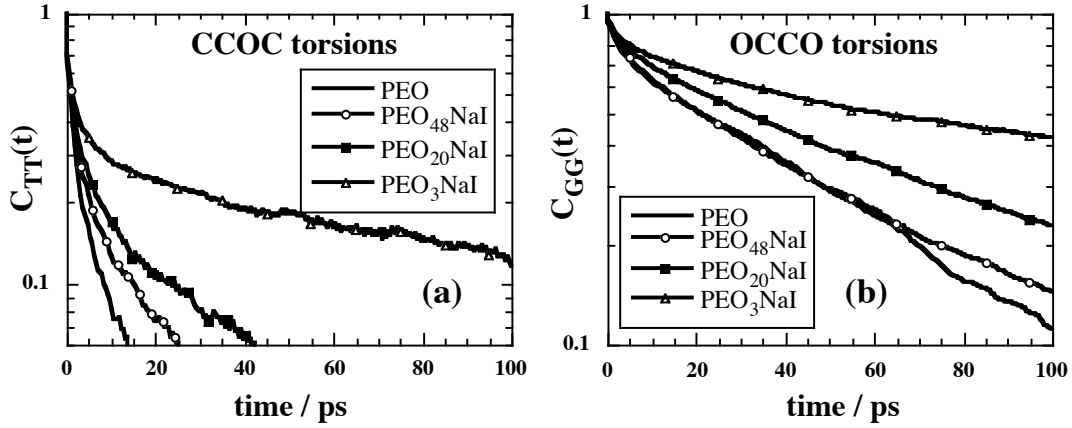

Fig. 18 *The normalized relaxation functions $C_{TT}(t)$ (Eq. 9) and $C_{GG}(t)$ (Eq. 15) for (a) CCOC and (b) OCCO torsion angles. The results for the three PEO_xNaI systems are compared at 500 K to those for pure PEO.*[6]

Both plots show the same general trend towards reduced polymer chain flexibility with increased ionic concentration. This correlates with the observation that glass-transition temperatures increase as salt is added[197] and with NMR-studies, where broader proton contributions to the spectra appear upon dissolution of salts in the PEO-host.[183] As expected, heating increases chain kinetics and relaxation rates, but the systems have the same qualitative behaviour at 400 and 500 K. In addition, the model relaxation times are in good agreement with the value of ~10^{-10} s reported for the segmental motions of the polymer chain.[170,198,199]

4.2. Local structure

Both radial pair distributions functions g(r) as a function of the distance r between cations and polymer oxygens on the polymer backbone, $g_{Na...O}(r)$, or that between cations and anions, $g_{Na...I}(r)$, were seen to exhibit a first strong structural peak at ~2.4-2.5 Å, with a trough at ~3.8 Å.[6] This indicates that a sodium is able to coordinate to both oxygens and iodines, thus leading to "NaO_mI_n complexes", with 3.8 Å being chosen as the limit for the first coordination shell. The g(r) were then integrated to give the average numbers, n(r), of oxygens and iodines around a sodium.[6] Results are summarized in Fig. 19:

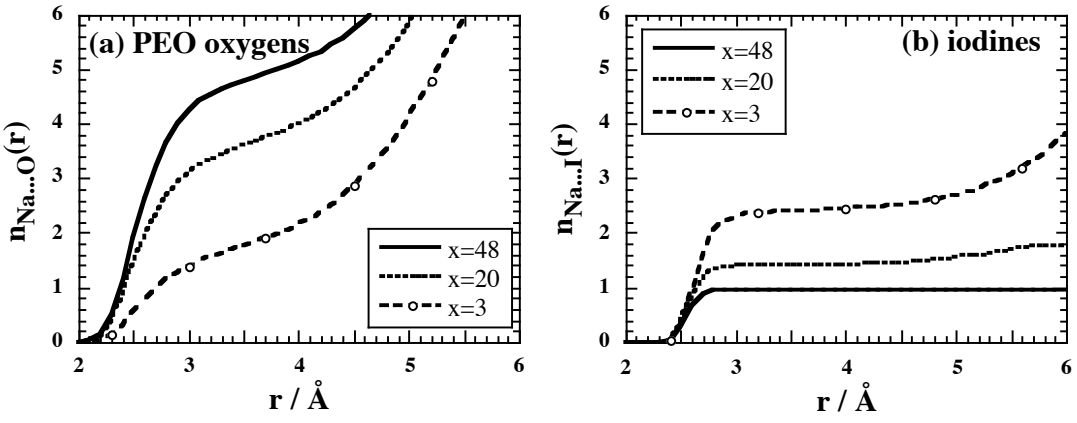

Fig. 19 *The average number of (a) oxygens and (b) anions within a distance r of a cation at 400 K. x is the EO:NaI ratio.*[9]

The average number of oxygens in a distance r of the cation clearly decreases with increasing salt concentration, while the average number of iodines within the same distance increases. These opposite trends, which are found at both temperatures under study, reflect the

competition between backbone oxygens and anions for cation coordination, which becomes unfavourable for the polymer as the concentration of ions increases. Such a behaviour is consistent with experimental evidence on the subject.[172,174,181,182] The $n_{Na...O}(r)/n_{Na...I}(r)$ coordination ratio varies from ~5/1 for $x = 48$, to ~4/1.5 for $x = 20$ and settles around ~2/2.5 for $x = 3$, with the decrease in the total coordination number being related to the larger size of the iodine ion. In amorphous PEO_3NaI, all 96 ions form an extended network intertwined with the polymer chain at both temperatures under study.[6] The presence of this percolating cluster is in agreement with the failure to describe ion motion in terms of isolated clusters for high EO:salt ratios.[172,182,200]

Although the analyses of the composition of the cation first cordination sphere suggest a slight salt concentration dependence, most structural features are shared by all systems under study. Many combinations of (*m*,*n*) values are seen for the NaO_mI_n complexes,[9] but the NaO_3I_2 complexes and its direct derivatives, *i.e.* where the iodines are replaced by two oxygens, NaO_5I_1 and NaO_7I_0, are clearly favoured at both low-salt concentrations. These three (*m*,*n*) combinations are basically equivalent in terms of steric considerations and seem to represent the optimal geometry for coordination to the cation. In PEO_3NaI, NaO_3I_2 is still prevalent, but the oxygens tend to be replaced by iodines leading to give NaO_0I_3, NaO_1I_3 and NaO_2I_2 complexes. As far as the position of the oxygen ligands on the PEO chain is concerned, the cations appear to be preferentially coordinated by up to 6 continuous oxygens on the same strand of polymer, reminiscent of the multidentate coordination of the crown-ethers which form stable complexes with Na^+.[201,202] The probability density distributions of $O^{\cdots}Na^{\cdots}O$ angles (close to 60°, see Fig. 20), $O^{\cdots}Na^{\cdots}I$ angles (close to 100°), and angles between planes of contiguous $O^{\cdots}Na^{\cdots}O$ entities (close to 0°) reveal that PEO segments usually coordinate to the cations in near-planar conformations with the anions being placed above and/or below the $PEO\cdots Na^+$ quasi-plane, since such geometries result in optimal coordination of both parties to the cation (Fig. 20):

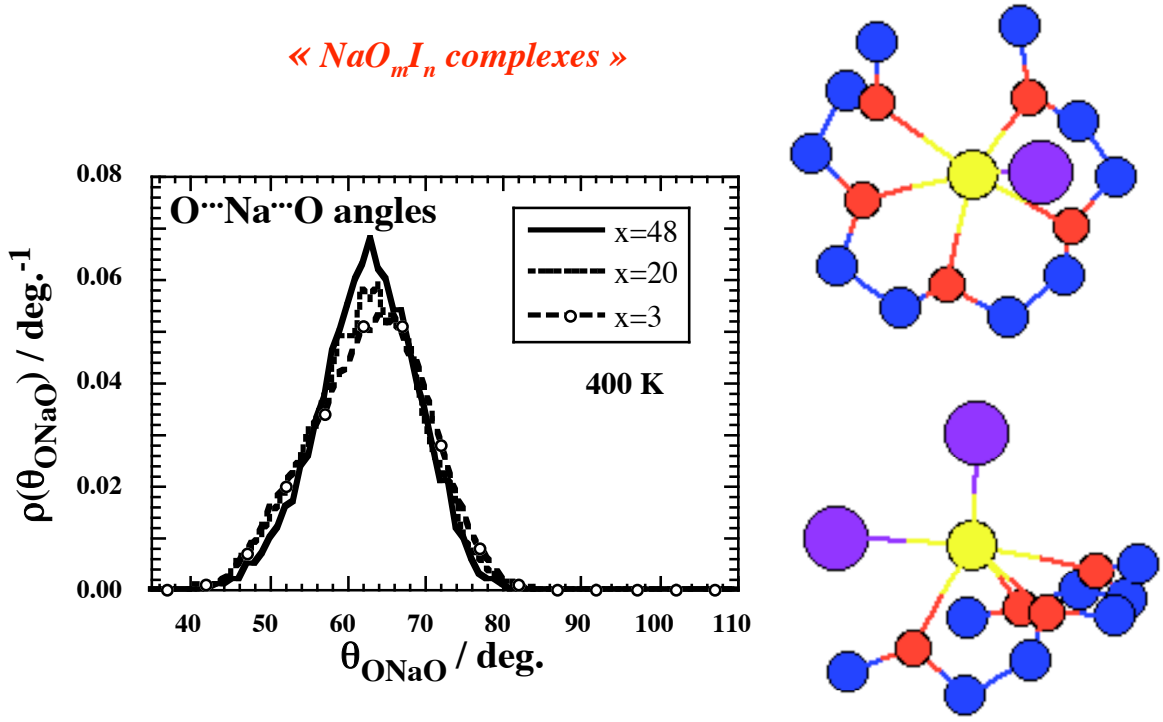

Fig. 20 *Left: normalized probability density distribution of O···Na···O angles between a cation and two nearest-neighbour oxygens belonging to its coordination sphere as a function of EO:NaI ratio. Right: views of NaO_mI_n complexes. "Bonds" have been drawn between the cation and its ligands separated by at the most 3.8 Å. (blue = C, red = O, H not shown, yellow = Na, purple = I).*[9]

4.3. Local dynamics

Diffusion coefficients of ions in high molecular-weight PEO are typically found in the range 10^{-7} to 10^{-6} cm^2 s^{-1}.[203,204] Although mean-square displacements (MSD) can easily be calculated for species of either types, they were statistically uncertain over the nanosecond simulations, prone to erratic behaviour and differed substantially depending on which part of the simulation was analyzed.[6] These problems remained even when the ionic mobility was artificially enhanced by using scaled-down coulombic interactions.[89,189,190] The Einstein regime for diffusion, which can be identified by the MSDs being directly proportional to time *t*, could not thus be reached and there was little meaning in trying to extract quantitative long-range diffusion coefficients from these output data.

On the other hand, the erratic behaviour of the MSDs could be traced to the occurence of distinct diffusional steps. Indeed, the average number of ligands around a specific sodium fluctuates with time, thus suggesting dynamical changes in its coordination sphere. To follow this evolution, all oxygen and iodine atoms that came within a radius of 3.8 Å of each sodium were identified, and their position with respect to this sodium monitored with time. It was soon clear that significant "jumps" occur, as can be seen from Fig. 21. Behaviour patterns include the replacement in the coordination sphere of two oxygen atoms by an iodine atom, either on a 20 ps (Fig. 21a) or a much shorter timescale (Fig. 21b), as well as the reverse effect, the replacement of an iodine by oxygens (Fig. 21c). Oxygens on the polymer chain can also replace each other (Fig. 21d):

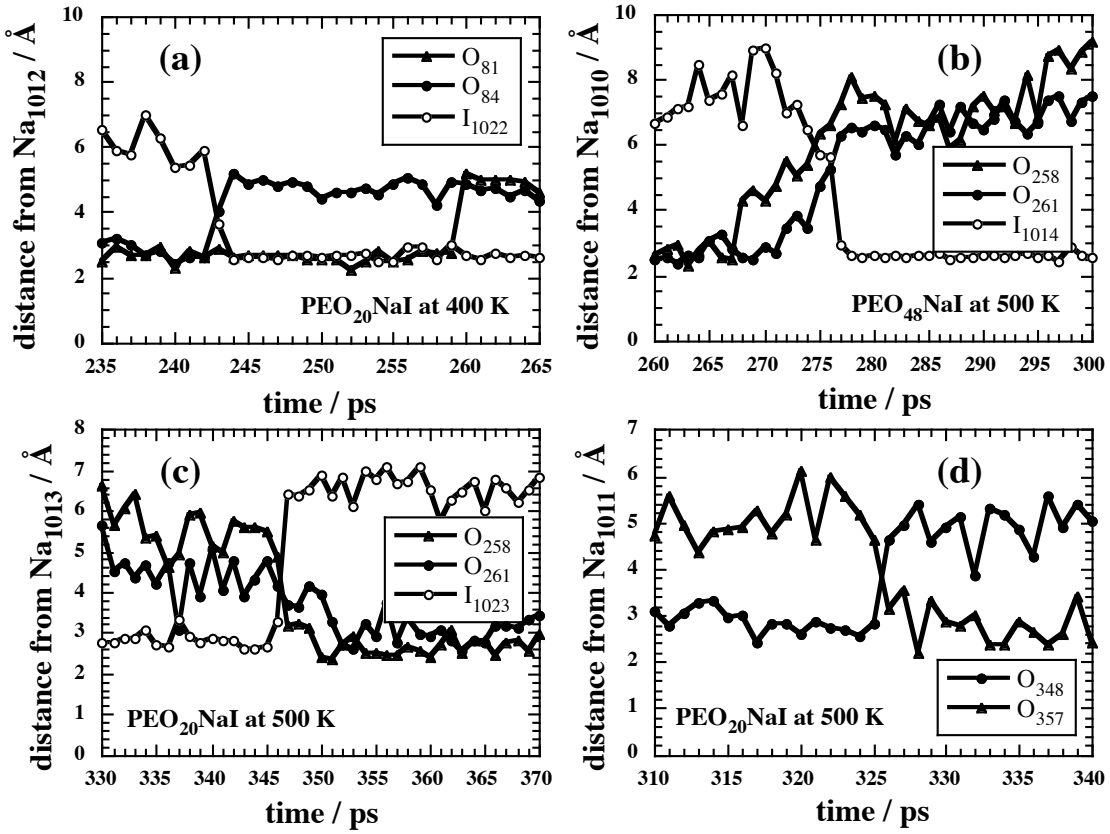

Fig. 21 *Examples of the dynamics of changes in the coordination shell around cations. The system used to label particles means that contiguous oxygens along the chain differ in index by three and ions indices begin at 1010.*[6]

The hopping timescale displayed in Fig. 21 is consistent with the values of $\sim 10^{-12}$ s reported in the literature,[198] and the local environment of the cation evolves faster at the lower salt concentrations ($x = 48$ and $x = 20$), where the polymer is relatively unconstrained. An example of the progressive motion of a cation along a polymer chain is best seen in Fig. 22, which follows the evolution of a sodium coordination sphere over 1000 ps. The sodium remains coordinated to an anion over the time of the simulation, but clearly 'glides' along the neighbouring oxygens of the polymer chain (Fig. 22):

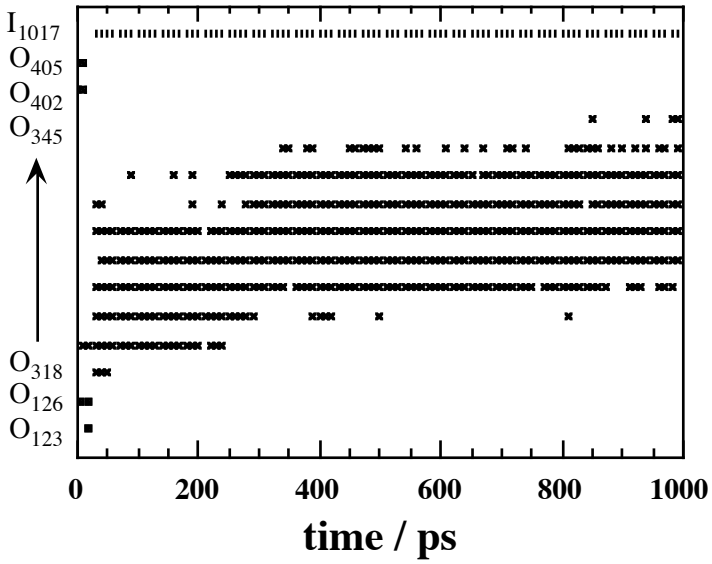

Fig. 22 *1000-ps time evolution of the local environment around a sodium in the $PEO_{20}NaI$ system at 400 K. The nine contiguous oxygen atoms belonging to the O_{318}-O_{345} PEO segment are indicated by crosses and the iodine ligand by bars. The square symbols identify those oxygen atoms that are only coordinated at the start.*[6]

The formation of ion pairs or even higher clusters thus does not prevent ionic mobility. Patterns of motions are varied and correlated motion around a cation involving different polymer segments close in space is not uncommon either. Schematic representations of a series of jump events occuring in our simulations are given in Figs. 23, 24 and 25. As before, "bonds" have been drawn between the cations and their ligands at the time of the snapshot. Fig. 23 displays a Na jump between neighbouring sites on the polymer chain. The high

flexibility of the PEO chain clearly results here in a net correlated motion of the ion triplet along the polymer backbone (Fig. 23):

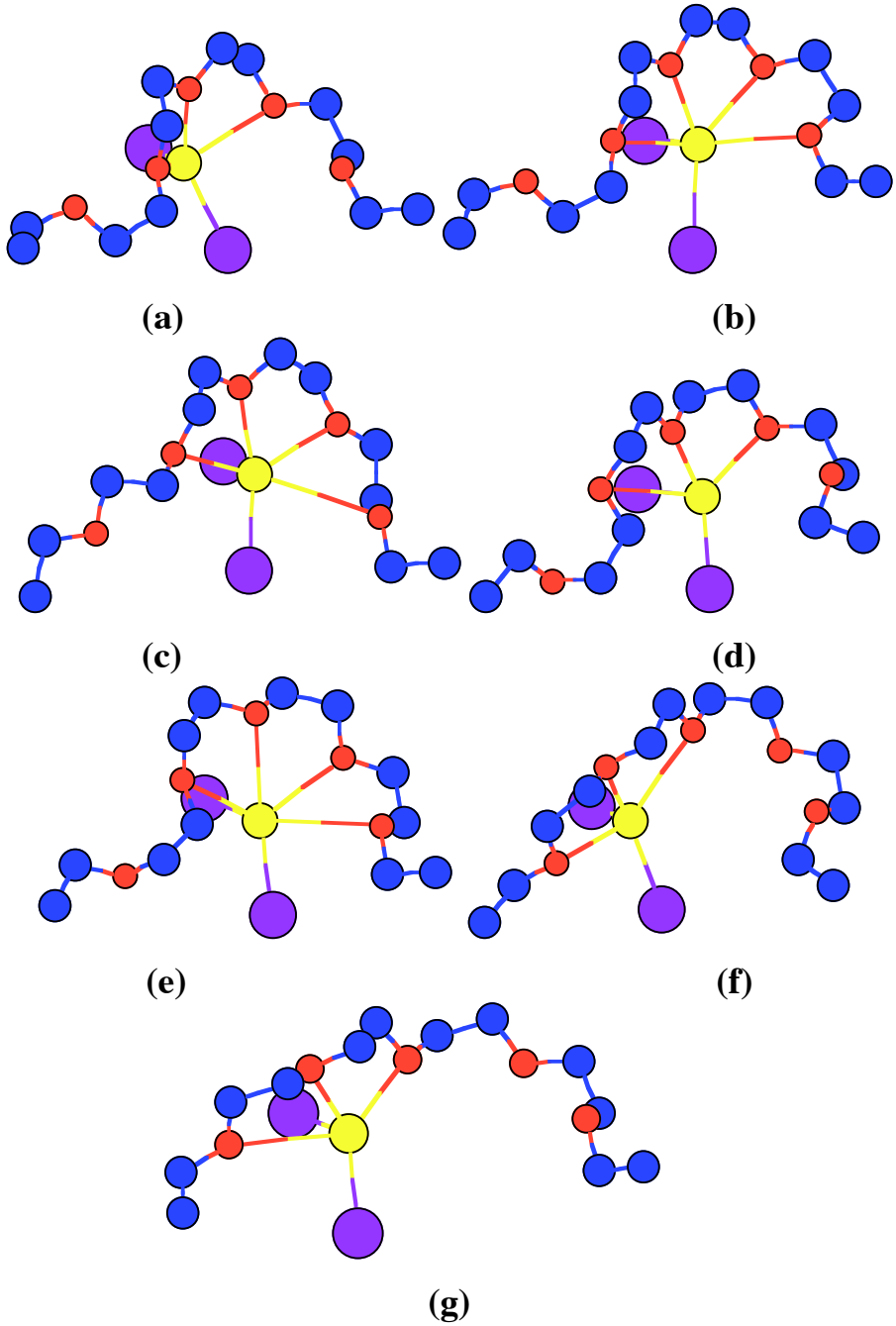

Fig. 23 *Cation jump between neighbouring sites on the PEO chain. Please note that in all these snapshots separated by 1 ps, exactly the same atoms are displayed and the viewing angles are identical. The sequence is taken from the simulation of the* $PEO_{20}NaI$ *system at 500 K (blue = C, red = O, H not shown, yellow = Na, purple = I).*[9]

In Fig. 24, two oxygen ligands are progressively replaced by an iodine which enters the coordination sphere of the cation. It should be noted that this cation is initially coordinated to oxygens situated on two different segments of the polymer chain (Fig. 24a). The formation of the ion pair is followed by the loss of oxygen ligands from a single polymer segment (Fig. 24d):

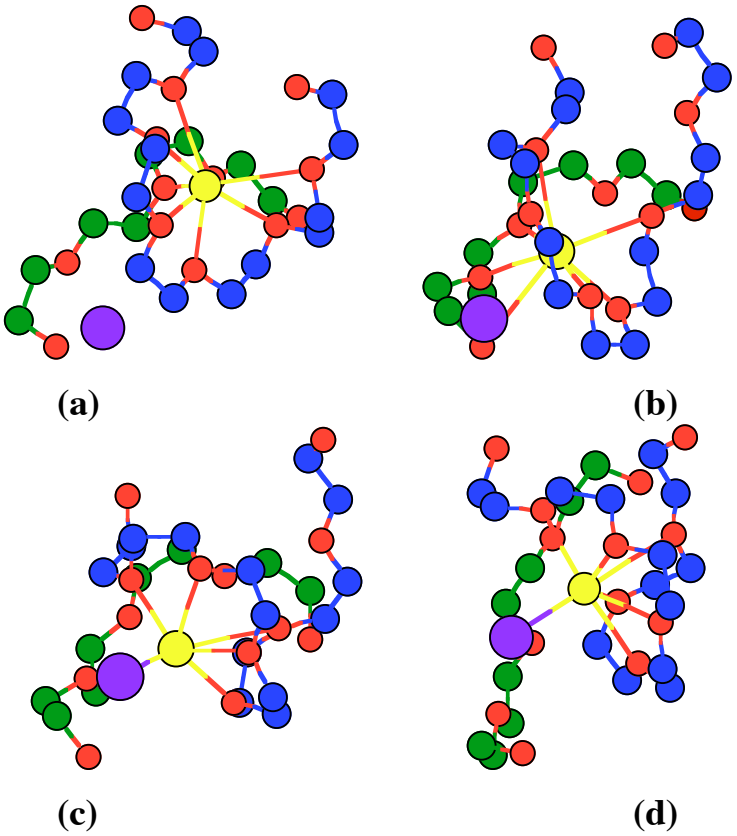

Fig. 24 *Replacement of two oxygen ligands by an iodine in a sodium coordination shell. Key is as Fig. 23 except that the blue and the green atoms are C belonging to different parts of the polymer chain. This sequence is taken from the* $PEO_{48}NaI$ *system at 500 K at three ps intervals.*[9]

Fig. 25 shows the reverse situation, *i.e.* the replacement of an iodine ligand by oxygens in a cation coordination shell. A large NaI_3 cluster relieves its steric and electrostatic constraints by coordinating as a triplet to the polymer chain:

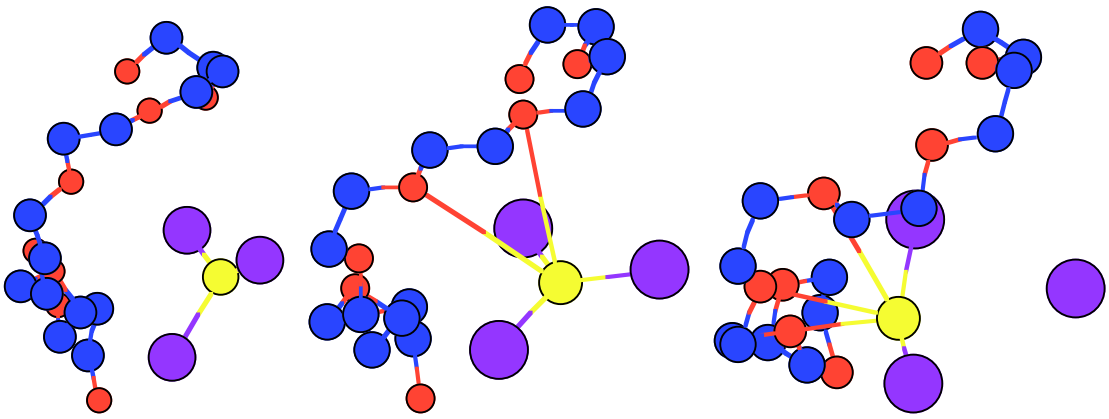

Fig. 25 *Replacement of an iodine ligand by oxygens in a sodium coordination shell. Key is as Fig. 23. This sequence is taken from the $PEO_{20}NaI$ system at 500 K at 1-ps intervals.*[9]

Na^+ and I^- ions thus undergo a succession of events such as those shown in Figs. 23-25, which progressively modify their local environment and effectively lead to diffusion. A representation of the net motion of a cation is given in Fig. 26. The same atoms are displayed, the viewing angles are identical and snapshots are separated by 120 ps. The ion pair 'glides' along the flexible PEO chain while its configuration is altered. The correlation of polymer/ion motion results in a net displacement of the ions (Fig 26):

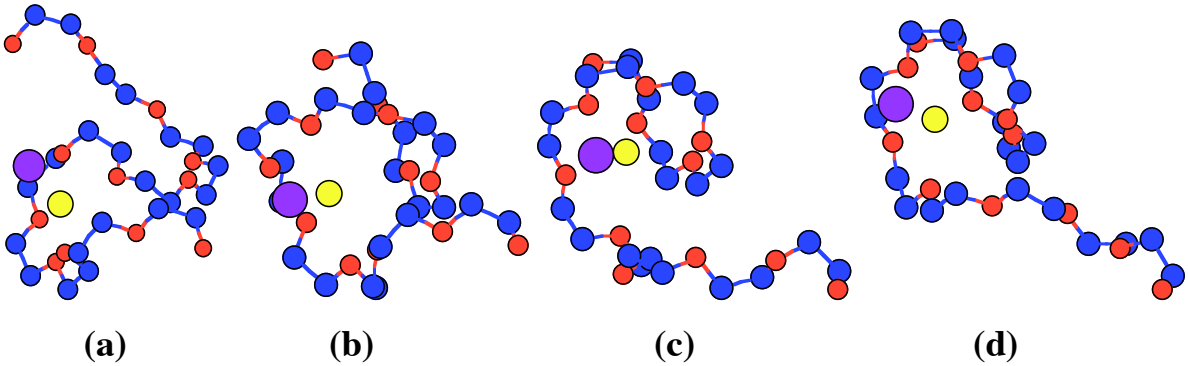

Fig. 26 *Ion pair 'gliding' along the polymer chain. Key is as Fig. 23. This sequence is taken from the $PEO_{20}NaI$ system at 400 K at 120-ps intervals. Note that the time between the snapshots is much greater than that of the preceding figures and that the "bonds" between the cation and its ligands have been removed for clarity.*[9]

4.4. Phase separation

The response of the PEO_xNaI models to a fast increase in temperature followed by a cooling phase of similar duration was also tested,[12] in order to check whether they reproduced the experimental "salting-out" effect linked to a precipitation of the salt as the temperature is raised.[205,206] The models were thus heated from 500 K to 1000 K and cooled back down to 500 K at rates of 1 K/ps. Although such a computational procedure did not allow for even quasi-equilibrium to be reached at a given temperature, interesting trends were obtained by monitoring the evolution of a number of properties.[12] Thermodynamic analyses showed that the systems underwent a net modification upon heating and that this was not fully reversible when they are returned to their initial temperature. The polymer conformations were rather insensitive to the temperature cycle but did indicate some restructuring at the highest salt concentration. Ionic association was clearly very affected for all systems under study by the rapid increase in temperature, and both Na^+ and I^- ions settled into single clusters containing all the ions in the simulations. These final phase-separated states were very stable, irreversible on the timescale of the simulations, thus reproducing the "salting-out" effect.[12]

4.5. Perspectives

The amorphous polymer electrolyte simulations outlined above obviously give a good qualitative picture of the structure and short time dynamics in PEO_xNaI systems. The succession of dynamical exchanges progressively modifies the local environment of the ions and, with the correlated flexibility of the polymer host, leads to effective ionic transport. It should be now possible to extend these simulations in order to get more quantitative measurements of diffusion coefficients and check whether they followed the same trend with increasing salt concentration as seen experimentally.

5. GAS TRANSPORT IN POLYIMIDE-BASED MEMBRANES

Polyimides are high-performance rigid macromolecules which are usually obtained via polycondensation of aromatic and/or alicylic dianhydride and diamine structures. They combine excellent mechanical and electrical characteristics over a large range of temperature, as well as good chemical and long-term stabilities.[207] In addition, they exhibit high gas selectivities and can thus be used as dense membranes for gas separation, *e.g.* for separating oxygen or nitrogen from air or for purifying natural gas.[29] The choice of their basic dianhydride and diamine monomers can be fine-tuned in order to lead to a large variety of flexibilities, mobilities and structural packings,[29,207,208] which in turn will be directly linked to the selectivity and permeability of the resulting polyimide membrane. However, it is now well-known that the membrane processing conditions are also key parameters for improving permeabilities while keeping high selectivities.[209,210]

This work was initiated by the experimental synthesis and characterization of a series of polyimides based on the flexible ODPA and the rigid BCDA dianhydrides as well as on the unsubstituted ODA, the fluoro-substituted CF_3ODA and the methoxy-substituted MeOODA diamines (Sec. 2.1.).[108-112] Several combinations of these basic fragments were used in an attempt to find interesting candidates for gas permeation applications. While over fifteen different copolyimides were actually synthesized,[109] five were chosen as test cases for a combined experimental and MD simulation study: the ODPA-ODA and BCDA-ODA homopolyimides, as well as the regular (ODPA/BCDA)-ODA copolyimide with 20% BCDA and the corresponding (ODPA/BCDA)-CF_3ODA and (ODPA/BCDA)-MeOODA copolyimides (see Sec. 2.1. for the chemical formulas).[17,20] Atomistic models of these polyimides in the bulk were built and found to be in excellent agreement with the real systems.[17,109,110] On the other hand, the calculated diffusion coefficients of He, O_2 or N_2 gas molecules were systematically higher than the experimental ones,[108] despite the force-fields being validated for both the matrices[17] and the gas molecules.[211,212] Several possible explanations for the disagreement between the models and the experiments have been put

forward[21] and this has led to a series of further simulations concerning specific features of such models, such as the influence of the model box size[21] or specific interfacial structures.[24,25] These studies are fundamental in nature and have general implications applicable to all glassy polymers and not just to the polyimides under study here.

5.1. The (ODPA/BCDA)-ODA polyimide bulk models

The effect of increasing the BCDA dianhydride content in ODPA/BCDA copolyimides was assessed by comparing the ODPA-ODA homopolyimide (0% BCDA), the (ODPA/BCDA)-ODA copolyimide (20% BCDA) and the BCDA-ODA homopolyimide (100% BCDA). Indeed, the BCDA bulky structure should make it a very strong candidate to favour the transport of small molecules in polyimide membranes. However, too much BCDA will lead to problems at the processing stage because it increases the Tg and brings it too close to the degradation zone.[108,109] In parallel, the ODA diamine was thus substituted either by a trifluoromethyl (Fig. 3) or by a methoxy group, in order to determine whether the effects at the molecular level could be similar to that of the introduction of BCDA and consequently "replace" it to a certain extent.

^{1}H NMR characterization showed that the experimental chains contained an average of forty (dianhydride-diamine) units, and that the copolyimides with 20% BCDA had regular (ODPA-diamine)$_4$-(BCDA-diamine) sequences.[108,109] Although less ordered structures were also detected, the model chains were all built using hybrid PMC-MD sampling[15] according to the above indications. In the absence of any experimental evidence, only the lowest-energy boat-boat conformation of the BCDA fragment was considered. There were ~2100-2200 atoms *per* polyimide chain and, at the start, three chains *per* simulated system.

5.1.1. Bulk properties

Table V gives at 300 K the average densities, intermolecular potential energies $\left\langle U_{pot}^{inter} \right\rangle$, volumes of the MD boxes $\langle V \rangle$, as well as the Hildebrand solubility parameters δ defined as:

$$\delta = \sqrt{\frac{\left\langle U_{pot}^{inter} \right\rangle}{< V >}} \qquad (16)$$

Table V *The copolyimide average model $<\rho>_{model}$ and experimental densities $<\rho>_{exp}$ (measured in m-cresol) are given in g cm^{-3}. $<V>$ are in Å^3 and $\left\langle U_{pot}^{inter} \right\rangle$ are quoted in kJ mol^{-1} molecule^{-1}. The δ parameter is in (J cm^{-3})$^{1/2}$. For error bars, see original reference.*[17]

Properties	**ODPA-ODA**	**(ODPA/BCDA)-ODA**	**BCDA-ODA**	**(ODPA/BCDA)-CF_3ODA**	**(ODPA/BCDA)-MeOODA**
$<\rho>_{model}$	1.377	1.349	1.297	1.417	1.373
$<\rho>_{exp}$	1.368	1.361	1.326	1.423	not available
$<V>$	70750	70350	65600	76800	73600
$\left\langle U_{pot}^{inter} \right\rangle$	-6367	-5927	-4719	-5683	-6278
δ	21.17	20.48	18.93	19.20	20.61

The average model densities $<\rho>_{model}$ are all found to be close to the corresponding experimental densities $<\rho>_{exp}$. Indeed, the difference between simulated and experimental values is only 0.7% for ODPA-ODA, 0.9% for the unsubstituted copolyimide, 2.2% for BCDA-ODA and 0.4% for the fluorinated copolyimide. The discrepancy seems to increase with the BCDA content, which might be related to the exclusive choice of the boat-boat isomer for that fragment, whereas higher-energy non-interconvertible boat-chair and chair-chair isomers may also exist in the real systems. However the $<\rho>_{model}$ all fall well within the 5% limit from $<\rho>_{exp}$ considered by some authors in the literature as being "acceptable" for polyimides,[213] and even within the 2% limit quoted by other authors.[91] As far as the methoxy-substituted copolyimide is concerned, $<\rho>_{exp}$ is not available but $<\rho>_{model}$ also falls within the expected range for polyimides.

As seen experimentally,[108] the density decreases with increased BCDA content, which can be related to the steric hindrance brought about by this bulky motive. Consistent with the

densities, $< U_{pot}^{inter} >$ tend to increase and δ parameters to decrease with BCDA, thus indicating that the systems are less tightly packed. The addition of a CF_3 substituent on the diamine leads to the highest-density system, which is also in agreement with experiment.[108] However, Table V shows that the fluorinated model has at the same time the largest molar volume due to to a decrease in packing energy and δ with respect to the unsubstituted copolyimide. On the other hand, the volume expansion following the addition of a methoxy group is much smaller, and its main effect on the intermolecular energy is an increase in cohesion. The added interactions with the MeO group thus outweigh the change in volume and have an opposite effect on the energy to that of CF_3. It should be noted that the Hildebrand parameters of Table V all lie within the empirical range of δ = 14 to 28 $(J\ cm^{-3})^{1/2}$, reported for polymers[193] and are in agreement with empirical estimations through the group contribution approaches.[17,193]

5.1.2. Structural properties

The indiscriminate intermolecular radial distribution functions for the chains, $g_{inter}(r)$, displayed in Fig. 27a, confirm the aforementionned trends. The average nearest-neighbour intermolecular distance, $r_{0.5}$, increase in the order ODPA-ODA < unsubstituted ≈ methoxy-substituted copolyimide < fluorine-substituted copolyimide < BCDA-ODA. Results are consistent with the evolution of the experimental *d*-spacings obtained using wide-angle X-ray diffraction.[108] Specific ODPA···ODA intermolecular interactions are particularly relevant with regard to charge-transfer complexes (CTC),[214] which are known to occur in some polyimides and have been linked to high color indices.[215-220] These CTC form by electron transfer between electron-rich diamine and electron-deficient dianhydride rings and have been characterized by UV spectroscopy,[215] solid-state ^{13}C-NMR,[217] ^{15}C-NMR,[218] and fluorescence spectroscopy.[219,220] Although classical MD simulations do not allow for electron transfer, it is obvious that direct orbital interactions are only possible if both moieties come into close contact.[218] On the whole, ODPA···ODA intermolecular interactions appear less predominant when the diamine is substituted. Shorter distances and maximum overlaps are found in the systems which stack easier, *i.e.* the homopolyimide and the unsubstituted copolyimide, in agreement with their

high colour indices characterized by UV spectrophotometry.[110] BCDA···ODA intermolecular interactions are almost totally dominated by the dissymmetric space-filling of the BCDA dianhydride, which prevents easy stacking in the first place. On the other hand, diamine-diamine intermolecular ODA···ODA interactions are very dependent on the substituent. The $n_{ODA...ODA}(r)$ curves (Fig. 27b), which give the average number of ODA aromatic carbons around a similar atom in another molecule, show that the polar trifluoromethyl group leads to significant repulsions between the ODA rings and pushes the chains apart. The smaller and less repulsive methoxy substituent has a much more limited effect:

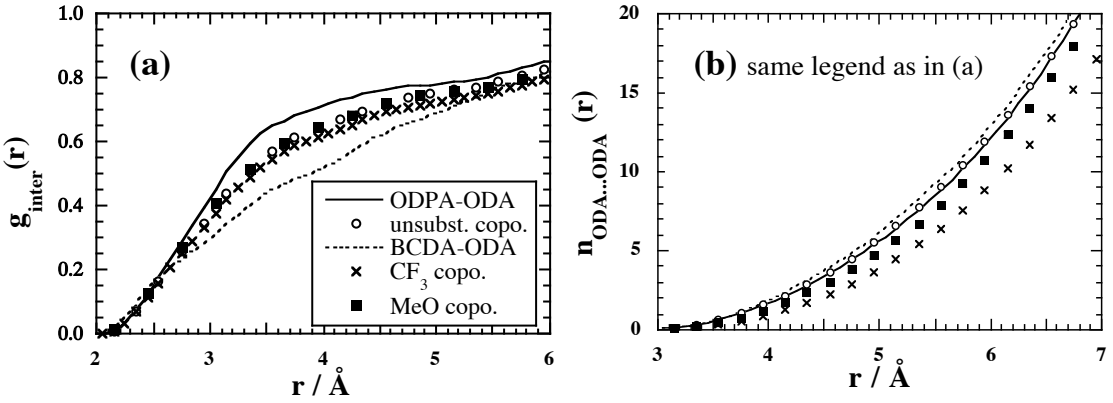

Fig. 27 *(a) Indiscriminate intermolecular radial distributions averaged over all atom pairs for each polyimide (unsubst. = (ODPA/BCDA)-ODA copolyimide, CF_3 copo. and MeO copo. = fluorine and methoxy-substituted copolyimides). (b) The intermolecular n(r) curves for ODA···ODA aromatic carbons.*[17]

As far as the conformational degrees of freedom are concerned, the flexible C-C-O-C angles and more rigid C-N-C-C distributions were found to be very similar in the five simulations, which suggests that these pivot angles are only governed by very local common intramolecular factors, *i.e.* the dianhydride imides and the aromatic rings. On the other hand, the C-C-C-F distributions in (ODPA/BCDA)-CF_3ODA were relatively flat, characteristic of very freely rotating symmetric groups. The distributions for the C-C-O-CH_3 dihedral angles were more structured, but in general, these pendant dihedrals have little influence on the global polyimide conformations.

5.1.3. Morphology of the void spaces

In order to complement the other analyses, the amount of "void space" and the manner in which it is distributed were characterized. There have been many attempts to estimate the morphology of void space using for example empirical calculations,[193,221] positron annihilation experiments,[222-224] labelling and probes,[225] or atomistic simulations.[81,95,224,226-230] Here, we used a simple method based on the "phantom sphere approach",[81,227-229] where the accessible space is obtained by a Monte Carlo procedure in which the polymer atoms are represented by hard spheres with standard van der Waals radii.[193,221] Probes of a preset radius are randomly and independently inserted over several million trials into the MD configurations previously stored, and only those probes which do not overlap with the polyimide hard spheres are accepted. The percentage of probe-accessible volume (%PAV) is then simply the percentage of accepted insertions, and the probe-accessible volume itself (PAV) is its product with the volume of the simulation box. In order to further characterize the PAV distribution, the positions of all accepted probes are stored and distances between them are subjected to an interaction limit R_p which links those probes having been inserted into the "same hole" for a given configuration. However, it is obvious that the resulting distributions will depend very much on the choice of R_p, and a compromise has to be found in order to obtain distributions with a range of hole sizes that can be used to compare the different systems in a relative way. It should also be stressed that other more sophisticated techniques have been proposed in order to exploit information from MD simulations so as to compare, for example, with positron annihilation lifetime spectroscopy (PALS).[81,224,229] However, we did not have exploitable PALS results on our copolyimides, and thus only a global comparison of the void-space morphologies was attempted.

The %PAV were obtained for probe radii ranging from 0 to 1.3 Å.[17] The smallest probe sizes led to high values, with the zero radius probe representing the total unoccupied volume (up to 37.25% for BCDA-ODA). However, results are more meaningful for probe sizes sampling accessible volume, and the %PAV for a positronium-like 1.1 Å probe is

displayed in Fig. 28a. Fig. 28b shows the underlying distributions of "holes" accessible to the 1.1 Å probe using R_p = 0.65 Å:

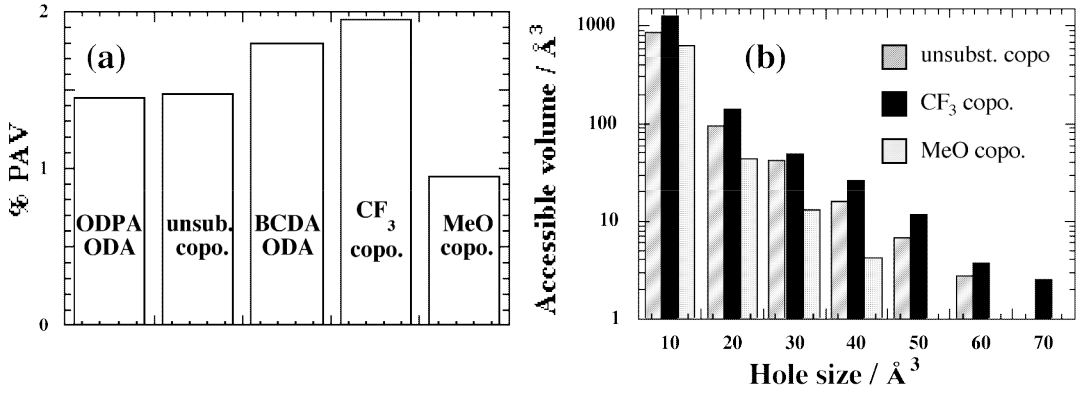

Fig. 28 *(a) Average %PAV for a probe of radius 1.1 Å. (b) Distributions of PAV for the 1.1 Å probe with an interaction parameter of R_p = 0.65 Å as a function of the hole size.*[17,20]

As suggested by the experimental free-volume fractions (FFV) estimated using the Bondi approach,[193,221] the %PAV increases with the introduction of BCDA, with a larger amount of small to medium holes brought about by its asymmetric geometry.[17] However, the system exhibiting the highest %PAV is actually the CF_3-substituted copolyimide which is found to significantly increase all sizes of voids. This is consistent with the literature on fluorine substituents, where both the steric and electronic effects are considered quite efficient in keeping the polymer chains apart.[231-234] The lowest %PAV is found in the MeO-substituted copolyimide with a tendency for the methoxy groups to occupy a part of the void space which already exists in the unsubstituted systems.

It is obvious from the various analyses of the pure models that the BCDA moiety and the CF_3 substituent on the diamine have a similar qualitative effect. Indeed, they both result in increased available void space and decreased chain cohesion. The BCDA-ODA and the (ODPA/BCDA)-CF_3ODA systems are thus potentially the most promising systems with respect to small molecules diffusion, while keeping in mind that the latter (Tg ~ 535 K) is more easily processable than the former (Tg ~ 660 K).[109]

5.2. Gas transport in polyimide bulk models

The force-field parameters for the gas molecules were directly taken from well-known sources, *i.e.* the Fisher and Lago force-field for oxygen[211] and the Cheung and Powles force-field for nitrogen.[212] Both these parameter sets were validated by checking that they maintained the experimental liquid densities at the boiling points (the differences being < 1%).[108] Helium parameters were taken from Lee et al.[235] The gas insertion procedure consisted in preparing a box of "gas" of the same size as the corresponding polyimide model at a density of ~1 g cm^{-3}. Both boxes are then superimposed and the required number of gas atoms (see later) are added by selecting those which overlap least with the polymer atoms. In this way, high overlap energies which could result from random insertions are avoided, and the initial gas-polymer repulsions are reduced as much as possible. For mobile penetrants, this method should be equivalent to a completely random insertion.

5.2.1. Individual trajectories

The mechanisms of gas motion in our bulk models[20] are similar to those reported by other authors for polyimides.[90-93] The individual displacements are obtained by a combination of oscillations within available free volumes and jumping events. These patterns have been shown to be characteristic of a diffusion which proceeds by hopping between different voids, made possible by the temporary opening of channels within the polymer matrix.[89,236,237] Although the glassy polyimide chains are fairly rigid, they do undergo natural fluctuations on the scale of very few Å, which allow them to form a passage for the gas molecules. Different types of behaviours can be seen under the timescale accessible to MD simulations (Fig. 29). The jump mechanism between adjacent cavities is best seen in Figs. 29a and 29b, with the permeant oscillating in a given cavity in between jumps. Fig. 29a displays helium diffusion, which resembles closely what is seen in the rubbery state,[89,238-240] with large jumps and quite effective diffusivity because of its high intrinsic mobility. Even if the individual molecules can oscillate within the same site for typically several hundred picoseconds and occasionally get temporarily "trapped" in a dead-end, they always reach a position which allows them to take another path. A similar type of behaviour has been found for hydrogen in polyimides.[90-93]

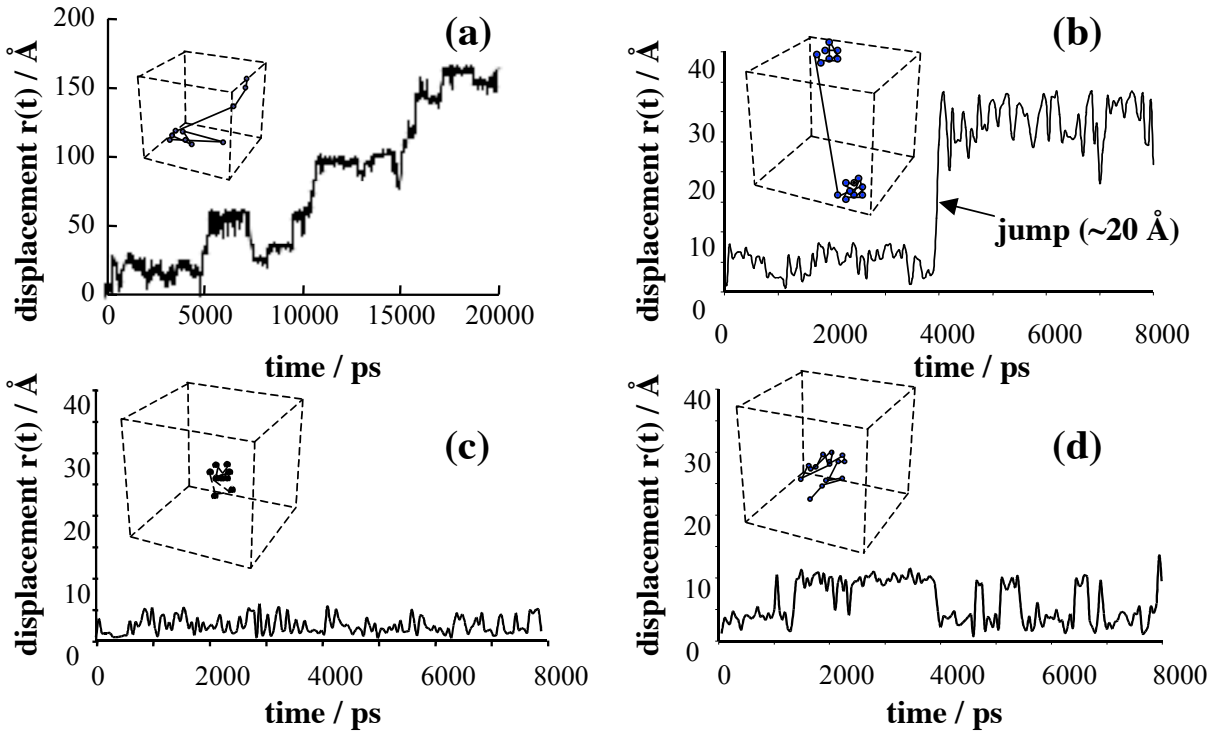

Fig. 29 *Typical gas trajectories within the copolyimide matrices as a function of simulation time. Note that the cubes only represent portions of the MD boxes.*[20,21]

On the other hand, slower penetrants such as O_2 or N_2 will have a tendency to undergo much shorter jumps (Fig. 29b), some will remain and oscillate within the same polymer cavity (with an amplitude usually < 5 Å) throughout the whole MD simulation (Fig. 29c), and others will even jump back and forth between different voids (Fig. 29d), which effectively results in slowing down diffusion. While the trajectories are rather "sharp" for O_2 and N_2 molecules (Figs. 29b, 29c, 29d), the jumps are much less pronounced and the positional fluctuations at a given site are larger for He, thus leading to a certain “blur” in its trajectories (Fig. 29a).[89,236]

5.2.2. Solubility in the bulk

The solubility, S, is linked to the excess free energy, ΔG, of a gas molecule dissolved in the polymer, the Boltzmann constant k_B and the temperature T:[89]

$$S = exp\left(-\frac{\Delta G}{k_B T}\right) \tag{17}$$

Solubility is actually a dimensionless ratio between the "volume of gas", V_g, absorbed into a given volume of polymer, V_p, *i.e.* $S = V_g/V_p$. To be more precise, V_g is the volume the same number of gas molecules (as absorbed into V_p) would occupy if they were in the gas phase at the same conditions of temperature and pressure.

It is well-known that diffusion and sorption in glassy polymers is traditionally described by the « dual-mode sorption model », in which there are two distinct sorption modes: unspecific dissolution, which follows Henry's law, *i.e.* the solubility of dissolved gas is linearly proportional to the pressure P, and trapped molecules in pre-existing cavities, which are described by a Langmuir term.[241,242] However, for small penetrants, sorption follows well Henry's law, $S=S_cP$, where the "constant" of proportionality, S_c, is called the solubility coefficient. For He and even for O_2 and N_2, it has become commonplace to report Henry solubility coefficients in the literature, irrespective of whether Henry's Law is obeyed or not.[95] The free energy for the solvation process is thus usually estimated in atomistic simulations using Widom's test-particle insertion method, in which a gas molecule is inserted at random sites into the matrix and the change in potential energy ΔU associated with the insertion is calculated.[89,243] This process is repeated many times in order to obtain ensemble averages. S is then directly linked to the probability of insertion for the gas molecules into the polymer, p_{ip}:

$$S \approx p_{ip} = \left\langle exp\left(- \frac{\Delta U}{k_B T} \right) \right\rangle \qquad (18)$$

p_{ip} is also related to the excess chemical potential of the gas in the polymer, μ_{ex} by:

$$\mu_{ex} = - RT\ ln\left\langle exp\left(- \frac{\Delta U}{k_B T} \right) \right\rangle = - RT\ ln(p_{ip}) \qquad (19)$$

In order to be consistent with the experimental set-up, the number of gas probes absorbed into the polymer model at T should be dependent on the external pressure P and on p_{ip}. If one considers an actual membrane constituted of a polymer of volume V_p with some free space for the gas phase on either side amounting to a total volume V_f, the probability of insertion for an ideal gas will be 1 in the gas phase and p_{ip} in the polymer, assuming spatial

invariance within the membrane itself. For N insertions, the total number of gas probes in the gas phase, n_f, will thus be :

$$n_f = \frac{N\ V_f}{V_f + p_{ip}V_p} \tag{20}$$

Assuming the ideal gas conditions, n_f is directly linked to the external pressure by $P\ V_f = n_f\ k_B\ T$, and can thus be replaced by its expression in Eq. 20:

$$P \approx \frac{N\ k_B\ T}{V_f + p_{ip}V_p} \tag{21}$$

In a similar manner, the total number of gas probes inserted into the polymer, n_p, can be obtained by:

$$n_p = \frac{N\ p_{ip}\ V_p}{V_f + p_{ip}V_p} \tag{22}$$

From the common denominator in Eqs. 21 and 22, it follows that :

$$n_p \approx \frac{P\ p_{ip}\ V_p}{k_B\ T} \tag{23}$$

If one were to respect the experimental solubility and conditions, *i.e.* an externally-imposed pressure of 3 bars at room temperature,[108,112] this would amount to less than one gas probe being inserted into the ~6500-atom bulk matrices. In order to both improve the statistics for the diffusion of the penetrants and remain consistent with respect to the gas solubilities, we usually set the number of gas probes to be inserted into the polyimide matrix, n_p, and adjust the external pressure P accordingly.[21] For example, a reasonable comprise can be found with 25 heliums in the standard ODPA-ODA 6225-atom model, which correspond to an external pressure of ~200 bars. We note that, in a periodic system, we are free to set gas concentration and pressure independently whereas, in any real experiment at a particular temperature, the concentration and applied pressure are inextricably linked.

Solubility coefficients are most often quoted as $S_c = p_{ip}T_{STP}/(T\ P_{STP})$, where T_{STP} and P_{STP} are the standard temperature and pressure (*STP: 273.15 K;1.013 10^5 Pa*) and T is the temperature of the measurement. This means that the quantity S_cPV_p represents the volume of

gas absorbed in the polymer of volume V_p at the pressure P and temperature T after it has been brought back to *STP* conditions and assuming it behaves as an ideal gas. Taking the same example as above, S_c for helium in the ODPA-ODA model is ~0.06 cm^3(STP) cm^{-3} bar^{-1},[21] and is close to its experimentally-estimated value S_{exp} of 0.04 cm^3(STP) cm^{-3} bar^{-1}.[108] However the S_c parameters for oxygen and nitrogen in the same matrix are ~2.1 cm^3(STP) cm^{-3} bar^{-1} and ~1.5 cm^3(STP) cm^{-3} bar^{-1} respectively, *i.e.* they are larger than the experimental-reported S_{exp} of ~0.27 and ~0.17 cm^3(STP) cm^{-3} bar^{-1} by a factor 5-10.[108] The latter were obtained using the relationship between S_{exp}, the experimentally measured effective permeability P_{exp} and the diffusion coefficient D_{exp} for ODPA-ODA:[108,112]

$$S_{exp} = \frac{P_{exp}}{D_{exp}} \tag{24}$$

Other literature sources for polyimides[94,95,207,244-248] give S_{exp} at room temperature in the range from 0.8-1.5 cm^3(STP) cm^{-3} bar^{-1} for O_2 and from 0.5-0.8 cm^3(STP) cm^{-3} bar^{-1} for N_2. These values suggest that the combined force-fields[17,211,212] for polyimides+O_2 and polyimides+N_2 overestimate the solubility by at least a factor 1.5. However, it is worth noting that a same order of magnitude has been reported for model solubilities of O_2 and N_2 in other polyimides and this has been considered as "being in very good agreement" (with respect to the poor agreement found for other penetrants such as CH_4 and CO_2).[94,95] On the other hand, the reported S_{exp} are surprinsingly small, thus casting a doubt on the reliability of the associated experimental measurements. It is highly possible that the differences between S_c and S_{exp} stem from both model and experimental origins. As expected,[207,249] the solubility for He in polyimides is much lower than that for other gases, but the values found fall in the experimental range. Indeed, the solubility for He has been reported as being 0.053 and 0.062 cm^3(STP) cm^{-3} bar^{-1} for PMDA-ODA and PMDA-IPDA.[231,232]

In all cases, the solubility coefficients are only weakly dependent on the chemical structure of the macromolecules. The long-held view that permeabilities in these glassy matrices are mostly governed by diffusion[250] is thus supported both by these simulations and experimental data.[108]

5.2.3. Diffusion coefficients in the bulk

Although there are several methods available to evaluate diffusion coefficients from MD simulations,[251] the most common way involves the calculation of mean-square displacements, MSDs = $<(r_i(t+t_0)-r_i(t_0))^2>$, averaged over all penetrant molecules and all possible time origins of the production runs, t_0. The MSDs can then be used to evaluate the diffusion coefficients D_{bulk} using Einstein's equation:

$$D_{bulk} = \lim_{t\to\infty} \frac{1}{6t} < \left(r_i(t+t_0) - r_i(t_0) \right)^2 > \qquad (25)$$

However, the derivation of the Einstein equation assumes that the gas molecules follow a random walk. In dense polymers, where penetrant motion is strongly restricted by the immediate environment, Einstein's equation is only really valid within the framework of a long-time Fickian diffusive limit, *i.e.* when the MSDs are proportional to t. In the intervening time, with the exception of a short-time ballistic regime at the very start, the MSD curves are usually found to be proportional to t^n with $n < 1$, which characterizes the anomalous diffusion regime.[89,236,252] The turnover or crossover time defines that region when diffusion goes from being anomalous to Fickian, and is best identified on log-log plots,[89,236] when the slope between log(MSD) and log(t) tends to one. Fig. 30a shows such a log-log plot for the average MSD obtained from 8 simulations of helium diffusion in 4150-atom ODPA-ODA matrices:

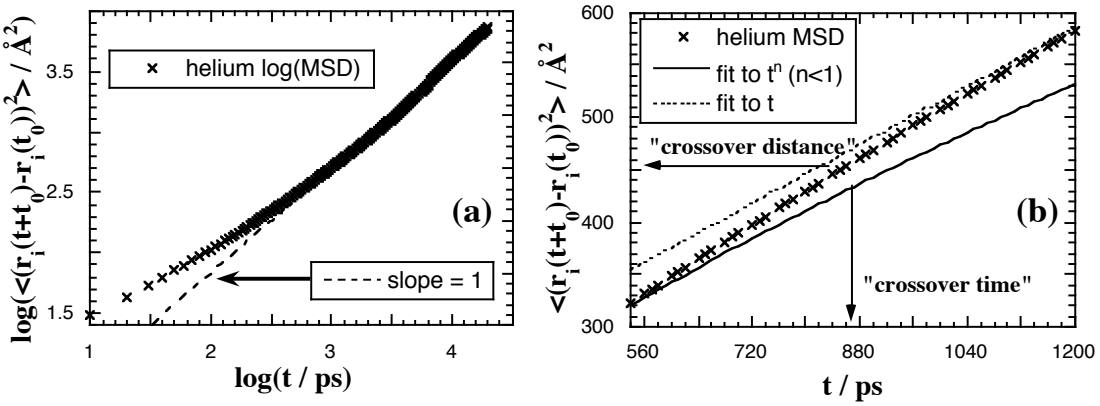

Fig. 30 *(a) A log(MSD)-log(time) plot for helium in ODPA-ODA along with a dashed line of slope 1 (b) The crossover region in the helium MSD curve along with a fit to the form $t^{0.63}$ for the anomalous regime and another fit to the form t for the Fickian regime. The crossover time and distance are defined as the average point during the gradual change of regime.*[21]

Fig. 30b concentrates on the crossover between the anomalous and the Einstein regimes for the same system.[21] It is clear that the crossover region is around 1000 ps, a slope of 1.0±0.1 in the log(MSD) *vs* log(t) being usually considered as characteristic of Fickian diffusion.[251,253] The problem of actually defining a specific crossover "time" and "distance" is illustrated in Fig. 30b. The transition between both regimes is very gradual, and it is not particularly obvious to identify. However, it is possible to fit the anomalous regime to MSDs $\propto t^n$ with $n < 1$ and the Fickian regime to MSDs $\propto t$, and then define the crossover time and distances as the average point during the gradual change of regime.

A second way to evaluate the diffusion coefficient is through the probability density distributions of penetrant displacement vector components, $\rho(\alpha(t+t_0)-\alpha(t_0))$, where t is the time interval, t_0 is the time-origin, and α represents x, y or z.[18,21] To have better statistics for the $\rho(\alpha(t+t_0)-\alpha(t_0))$, the absolute values of the displacements along the x, y and z axes are averaged together for all penetrant atoms and over all possible time origins. Fig. 31 shows[18,21,108] that these distributions in the anomalous regime, *i.e.* at short time-intervals, cannot be fitted by the single gaussian curve expected from Fickian diffusion:

$$\rho\left(\alpha\left(t + t_0\right) - \alpha\left(t_0\right)\right) = \sqrt{\frac{3}{2\,\pi\left\langle r^2\right\rangle}}\; exp\left(\frac{-3}{2\left\langle r^2\right\rangle}\alpha^2\right) \tag{26}$$

with $\langle r^2\rangle = \langle x^2\rangle + \langle y^2\rangle + \langle z^2\rangle$. However, the anomalous regime distributions do fit surprisingly well to a weighted combination of two gaussian curves,

$$\rho\left(\alpha\left(t + t_0\right) - \alpha\left(t_0\right)\right) = \omega(t)\left(\sqrt{\frac{3}{2\,\pi\left\langle r_1^2\right\rangle}}\; exp\left(\frac{-3}{2\left\langle r_1^2\right\rangle}\alpha^2\right)\right) + (1-\omega(t))\left(\sqrt{\frac{3}{2\,\pi\left\langle r_2^2\right\rangle}}\; exp\left(\frac{-3}{2\left\langle r_2^2\right\rangle}\alpha^2\right)\right) \tag{27}$$

thus suggesting that there are in fact two distinct types of time-dependent behaviour for the components. A simple interpretation is that the first one, referred to in Fig. 31a as type "1" with average displacement $\langle r_1^2\rangle$ is mostly related to those molecules which remain in, or return to, the very near vicinity of their position at the time-origin, *i.e.* molecules which can be considered as being “trapped”. The second one, referred to in Fig. 31a as type "2" with

average displacement $<r_2^2>$, could primarily be due to those molecules which escape from their initial environments, *i.e.* which will eventually contribute to the limiting long-time diffusion coefficient. The weighting factor, $\omega(t)$, represents the respective proportions of both types of populations for a given time-interval t. Although these distributions are for components (and not the modulus) of the vector displacement, this simple interpretation does agree very well with visual analyses of the individual trajectories (Fig. 31a):

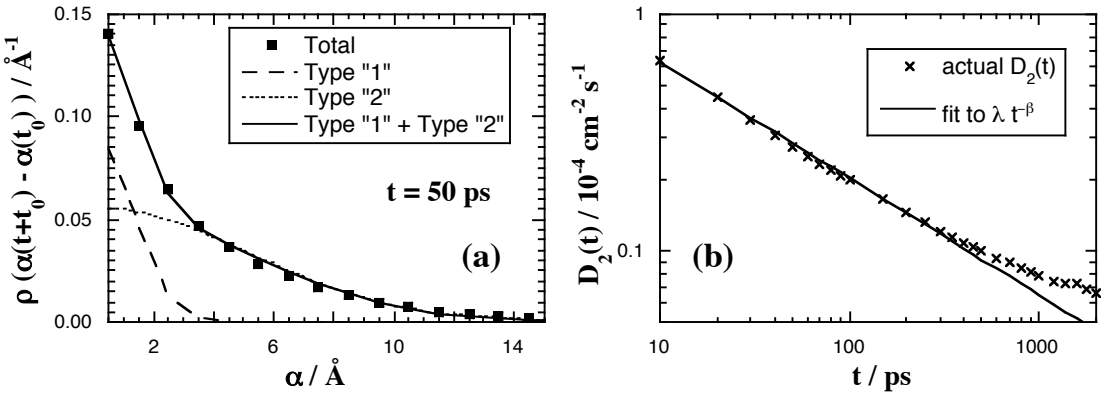

Fig. 31 *(a) Probability density distribution for the components of the displacement vector for helium in an 56025-atom ODPA-ODA matrix at t = 50 ps (black squares). The dashed lines represent the two weighted gaussians fitted to the actual data (Eq. 27). The plain line is the sum of both gaussians (b) Time evolution of $D_2(t)$ as defined in Eq. 28 (crosses). The line is a fit to the algebraic form $D_2(t) = \lambda t^{-\beta}$.*[21]

For the smallest time-interval considered, *i.e.* 10 ps, ω is ~0.35. It decreases rapidly as the time-interval increases and drops to 0.10 after ~1000 ps. This confirms the crossover region from the anomalous to the Fickian regime, whereafter the displacement vector component distributions can then be fitted satisfactorily to the single Gaussian expression of Eq. 26 with the diffusion coefficient D_{bulk} being obtained from $<r^2>/6t$.

An advantage of this method is that it characterizes diffusion at both short and long distances. In the anomalous regime, $<r_1^2>$ and $<r_2^2>$ contribute to the displacement of the molecules, whereas the increasing $<r_2^2>$ with larger t allow for the definition of "time-dependent" diffusion coefficients, $D_2(t)$:[18,21,108]

$$D_2(t) = \frac{\left\langle r_2^2 \right\rangle}{6\,t} \tag{28}$$

The $D_2(t)$ coefficients are displayed on a logarithmic scale for different t in Fig. 31b. They decrease in the anomalous regime and can be fitted to the algebraic form $D_2(t) = \lambda t^{-\beta}$. The divergence from the algebraic form is the signature of the crossover region from the anomalous to the Fickian regime, and the limiting $D_2(t)$ becomes equivalent to D_{bulk}.[21]

A third way to evaluate D_{bulk} is through the self part of the van Hove correlation function.[251,253] The van Hove self-correlation function $G_s(r,t)$ gives the probability density that a penetrant moves a distance r over a given time interval t. Its limiting form in the Einstein regime is defined as:[254]

$$G_s(r,t) = (4\pi D_{bulk}\, t)^{-3/2} \exp\left(\frac{-r^2}{4D_{bulk}\, t}\right) \tag{29a}$$

or alternatively, if the diffusion coefficient D is replaced by $<r^2>/6t$, by:

$$G_s(r,t) = \left(\frac{2\pi\left\langle r^2\right\rangle}{3}\right)^{-3/2} exp\left(\frac{-3r^2}{2\left\langle r^2\right\rangle}\right) \tag{29b}$$

As can be expected, the fits of the actual $G_s(r,t)$ to Eq. 29 in the anomalous regime, *i.e.* up to 1000 ps, are poor. On the other hand, the data at longer times become consistent with the limiting form expected, and the fits can be used to evaluate D_{bulk} from either Eq. 29a or Eq. 29b (Fig. 32a):

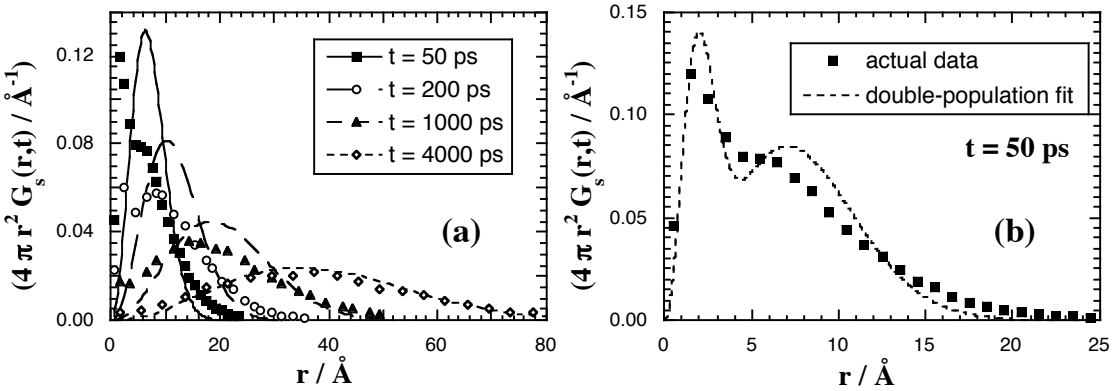

Fig. 32 *(a) Van Hove self-correlation functions for He in a 56025-atom ODPA-ODA matrix at different time-intervals. The actual data are shown in symbols only. The associated lines are the corresponding fits to the limiting form given in Eq. 29. (b) A close-up of the correlation function for t = 50 ps. The actual data points are the squares. The dashed line is a tentative fit to the weighted form of Eq. 30.*[21]

It is interesting to note that the van Hove functions in the anomalous regime exhibit a shoulder or even a double peak form. This appears to be consistent with the notion of two populations identified in the penetrant displacement component distributions. In a similar vein to Eq. 27, a fit of the data to the following weighted two-population form was attempted:

$$G_s(r,t) = \omega(t)\left(\left(\frac{2\pi\left\langle r_1^2\right\rangle}{3}\right)^{-3/2} exp\left(\frac{-3r^2}{2\left\langle r_1^2\right\rangle}\right)\right) + (1-\omega(t))\left(\left(\frac{2\pi\left\langle r_2^2\right\rangle}{3}\right)^{-3/2} exp\left(\frac{-3r^2}{2\left\langle r_2^2\right\rangle}\right)\right) \qquad (30)$$

with $<r_1^2>$ and $<r_2^2>$ again being the average displacements for type "1" and "2" at a time interval *t*. From Fig. 32b it is clear that the fit to Eq. 30 is much less successful at describing the data for $G_s(r,t)$ than Eq. 27 is of matching the displacement vector component distributions. Adding further terms gives progressively better fits, but they are difficult to link to a physical basis. It thus suggests that the double-population explanation for the displacement components, albeit globally representative of the reality, is a bit simplistic. Indeed, one could argue that an atom could move along only one direction, e.g. *z*, while remaining close to its initial position in the *x*-*y* plane. In that case, the *x* and *y* components would contribute to the population of "type 1" and the *z* component to the population of "type 2". Indeed a numerical integration of the vector displacement magnitude distributions, $\rho(\boldsymbol{r})$ (= $4\pi r^2\ G_s(r,t)$), assuming that the probability of a given displacement vector, $\rho(\boldsymbol{r})$, is simply proportional to $\rho(x)\rho(y)\rho(z)$ fail to predict the actual form of the $4\pi r^2$-weighted van Hove. In other words, the components of the displacement vector cannot be considered as being independent in the anomalous diffusion regime. The polymer matrix imposes a correlation in the motion of the gas atoms and restricts the penetrant motion,[89] which is particularly important for short displacement vectors, *i.e.* at short times.

A fourth way to obtain D_{bulk} would be the transition state theory (TST) method,[236] which allows for far longer times to be attained than brute force MD and can thus be used to obtain reliable small molecule diffusion coefficients.[90-95] However, one of the assumptions underlying the TST method is that the polymer packing does not undergo structural relaxations and that atoms in the polymer oscillate elastically around fixed positions

determined from prior simulations of the pure matrix.[236] It is thus not surprising that TST has been reported as taking badly into account the variations of diffusive motion as a function of temperature.[248] Although there are approaches to explicitely introduce the coupling between polymer and penetrants degrees of freedom in the TST calculations,[226,237,255] such assumptions bring extra variables to the problem, and we prefer to carry out our simulations well within the Einstein regime. However, we note that TST results can also be used as the basis for a more sophisticated coarse-grained method where large microstructures of sorption states and jump paths are generated by reverse MC, and penetrant diffusion analyzed by kinetic MC.[46]

In the initial work,[108] the model diffusion coefficients for He, O_2 and N_2 in the (ODPA/BCDA)-ODA family were first obtained from the MSDs and later confirmed by the vector displacement components. Despite the careful validation of both polyimide and gas force-fields (see Sec. 5.1 and 5.2), the calculated gas D_{bulk} were found to be systematically larger than the measured ones. In the case of helium for example, this typically amounted to a factor of at least 25, which got even larger for both O_2 and N_2.[108] Qualitatively, diffusion occurred as expected faster in both the BCDA-ODA homopolyimide and the fluorinated (ODPA/BCDA)-CF_3ODA, and the model D_{oxygen} followed even the general experimental order, *i.e.* ODPA-ODA < unsubstituted copolyimide < fluorinated copolyimide < BCDA-ODA.[112] However, as has been noted before, it is not obvious that our experimental data are truly reliable: reproducibility could not be tested since the limited amount of material available prevented further gas permeation measurements from being made and only one membrane *per* system was tested. This also meant that other questions related for example to the processing history, morphology, solvent effects and many other possible factors remained unanswered. An even more suspicious sign is that gas permeabilities for O_2 and N_2 in the ODPA-ODA matrix have been reported elsewhere as being respectively 0.183 and 0.026 Barrers,[256] which differ fairly significantly from the corresponding 0.07 and 0.09 Barrers found in the course of this work.[112] This would indicate a O_2/N_2 permselectivity of 7 in the former case, while it would be closer to 1 in the latter for the same system. Indeed, the numerous difficulties encountered when comparing experimental to simulated data in the case

of polyimide membranes, whose processing conditions strongly affect the results, have been pointed out by Heuchel et al.[95] Nevertheless, our main concern was the *systematic* trend in overestimating diffusivity in our models, regardless of the thorough preparation of the pure matrices,[17] and several possible explanations for the disagreement between the models and the experiments have been put forward. This has led to a series of further simulations concerning specific features of such glassy models, which will be described in the following sections.

5.2.4. Influence of system size

A first suggestion was that the original ~6500-atom systems[17] were too small. Despite the fact that this size is fairly standard in such simulations,[94,95,224] it was possible that the small system sizes coupled with the relatively long chains and the periodic boundaries could have led to enhanced diffusion due to artificial inhomogeneities and percolating channels in the glassy models.[91] Finite-size effects are not a new preoccupation in molecular simulations,[89,240] and, especially in glassy polymers, a simulation size effect on gas diffusion has been suggested.[236,251,253,257,258] The most relevant work with respect to our systems is that of Cuthbert, Wagner et al.,[251,258] who carried out MD simulations of gas diffusion in glassy polystyrene (PS) and polypropylene (PP) with different box sizes. Several polymer chain lengths were considered (up to ~6600 atoms) at a fixed density. The initial chain configuration was generated with a gaussian lattice algorithm[66] and different sizes of penetrant gas molecules were used. Solubility was found to be system-size dependent for the larger penetrants, although gas diffusion was virtually unaffected.[251,258]

In order to assess the influence of simulation box size, we created instead several models containing different numbers of molecules of the *same* chain length for the 40-*mers* ODPA-ODA. These systems were then simulated at the same applied external conditions of constant temperature and constant pressure tensor. Eight 4150-atom, one 6225-atom and a much larger 56025-atom system were generated by hybrid PMC-MD single-chain sampling and relaxed with the polyimide full potential.[17] Their volumetric and energetic properties at 300 K are compared in Table VI and show no system-size artefact:[21]

Table VI *Average bulk properties of the pure polyimide packing models. The results for the eight 4150-atom models have been averaged and the numbers in parentheses refer to the standard deviations of the sample means. The densities* $\langle\rho\rangle_{model}$ *are given in g* cm^{-3}. $\langle V\rangle$ *are the volumes of the MD cells in* $Å^3$ *and* $\langle l\rangle = \langle V\rangle^{1/3}$ *the cell length in Å. The potential intermolecular energies* $\left\langle U_{pot}^{inter} \right\rangle$ *are quoted in kJ* mol^{-1} *molecule*$^{-1}$. *The solubility parameter,* δ, *is in* $(J\ cm^{-3})^{1/2}$. *For error bars, see original reference.*[21]

Properties	**4150-atom**	**6625-atom**	**56025-atom**
$\langle\rho\rangle_{model}$	1.367 (0.017)	1.377	1.376
$\langle V\rangle$	47520 (580)	70750	637300
$\langle l\rangle$	36.2 (0.2)	41.4	86.1
$\left\langle U_{pot}^{inter} \right\rangle$	-6098 (124)	-6367	-6134
δ	20.65 (0.32)	21.17	20.77

Helium was chosen as the main test-penetrant because of its high permeability in polyimides.[249,250,259,260] Three polymer+helium simulation boxes of different sizes are displayed for comparison on the same scale in Fig. 33.

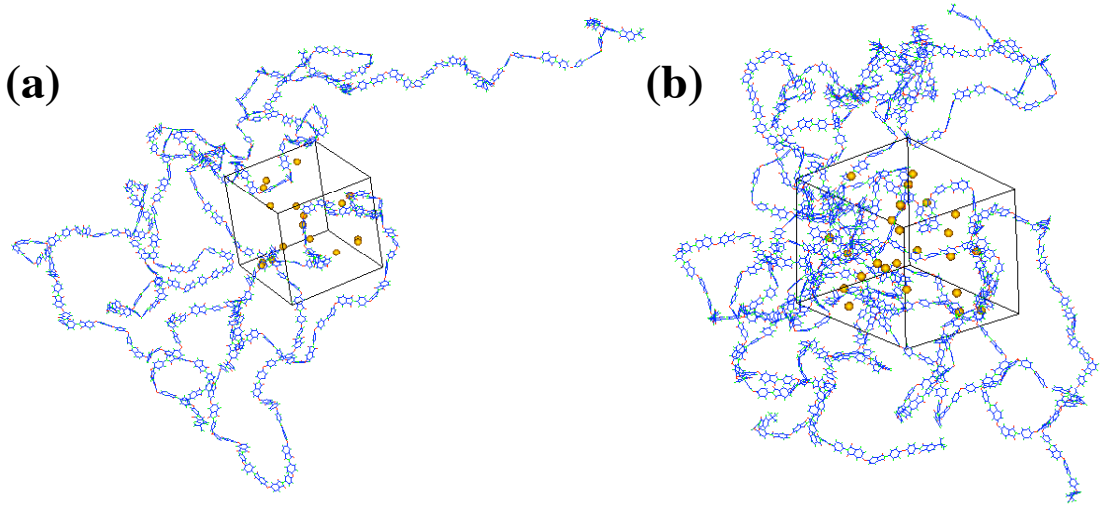

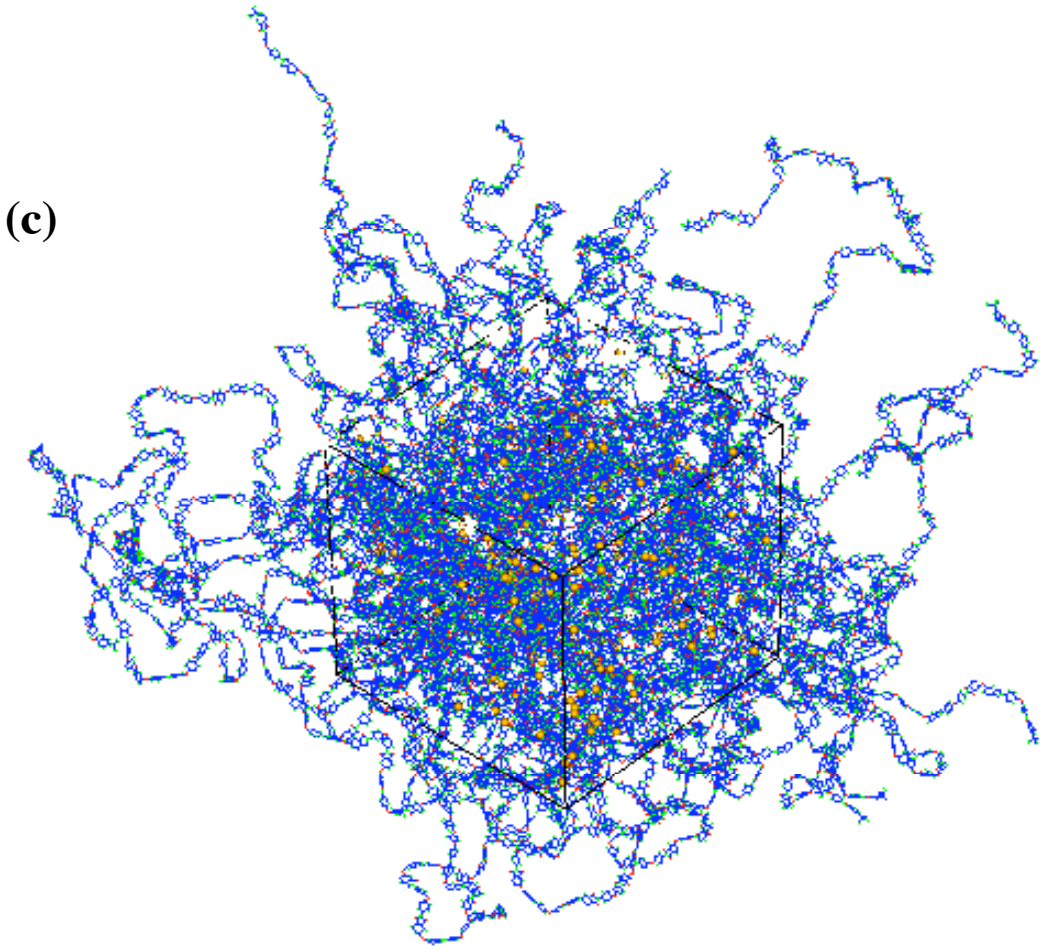

Fig. 33 *Schematic representations of (a) a 4150-atom (b) the 6625-atom and (c) the 56025-atom ODPA-ODA matrix with helium. The polyimide and gas molecules are represented in wire-frame and space-filling models, respectively.*[21]

However, Widom's insertion procedure for estimating gas solubilities (Sec. 5.2.2.) was applied not only to helium, but, as proposed by Cuthbert et al.,[251,258] also to hypothetical derivatives of helium, namely argon-helium, "Ar-He", and carbon-dioxide-helium, "CO_2-He". These particles have the same mass and ε parameter for the LJ potential than helium, but their size parameters are σ = 3.4 Å for Ar-He and 4.5 Å for CO_2-He instead of 2.6 Å for He. The resulting S_c solubility coefficients are reported in Table VII.

Table VII *Solubility coefficients S_c in $cm^3(STP)\ cm^{-3}\ bar^{-1}$ (with a maximum standard error of ± 0.001) for He, "Ar-He" and "CO_2-He" in the pure polyimide packing models at 300 K. The results for the eight 4150-atom models have been averaged and the numbers in parentheses refer to the standard deviations of the sample means.*[21]

Properties	**4150-atom**	**6625-atom**	**56025-atom**
S_c for He	0.065 (0.007)	0.064	0.059
S_c for Ar-He	0.030 (0.006)	0.029	0.025
S_c for CO_2-He	0.010 (0.005)	0.009	0.007

The average values for the solubilities are obviously number-independent, even in the case of the larger hypothetical "CO_2-He". This is in total contradiction with the results of Cuthbert et al.[251,258] who linked their system-size-dependent effect in PS to the fact that smaller structures were unable to form cavities of sufficient size to accommodate larger penetrants.[258] They even confirmed this bias in PP by examining their cavity sizes, and showing that their smallest structures had narrower sizes distributions.[251] In order to ensure that the distributions of cavities were not biased in any way in our ten different ODPA-ODA models, changes in the excess potential energy ΔU associated with the Widom-particle insertion process were sub-averaged every 1000 insertions for one million trials per configuration, using the full U_{LJ} (Eq. 5a) and U_{coul} (Eq. 6) potentials. The resulting normalized probability distributions of $\Delta U_{1000\text{-}ins}/k_BT$ are displayed for He and "CO_2-He" particles in Fig. 34. Standard deviations calculated from the eight different simulations of the 4150-atom size are indicated in order to characterize the dispersion of the results. There is indeed a large amount of heterogeneity in the void distributions, which is reflected both in the actual distributions of $\Delta U_{1000\text{-}ins}/k_BT$ and in the standard deviations displayed. This is especially clear for the large cavities corresponding to the smaller $\Delta U_{1000\text{-}ins}$. However, if one considers the normal differences that can be expected from the standard deviations of the 4150-atom size, there is no real bias in the cavity size distributions of the larger 6225-atom and 56025-atom systems.

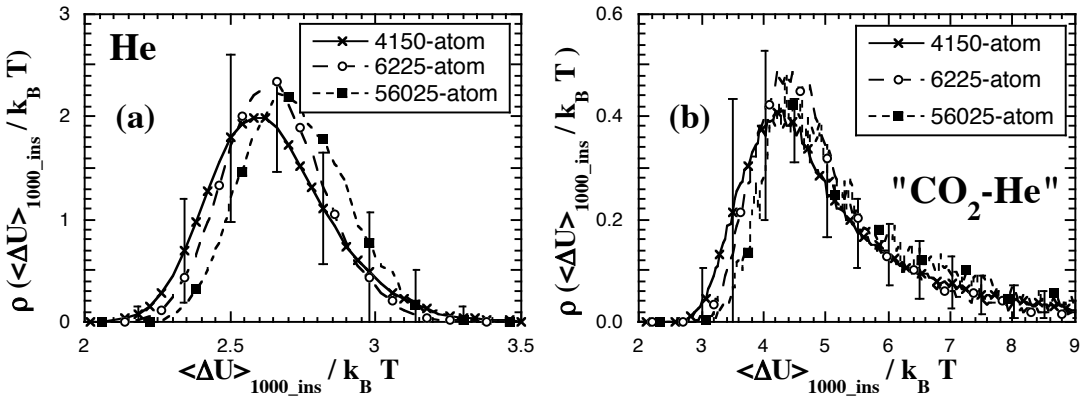

Fig. 34 *Normalized probability distributions of the sub-averaged changes in excess potential energy. The inserted particles are (a) He and (b) the hypothetical "CO_2-He" as defined in the text.*[21]

It is interesting to note that when the diameter of the inserted particles is bigger, *i.e.* He < "Ar-He" < "CO_2-He", the distributions of excess chemical potentials get progressively wider and skewed to the right, indicating that there are fewer holes of the size that can easily accommodate particles of larger sizes. On the other hand, the distributions for particles as small as He are quite symmetric in terms of large and small cavities, which suggests that this gas can potentially access most of the void-space available without too much disruption of the glassy polyimide matrix. Fig. 34 thus proves that the use of only one chain length for the ODPA-ODA polyimide as well as constant-pressure rather than constant-density conditions avoids the cavity size bias reported by Cuthbert et al.[251]

As far as diffusion is concerned, it became clear that using the full potential for the polyimide+helium models would rapidly become prohibitive in terms of computational costs, especially for the largest system. Consequently, in that phase, the U_{LJ} and U_{coul} potentials were replaced by U_{WCA} (Eq. 5c). Helium individual trajectories are qualitatively very similar to those obtained using the more realistic potentials (Fig. 29a) and the WCA form allows for longer simulation times and better statistics, the most important point being that the various systems are consistent with each other. Helium diffusion could thus be analyzed over periods of up to 20 ns using mean-square displacements, distributions of penetrant displacements components as well as van Hove correlation functions. Fig. 35 displays the compared (a)

MSDs *vs* time curves and (b) time evolutions of the helium diffusion coefficient for type "2" population as defined in Eq. 28 as a function of box size:[21]

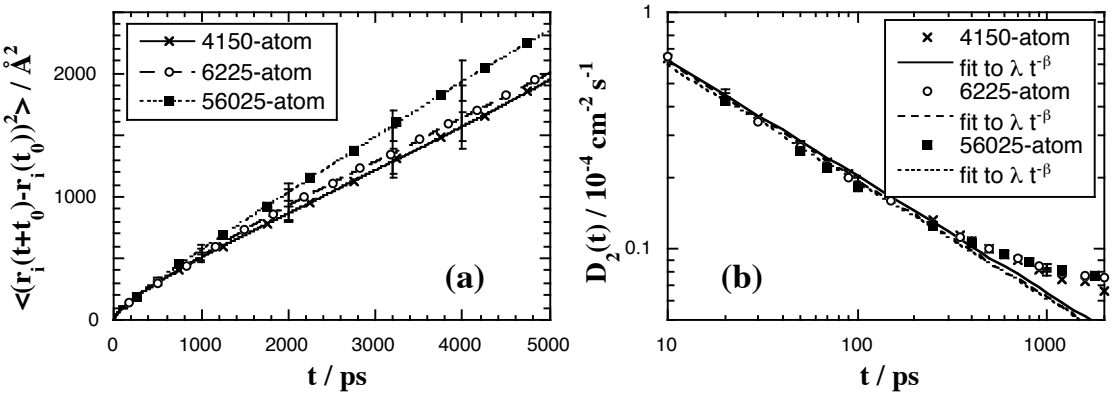

Fig. 35 *(a) Helium MSDs vs time as a function of system size. The error bars are the 99% confidence interval associated to the standard errors calculated from the number of gas molecules, the number of uncorrelated time origins in a given system and the number of systems per size. (b) the $D_2(t)$ coefficients displayed on a logarithmic scale for all three sizes, along with fits to the algebraic form $D_2(t) = \lambda t^{-\beta}$. The error bars are indicated for t = 20, 50, 100, 500 and 1000 ps.*[21]

Figs. 35a and 35b show that no number dependence could be detected in the diffusion either, whether the gas molecules were in the anomalous or in the Fickian regime. The transition region from anomalous to Einstein diffusion is around 1000 ps. Within the obvious uncertainties linked to the graphical determination (see Fig. 30a), the associated crossover "distances" could be evaluated at ~22 Å for the three sizes under study. They thus occur at smaller values than the box length which is once again in disagreement with the results of Cuthbert et al. for helium in glassy PP.[251] However, the same authors reported that their "Ar-He" and "CO_2-He" penetrants did reach the diffusive regime before traveling a box length in their simulations,[251] thus suggesting that the difference might more be due to the various potentials used rather than to the box-length effect. It is worth mentioning that a critical box size, above which the diffusion coefficient and the turnover point become independent of box size, has indeed been reported in frozen polymer matrices.[253,257] However, in those cases, the penetrant diffusion mechanism changes from an activated process to a kinetic motion

hindered by tortuosity.[253] Our polyimide chains are mobile, albeit in a fairly limited way, and we do not see such a critical limit.

The actual D_{bulk} obtained from the MSDs curves (Eq. 25) were $D_{4150\text{-}atom} = 6.0\times10^{-6}$ cm^2 s^{-1}, $D_{6225\text{-}atom} = 6.7\times10^{-6}$ cm^2 s^{-1} and $D_{56025\text{-}atom} = 7.5\times10^{-6}$ cm^2 s^{-1}. The same values were found from Eqs. 28 and 29. The error bars on the MSDs can also be used to give limiting values, with an overall lower bound of $D_{bulk} = 4.8\times10^{-6}$ cm^2 s^{-1} and an upper bound of $D_{bulk} = 8.2\times10^{-6}$ cm^2 s^{-1}, which differ by a factor of 1.7. Despite using U_{WCA}, the order of magnitude of the diffusion coefficients found here is reasonable for helium in glassy polyimides, which usually are in the range ~1-8×10^{-6} cm^2 s^{-1}.[231,232] However, reasons others than number-dependence will have to be sought to explain the discrepancies between simulated and experimental diffusion coefficients that initiated this work.

5.3. Gas transport in polyimide membrane models

The direct correlations between the basic chemical structures and the permeabilities of polyimide membranes have naturally been widely studied experimentally.[29,207,208,231,232,249,261] However, membrane pre- post- and processing parameters[96,110] are also known to be of paramount importance: molecular weight,[97] residual solvent,[98] heating cycle,[99,100] etc… have all been named as potentially influencing the physical properties of the polyimides.[96] Another key factor is film thickness. Diffusivity and solubility of oxygen transport through dry Kapton® membranes have been reported to increase along with the thickness of the samples.[262] In an intriguing work, it has been postulated instead that solubility and cohesion energy density increase in thinner glassy films.[263] Pin-holes or defects in the thin layers are known to affect selectivity,[263] while defect-free layers are thought to provide greater size and shape discrimination, a property used in the design of asymmetric polyimide membranes.[264,265] It has even been suggested that free volume could diffuse to a thin film surface[266,267] in order to explain thickness-related physical ageing of polyimide films.[268,269] In addition, membranes which are cast on glass are known to result in stiffer, stronger and more oriented films than when they are cast on mercury.[96] There are thus many possibilities for skin effects in these

materials.[270] From a molecular point-of-view, it is clear that a surface region of the membrane where the chains are either more or less ordered could significantly affect penetrant solubility and diffusion and maybe even act as the most important factor in the process of permeation.

As described in Sec. 3.2, we created a huge 141100-atom fully-atomistic model of an actual 40-*mers* ODPA-ODA membrane.[24] It was periodic in the *x*- and *y*-directions, and was initially confined between two solid walls in the *z*-direction in order to be consistent with the presence of a glass casting surface. This first "confined membrane" allowed us to test the influence of a high-density interface using the U_{WCA} potential to reach the steady-state for diffusion over a production run of 10 ns.[24] In a second stage, the more realistic U_{LJ} and U_{coul} interactions were included in order to maintain the cohesion of the membrane upon removal of the walls and let the density at the interface and the interior adjust itself naturally. Such a model is likely to be more representative of reality where the film is peeled off the glass plate and local rearrangement, particularly at the surface, can occur. However, despite the implementation of a parallelized particle-mesh technique using an iterative solution of the Poisson equation for the efficient evaluation of the electrostatic interactions,[24] only 1 ns of production run could be obtained. This second model will be referred hereafter as the "free-standing membrane". A schematic representation of both types of interfaces is presented in Fig. 36. It is clear that, in the free-standing membrane, the interface has expanded significantly and has become a lot rougher than its confined counterpart.

Note that most results displayed in the following sections are symmetrized about the relevant membrane center-of-mass (COM) so as to accumulate averages from both interfaces.

5.3.1. Characterization of the polyimide membranes

The features of these two model matrices are obviously strongly linked to their preparation procedure and they were compared to the 56025-atom bulk model presented in Fig. 33. The latter has a density of ρ_{bulk} = 1.378 g cm^{-3}, *i.e.* in excellent agreement (~0.7%) with the experimental value of 1.368 g cm^{-3}.[108]

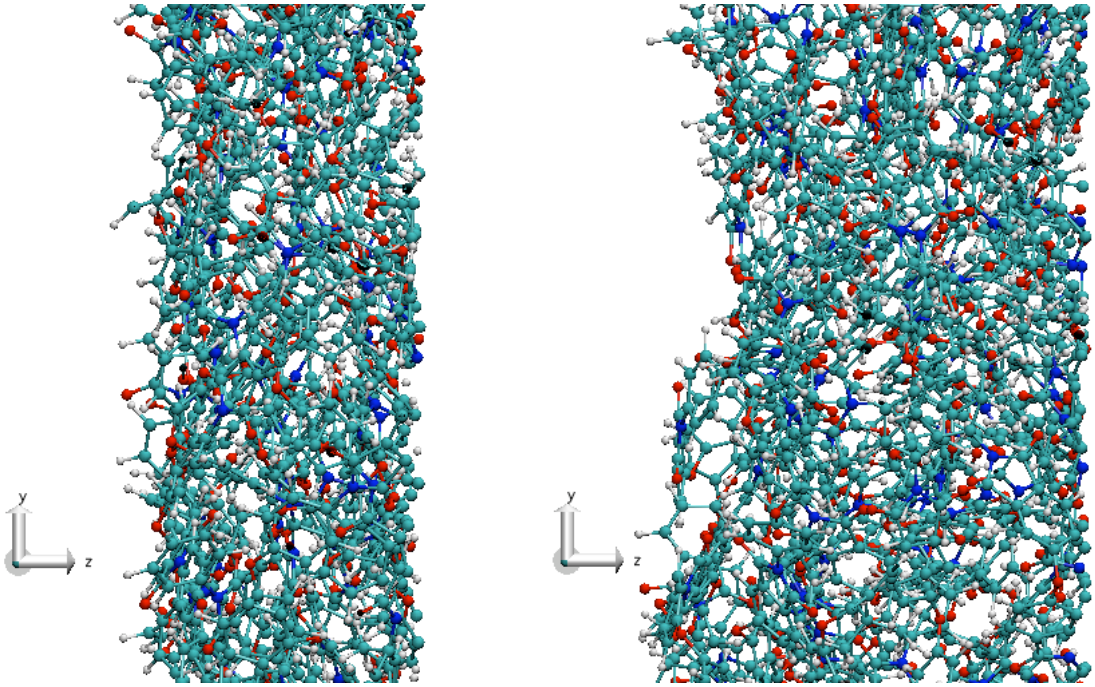

Fig. 36 *A close-up comparison of the left interfacial zone in the confined (left) and free-standing (right) ODPA-ODA membrane. Both snapshots have dimensions of ~30 Å along the y-axis and the color code is the following: cyan = C, red = O, blue = N, white = H.*[24,25]

5.3.1.1. Densities and location of the interfaces

Normalized mass density distributions, $\rho(\alpha)/\rho_{bulk}$, of the chains as a function of their distance α to the membrane COMs are shown in Fig. 37 along specific directions:

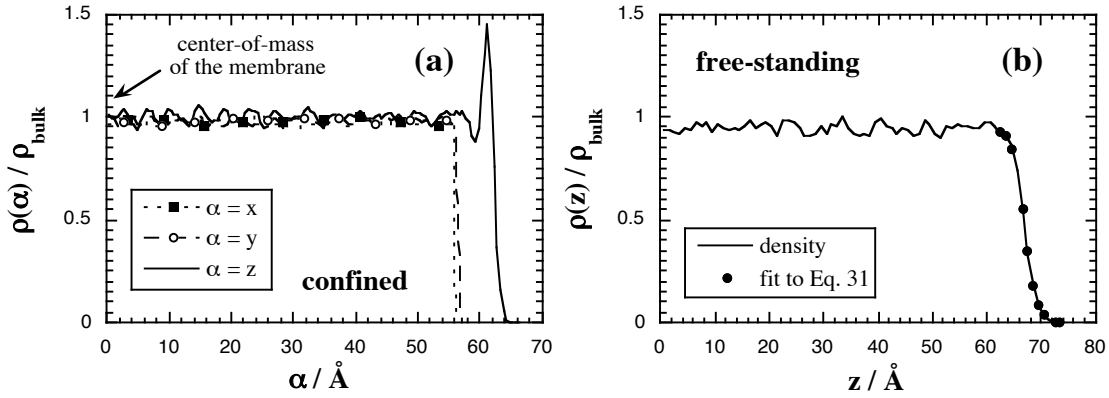

Fig. 37 *Mass density distributions for the polyimide atoms as a function of the distance from the COM of the membrane along different directions for (a) the confined and (b) the free-standing membranes. The slab width is 0.5 Å. In (b), the black circles originate from fits of the sigmoidal part of ρ(z) to the form of Eq. 31.*[24,25]

As expected from the film preparation, the $\rho(\alpha)$ do remain very similar to ρ_{bulk} for slabs spanning the full x and y lengths of the model. On the other hand, z is obviously affected by the compression. It is well-known that the polymer chains tend to form some densely packed layers at the vicinity of planar surfaces,[113-115,117-119,121,271] which is indeed reflected in the high-density peak of Fig. 37a with a peak at ~3.5 Å and a trough at ~6 Å from the interface, followed by an attenuated second layer of similar width. Interestingly, the film density is usually perturbed on a relatively limited range with respect to other properties.[117,119] Upon removal of the walls, the polymer matrix loses this high-density region and the middle part of the model relaxes towards ~95% of ρ_{bulk}, which is a direct result of the flattening of the chains during the membrane construction phase. Here again, the free-standing model is in agreement with results from the literature,[102-106,120,122-129] which usually report the density profile at the free-standing surface as being sigmoïdal. While it is relatively easy to locate the interface of the confined membrane at ~65 Å, there are several possible definitions for the more subjective interfacial thickness of a free-standing membrane.[105,120,122-124,126] A common way is to fit the sigmoïdal part of the mass density curve $\rho(z)$ to the following hyperbolic equation:[272,273]

$$\rho(z) = \rho_{middle} \frac{1 - \tanh\left[2(z-h)/w\right]}{2} \qquad (31)$$

where ρ_{middle} is the density of the middle region of the film, h is the location of the interface and w is the interfacial width. $\rho(z)$ does fit very well to the form of Eq. 31 and the resulting normalized curve is displayed as filled circles in Fig. 37b. The optimized parameters are h = 66.9 Å for the location of the interface, and w = 4.5 Å for the interfacial width. The interface can also be located by determining the point where $d\rho(z)/dz$ is at its minimum value near the free surface,[123] *i.e.* in that specific case, h = 65.5 Å.

5.3.1.2. Chain structures

To characterize chain alignments, the second order Legendre functions, $P_2(\cos\theta_Z)$, are displayed in Fig. 38, with the angle θ_Z for a triplet of pivot-angle atoms $\{i, j, k\}$ being that between the z-axis and the vector between atoms i and k.[22] The P_2 functions are defined as:

$$P_2(\cos\ \theta_z)\ =\ \frac{3}{2}\ <\cos^2\theta_z>\ -\ \frac{1}{2} \qquad (32)$$

and are especially interesting since their limiting values, with respect to the normal to the interface, are -1/2 for a perfectly perpendicular alignment, 1 for a perfectly parallel alignment and 0 for a random alignment of the vectors defining θ_z (Fig. 38):

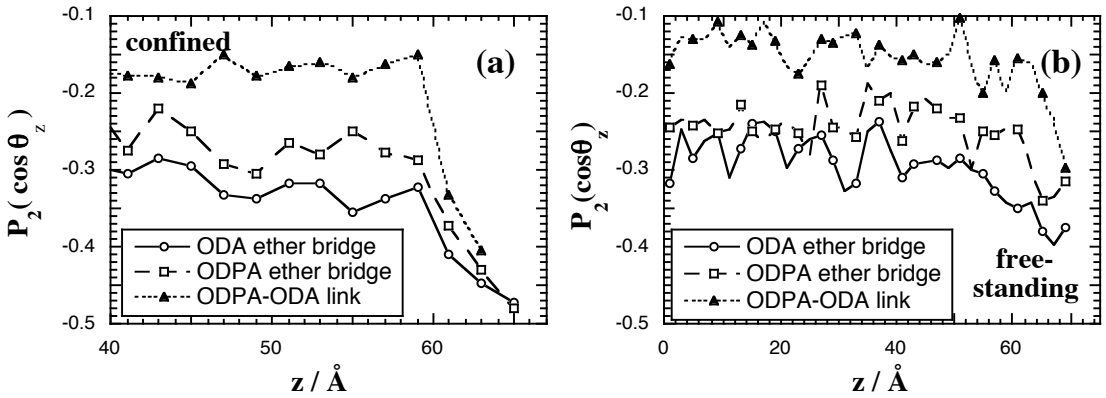

Fig. 38 *P_2 Legendre functions (Eq. 32) for selected pivot angles in (a) the confined and (b) the free-standing membranes. The slab width is 2 Å.*[24,25]

In the initial confined membrane (Fig. 38a), there is a tendency towards a parallel alignment of these backbone angles with respect to the surface, and thus, by consequence, an alignment of the chains, which has also been seen elsewhere.[113,114,118,119,122] Fig. 39 shows that the polyimide aromatic rings align in the *x-y* plane:

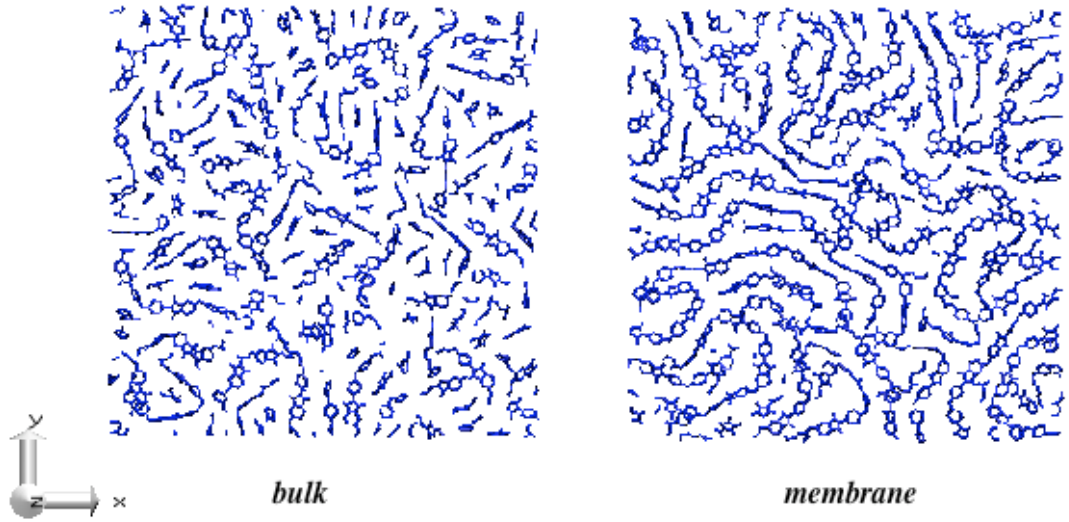

Fig. 39 *A comparison of cross-sections of 5 Å-width along the z-axis. Only polyimide backbones are displayed. The left was taken from the middle of the 56025-atom bulk while the right comes from the confined membrane closest to one of its interfaces.*[24]

Such an effect is very pronounced at the immediate vicinity of the interface, where the angles are almost perfectly parallel to the surface (Figs. 38a and 39). However, the alignment of the chains, which obviously originates from the flattening induced in the chains by the compression step, persists into the core of the model. Despite its very large magnitude, our confined membrane does not attain true bulk behaviour at the centre, and the very low mobility of the glassy chains ensures that this remains throughout the simulations. The free-standing membrane (Fig. 38b) retains the features of the confined system, but does not show the same precipitous fall in $P_2(\cos \theta_z)$ towards -1/2 at the interface. While a pronounced alignment of the chains in the vicinity of the interface has been extensively described in the literature for confined systems,[24,113,114,118,119,122] it is known to be present but attenuated in a free-standing membrane.[102-104,122,124,127] Indeed, the tendency for parallel orientation has been shown to decrease with increased roughness,[126] which is characteristic of a free-standing interface.

The mean square radii of gyration of the chains, $\langle S^2 \rangle$ were accumulated in slabs of 5 Å-width according to the z distance to a given membrane COM, and resolved into their components perpendicular, $\langle S_\perp^2 \rangle$, and parallel to the interfaces. Such an histogram is displayed in Fig. 40a for the confined membrane. If it was isotropic, $3 \langle S_\perp^2 \rangle$ would be equal to $\langle S^2 \rangle$, which is not the case. Indeed, there are almost no contributions to $\langle S^2 \rangle$ in the direction perpendicular to the interface, and the main components are the ones parallel to the interface. The large variations in $\langle S^2 \rangle$ reflect the low number of chains contributing to a given slab but the $\langle S_\perp^2 \rangle$ show that the flattening effect also extends into the heart of the membrane model, even if the well-aligned chains in the immediate vicinity of the membrane are more flattened than the others. This tendency of surface chains to be flattened at the proximity of a solid surface is once again consistent with what has been seen elsewhere and has even been compared to "pancakes", *i.e.* a nearly two-dimensional behavior.[113-115,117,118,274] It remains, albeit slightly attenuated in the free-standing model.

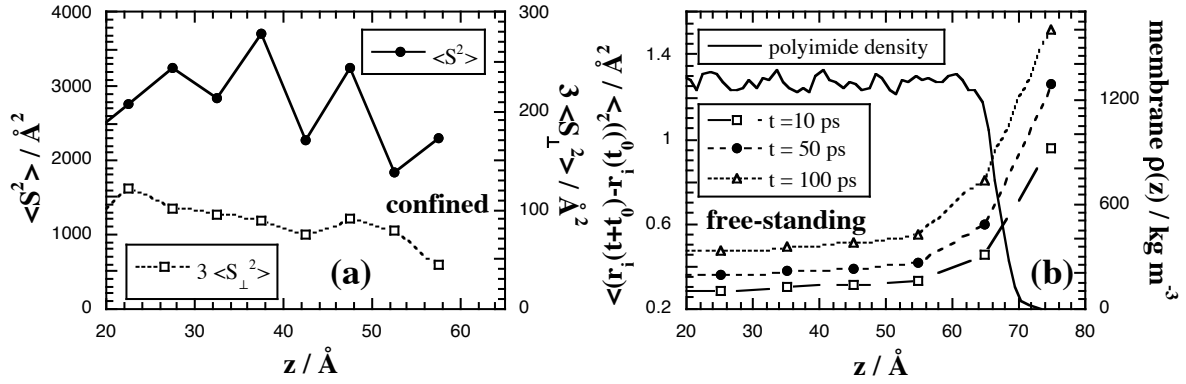

Fig. 40 *(a) Left axis: the total <S²> as a function of the z distance from the chains COM to the confined membrane COM (filled circles). Right axis: its component perpendicular to the membrane surface multiplied by three (open squares). (b) Left axis: polyimide MSDs as a function of z in the free-standing membrane after different time-intervals t. Right axis: polyimide mass density ρ(z) with a slab width of 1 Å.*[24,25]

5.3.1.3. Dynamics

In the confined model, the polyimide MSDs are typically less than 1 Å^2, thus showing that the matrix has very little mobility. However, in free surfaces of glassy atactic PP,[120] Mansfield and Theodorou had reported enhancements in the small MSDs of polymer atoms in the vicinity of the interface. This can indeed be seen in Fig. 40b, where the MSDs are averaged for different time-intervals t for all polymer atoms situated initially at initial time t_0 in slabs of width 10 Å. For comparison, the polyimide density profile is also given in Fig. 40b. While the absolute values for the polyimide MSDs remain very small, there is undoubtedly an enhancement of atomic mobility close to the interface, which Mansfield and Theodorou attributed to the lower density prevailing there.[120] Similar to their and other work,[22] this dynamical feature extends further into the polymer than the mere perturbation of density (Fig. 37b), and what has been called the "dynamical interfacial thickness" is indeed about twice as large as the thickness obtained from the mass density profile. Such a transmission of enhanced mobility has been attributed to molecular connectivity[120] and the increase of local diffusivity at the free surface has been reported in several other studies of both rubbery and glassy polymers.[123,128,275]

5.3.2. Permeation of small gas probes

The membrane investigations suffered from the same limitations than the box size influence (Sec. 5.2.4.), *i.e.* the polyimide matrices were prepared with the full potential including the van der Waals and electrostatic interactions,[17,21] but at extreme computational costs for the larger systems. We thus adopted a compromise in which the gas permeation phase was speeded-up in a less-realistic way, but could be compared to reference bulk systems simulated under the same conditions.

In the confined membrane, the 70-times faster U_{WCA} was used instead of $U_{LJ}+U_{coul}$, since it had proven to be a reasonable approximation for small penetrant diffusion: the trajectories are similar, the diffusion coefficient is almost the same[21] and it allowed us to simulate up to 10 ns. Of course, caution has to be exercised when using a purely repulsive potential approach, but here the glassy matrix is hardly modified and, unlike larger penetrants, He is a weakly-interacting gas.[249,250,259,260] However, we were faced with another problem: permeation is governed by *both* diffusion and solubility, the latter being already quite low for He in polyimides compared to other gas molecules.[249,250,259,260] Since the switch to a WCA potential reduces even more the penetrant solubility, we kept the same ε as helium,[235] but decreased its σ to 1.88 Å. This gave the same solubility coefficient in the confined ODPA-ODA for the test-probe with U_{WCA} than that obtained with helium and U_{LJ}, *i.e.* 0.06 cm^3(STP) cm^{-3} bar^{-1}.[21] On the other hand, the introduction of full van der Waals and electrostatic interactions to maintain the cohesion of the free-standing membrane means that we could have reverted to the realistic Lee potential for helium[235] in the second model. However, considering the huge slow-down in terms of computational time (~26000 h monoprocessor on an IBM Power 4 for only ~1 ns of simulation), it was decided to keep the gas probe σ at 1.88 Å in order to follow its motion with sufficient statistics by increasing both the solubility and the diffusivity over the 1 ns available for the free-standing film model. The gas-gas interaction parameters were switched off completely so that the gas behaved ideally. The number of probes to introduce into a membrane model (a total of $n_p + n_f$) was obtained using the procedure described in Sec. 5.2.2 (Eqs. 20 and 23), which gave 1780 gas probes for the

confined and 3280 for the free-standing membranes. Half the penetrants were randomly inserted into the free space on one side and the remainder into the free space on the other side of their polymer matrix.

While the test gas probes described above were inspired from helium, they could not be directly compared to the former systems.[108] As a consequence, pre-prepared ODPA-ODA bulk models were run with the same modified probe parameters. Permeation in the confined membrane was directly compared to that of the 56025-atom bulk model using σ = 1.88 Å, 225 gas probes and U_{WCA}. In the case of the free-standing membrane, two reference bulk systems were considered. The first one was the 6225-atom model also used previously,[21] which had a density of 1377 kg m^{-3}, and is referred to afterwards as the "normal-density" bulk. In order to make comparisons with the lower density of the free-standing film, the "normal-density" bulk was expanded smoothly to create a second reference bulk, the "95%-density" system, with a final value of ρ_{bulk} = 1301 kg m^{-3}. 25 gas probes were inserted into each of these two reference bulk models with respect to the free-standing membrane.

5.3.2.1. Individual trajectories

Typical trajectories for gas probes crossing the membranes are displayed in Fig. 41:

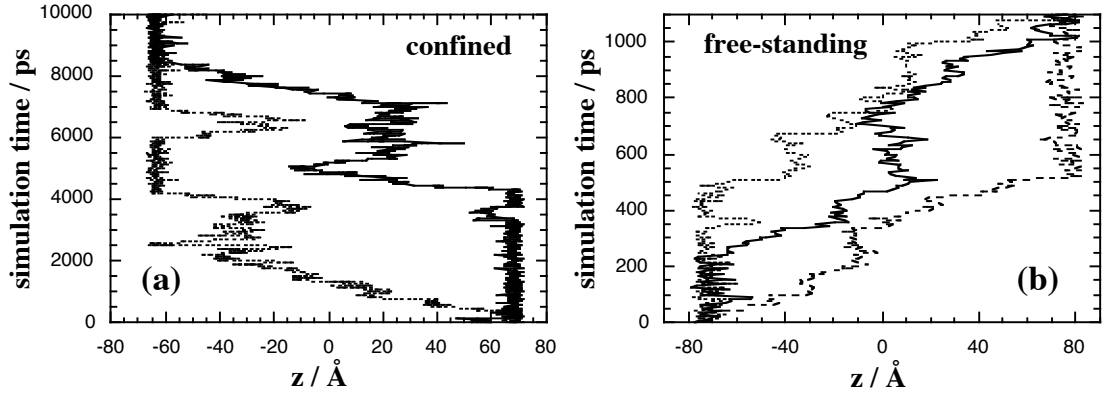

Fig. 41 *Trajectories of gas probes along the z direction of the (a) confined and (b) free-standing membrane models.*[24,25]

The use of a smaller σ for the gas probe does not qualitatively change the behaviour with respect to helium (Fig. 29a), but the times of residence within specific holes of the polymer matrix are even more reduced and positional fluctuations are larger. The probes

remain for various times on either side of the membranes, but once inside, behave in very similar ways with a continuation of efficient jumps and very little time spent at a given site. To assess whether diffusion in the *x* and *y* direction occurs on the same extent than that in the *z* direction, gas MSDs can be recorded as a function of time *t* for all probes situated at initial time t_0 in the region 10 Å to either side of a model COM. The MSDs can then be resolved into their components along the *x*, *y* and *z* axes. The results are given in Fig. 42:

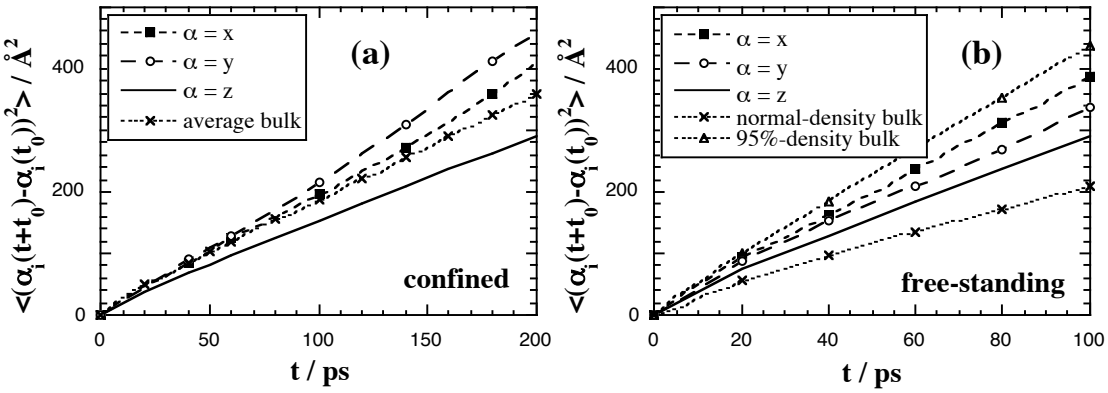

Fig. 42 *Individual x, y and z components of the MSDs for penetrants situated in the region 10 Å to either side of the (a) confined and (b) free-standing membrane COMs at time t_0. The x, y and z components for each reference bulk model have been averaged together since they were isotropic.*[24]

Note that, by choosing probes in the middle of the membrane and restricting the analyses to relatively short time intervals, the influence of the gas atoms which diffuse out of the membrane is minimized. Unlike the bulk systems, short-time diffusion is obviously anisotropic in both membrane models, which is especially visible in the confined membrane. Indeed, the *z*-component of its gas MSDs is systematically lower with respect to the bulk by ~20%. On the other hand, it is compensated by an increase in both *x* and *y* components. The alignment and flattening of the chains in the confined model thus leads both to a more difficult "straight" crossing of the membrane, and also to a slight channeling effect along the *x*-*y* plane (Fig. 39). The free-standing membrane retains the features of the confined membrane, but the relaxations of the density and structures allow the MSDs to get closer to the 95%-density reference bulk. This suggests that transport is more efficiently carried out.

5.3.2.2. Diffusion coefficients in the membrane models

Considering the set-up of the membrane models, the gas concentration, c, is expected to vary as a function of both the z-position and time t; it should thus be referred to as $c(z,t)$. However, the simplest and most common way of solving the one-dimensional Fick's law diffusion equation is through the identification of a regime in which the gas probe diffusion coefficient $D_{membrane}$ is assumed to be independent of both z and concentration.[276,277] In terms of time, a linear relationship between the weight gain of the polymer and $t^{1/2}$ is characteristic of Fickian diffusion.

With our polyimide surfaces (Fig. 36), the first problem is to define the width L of a specific membrane. For the confined system and its associated 10-ns simulation, the penetrant concentration in the membrane should tend at long times towards a constant consistent with its solubility and the effective external pressure of the gas. Fig. 43a shows a close-up in the vicinity of the interface of the symmetrized slab mass densities for both the gas and the polyimide in the 6-10 ns interval, which as will be seen in Fig. 43b, correspond to the steady-state regime:

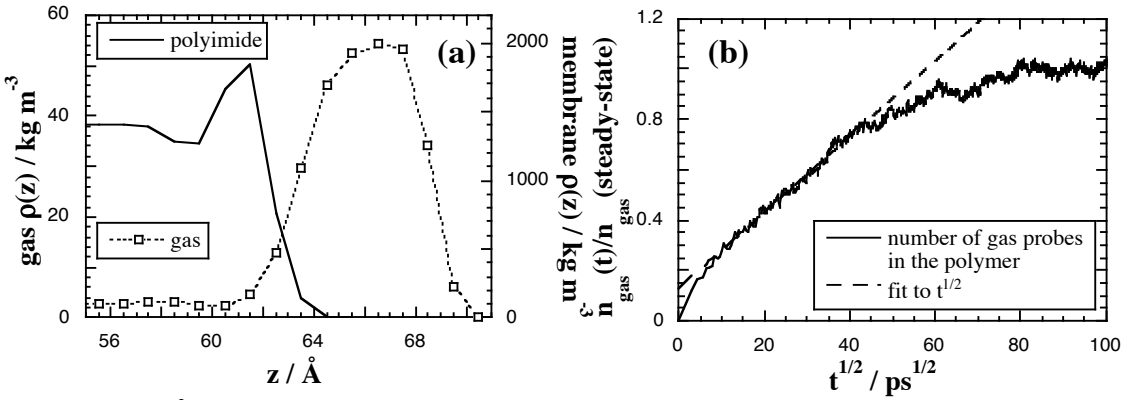

Fig. 43 *(a) 1Å-wide slab mass densities as a function of z averaged over the 6-10 ns interval of the production run for the gas (left axis) and the confined polyimide (right axis) (b) The number of gas probes in the confined membrane at time t divided by the number found in the steady-state regime, shown over the 10 ns of the production time (solid line). For a better identification of Fickian diffusion, the data is plotted as a function of $t^{1/2}$ along with a linear fit to $t^{1/2}$ (dashed line).*[24]

In Fig. 43a, the gas mass density remains quasi-constant up to $|z| = 61.5$ Å and then increases dramatically, indicating that the remaining probes can be considered as belonging to the gas reservoir. As the turning point also corresponds to the position of the density maximum in the first peak (Fig. 37a), *L/2* was defined as 61.5 Å for the confined membrane. Despite the limited width of the gas reservoir, an ideal gas phase is attained in its centre, since Widom's insertion probability in this region is equal to 1. The equilibrium gas density at the mode can be used to estimate the partial gas pressure using the ideal gas law, $P_{gas}V=n_{gas}k_BT$, which gives P_{gas} = 340 bars. Fig. 43b presents the relative number uptake of gas probes in the confined membrane as a function of $t^{1/2}$. Following the first entry of probes in the membrane, the uptake curve scales linearly as $t^{1/2}$ from 100 to 2000 ps, thus suggesting that gas diffusion is consistent with a single value of $D_{membrane}$ in that time-interval. After 2000 ps, gas probes have had time to diffuse through the entire membrane and start to exit in significant numbers through the second interface. The uptake curve then tends towards a plateau which is attained at ~6000 ps. Of course, afterwards, gas probes keep going in and out of the membrane but their total number within the polymer remains quasi-constant, as well as the average numbers in each reservoir, thus defining steady-state (Fig. 43).

The definition of the width is a lot less obvious for the free-standing membrane since several possible definitions are possible (Sec. 5.3.1.1) and the surface of the membrane is highly heterogeneous (Fig. 36b). Fig. 44 shows the free-standing data comparable to the confined case of Fig. 43. Since the curves are a lot smoother, we considered *L/2* = 60.5 Å corresponding to the start of the dense part of the membrane, *L/2* = 66.9 Å obtained from Eq. 31 and *L/2* = 65.5 Å referring to the point where $d\rho(z)/dz$ passes through a minimum at the interface. In addition, the number uptake was also studied under the hypothetical condition that *L/2* = 50 Å, which would be situated well inside the dense part of the model:

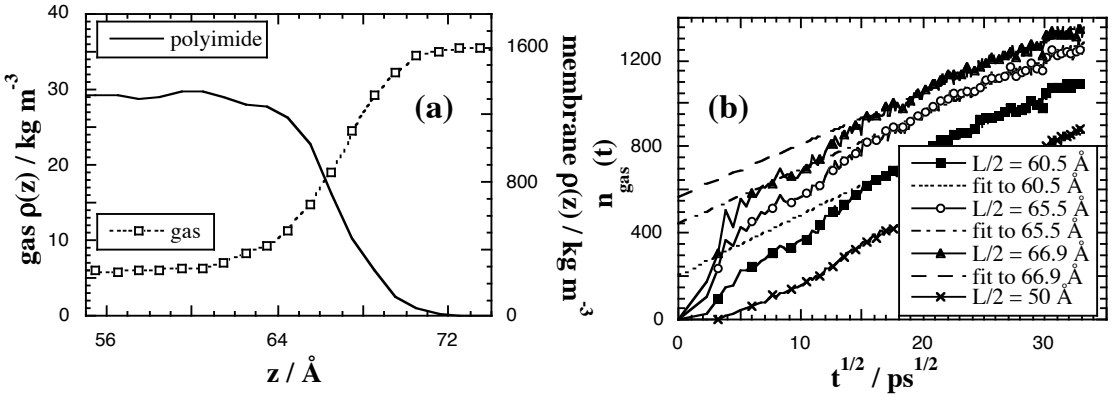

Fig. 44 *Same legend as Fig. 43 but for the free-standing membrane on a much more limited timescale. In (b) several values related to the interface L/2 have been considered (see text and legend for details). The actual uptake curves are displayed with symbols and lines whereas the straight lines are the corresponding linear fit to* $t^{1/2}$.[25]

The uptake curves (Fig. 44b) differ at short times but their limiting slopes are very similar, thus showing that the actual location of the interface does not fundamentally affect the analyses. When *L/2* is defined as being 60.5 Å, 65.5 Å or 66.9 Å, the curves do not scale linearly as $t^{1/2}$ at short times. This is related to the initial filling-up of the interface by the gas where the diffusion coefficient varies with *z*. As the definition of *L/2* gets closer to the dense part of the polymer, this non-$t^{1/2}$ dependence of diffusion progressively disappears, as can be seen from the uptake curve of the hypothetical *L/2* = 50 Å. This indicates that the diffusion coefficient settles from a large value in the gas phase to a low constant value in the dense part of the membrane. It is clear that the available simulation time does not allow for the steady-state regime of the free-standing model to be reached. However, the equilibrium and non-equilibrium uptake curves are found to be superimposable in the confined membrane,[24] thus suggesting that the results are fairly insensitive to whether the membrane already contain gas probes or not. Although it is known that pressure can have effects in actual membranes depending on the diffusing molecule type,[278] the range of pressures applied here and the nature of the penetrant do not lead to any noticeable effects.

If $D_{membrane}$ is independent of *c* and *z* within the membrane, and diffusion in the gas phase is considerably higher, $D_{membrane}$ can be evaluated from fits of the time-dependent

density distributions to the following solution of the one dimensional diffusion equation in a semi-infinite system:[276,277]

$$c(z',t) = c_0\, erfc\left(\frac{z'}{\sqrt{4\, D_{membrane}\, t}}\right) \tag{33}$$

Here, z' is the coordinate in a reference system where $z'=0$ is the left edge of a membrane which extends to $z'=+\infty$. This solution is obtained given the following boundary conditions:- $c(z'\geq 0, t=0) = 0$; $c(z'=0, t > 0) = c_0$. In our case, where the membranes are of finite length L, we can define $z' = z + (L/2)$ where z is the coordinate in the frame of reference of the membrane COM; $z' = 0$ thus corresponds to one end of the membrane and $z' = L$ to the other. In addition, Eq. 33 will only be valid up to when gas probes begin to cross the membrane, *i.e.* ~2000 ps and ~500 ps for the confined and free-standing models, respectively (Fig. 41). Gas mass densities *vs.* time curves were obtained by artificially labelling gas probes as being on the "left", $z_i(t_0) < -L/2$, or on the "right", $z_i(t_0) > L/2$ at any particular time origin t_0 and then subsequently following the evolution of the distribution of these t_0-labelled atoms. In order to improve the resolution, all possible time origins were used and the distributions for "left" and "right" molecules were symmetrized. They are displayed in Fig. 45 for both membranes along with the corresponding fits to the form of Eq. 33:

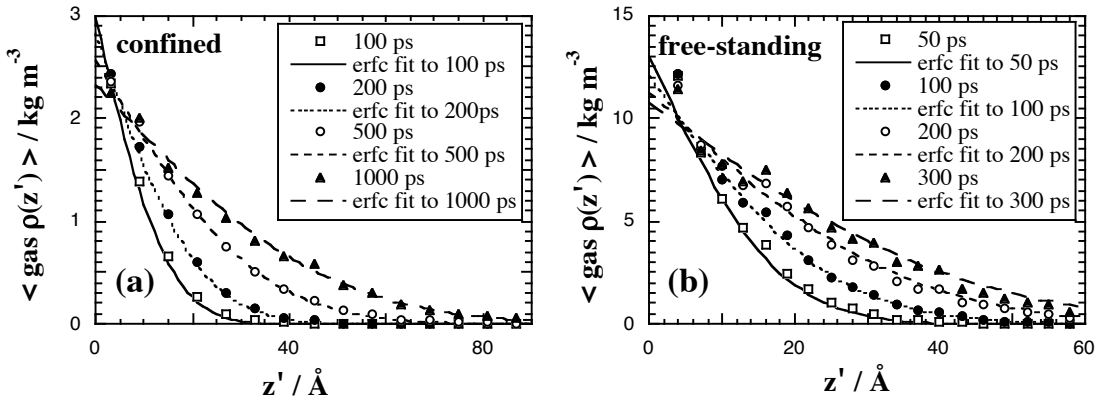

Fig. 45 *Mass density distributions in slabs of width 1 Å showing the diffusion of labelled gas atoms into the (a) confined membrane with L/2 = 61.5 Å and the (b) free-standing membrane with L/2 = 66.9 Å at different time-intervals. The actual profiles are displayed with symbols. The lines are fits to the form of Eq. 33 with a constant diffusion coefficient.*[24,25]

All the fits could be obtained with a constant diffusion coefficient of $D_{confined} = 6.8\times10^{-5}$ cm^2 s^{-1} and $D_{free\text{-}standing} = 1.9\times10^{-4}$ cm^2 s^{-1}. However, the erfc fits are only possible from about $z' = 6.5$ Å onwards in the case of the free-standing membrane (Fig. 45b), which corresponds to the region where the density approaches that of the middle region of the film. These fits are thus not valid in the smoothly decreasing $\rho(z)$ part of its interfacial region. Probes initially situated in the pure gas phase, i.e. at $|z_i(t_0)| > 72$ Å at time origin t_0, were thus followed and found to fill up almost entirely the irregular interfacial structure within 1 ps. Despite an intermediate behaviour between diffusion in the pure gas phase and that through the dense membrane, it is thus a lot closer to the former case. Diffusion is progressively reduced as the polymer density increases but it still remains a lot faster than transport in both reference bulk models (D_{bulk} = 1 to 2 Å^2 ps^{-1}) and only drops to a limiting lower value in the more dense interior regions of the membrane. Another problem with Fig. 45 is that the c_0 coefficient in Eq. 33 obviously slightly decreases with increasing t for both membrane models. The stationary source boundary condition, $c(z'=0,t > 0) = c_0$, justifiable in the case of a constant partial pressure of the penetrant gas in the reservoir, is not really consistent with the conditions used here, *i.e.* the partial pressure of the labelled gas probes in the (fixed volume) reservoir gradually diminishes as they diffuse into the membrane. Consequently, Eq. 33 cannot be considered on its own as fully appropriate for the determination of $D_{membrane}$.

In order to avoid the problem of the inappropriate boundary conditions, a second approach in which the solution of the one-dimensional diffusion equation is obtained numerically[276] was attempted. The range of each membrane in the z dimension was divided into equal intervals of δz = 1 Å and the range in t into intervals of δt = 0.1 ps. With finite difference methods, it is possible to obtain the concentration at the middle of a slab z and at time $t+\delta t$, c(z,$t+\delta t$) with good precision from the following numerical integration algorithm:

$$c(z,t+\delta t) = c(z,t) + D_{membrane}\,\frac{\delta t}{\delta z^2}\left(c(z+\delta z,t) + c(z-\delta z,t) - 2c(z,t)\right) \qquad (34)$$

provided that ($D_{membrane}\,\delta t/\delta z^2$) < 1/2.[276] The left edge z_{min} was defined as being -61.5 Å for the confined and -60.5 Å for the free-standing membranes in order to have a description

consistent with a constant $D_{membrane}$. At the start of the numerical integration, $c(z_{min},0)$, were set to the average steady-state gas mass density for the confined membrane, and to the inflexion point of all the gas density curves (Fig. 45b) for the free-standing membrane. The initial amount of gas in the reservoir to the left side of the membrane, $Q_L(0)$, was determined from the symmetrized integral of the actual average gas distribution. Over the integration loop, the amount of gas either remaining in the left-side gas reservoir, $Q_L(t)$, having diffused into the membrane, $Q_M(t)$, or having exited through the right interface situated at $z_{max} = -z_{min}$, $Q_R(t)$, was evaluated at each δt. These values were then used immediately to reset the imposed concentrations at the left and right edges of the membrane at each integration loop using:

$$c(z_{\min},t) = c(z_{\min},0)\,\frac{Q_L(t)}{Q_L(0)} \tag{35a}$$

$$c(z_{\max},t) = c(z_{\min},0)\,\frac{Q_R(t)}{Q_L(0)} \tag{35b}$$

This is possible given that diffusion in the gas reservoirs and the interfacial part of the free-standing membrane are significantly higher than that in both dense membranes, *i.e.* it can be assumed that the gas distributions in the reservoirs are always proportional to the equilibrium one. Using this approach, the best fits to the concentration density profiles at different times were obtained with values of $D_{confined} = 7.5\times10^{-5}$ cm^2 s^{-1} and $D_{free\text{-}standing} = 1.9\times10^{-4}$ cm^2 s^{-1}. They are displayed in Fig. 46 for the same time-intervals t than Fig. 45:

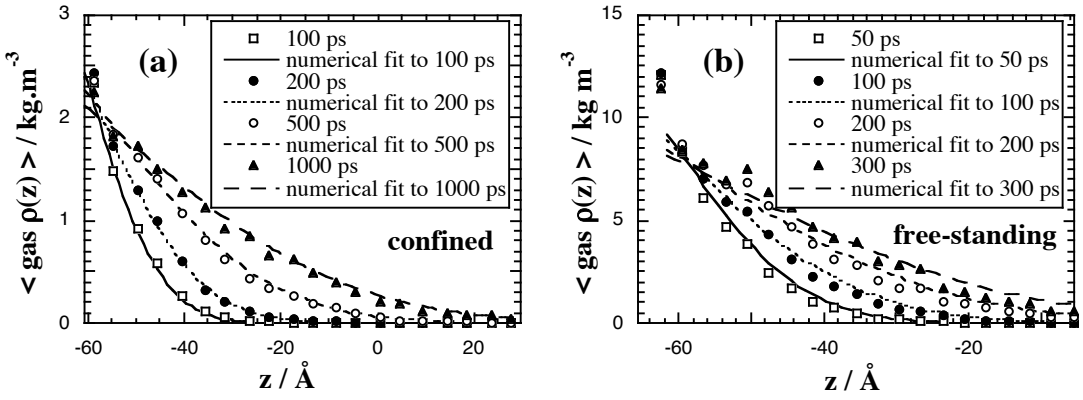

Fig. 46 *As Fig. 45 except that the lines are now from numerical solutions of the one-dimensional diffusion equation using the algorithm given in Eq. 34 and are displayed as a function of the z distance.*[24,25]

Since the specific boundary conditions are now well taken into account and the resulting $D_{membrane}$ is still close to that obtained from the analytical solution of Eq. 33, it can be safely assumed that the latter is a reasonable approximation. In addition, the numerical integration procedure was carried out up to 10 ns for each system under study and the predicted uptakes of gas probes were found to be superimposable to the actual uptakes. While this allowed for a basic check of the parameters used, it also revealed that the steady-state would probably not be reached before 3.5 ns for the free-standing model.

A third way to estimate $D_{membrane}$ is to perform a time-lag analysis, analogous to what is done experimentally[278,279] by following the quantity of penetrants that have crossed the membrane after a given time-interval *t*. The intercept on the time axis with the extrapolated linear steady state portion of the curve is the time-lag, θ, and is directly related to both *L* and to $D_{membrane}$ by:

$$D_{membrane} = \frac{L^2}{6\,\theta} \tag{36}$$

The resulting curve for the confined polyimide shows the typical profile[279] of a permeation experiment (Fig. 47):

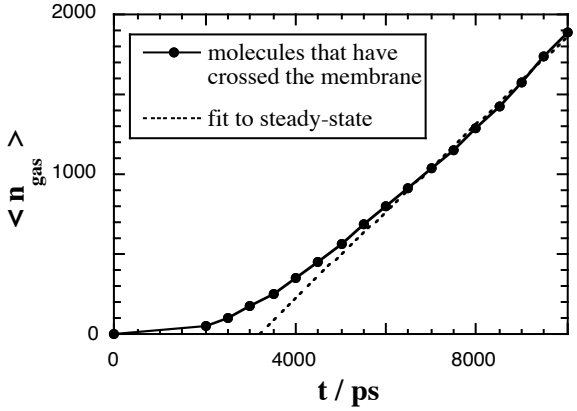

Fig. 47 *The average number of gas probes that at the time origin are on one side of the confined membrane but are found on the other side at a time t later. The dashed line is a fit to the curve in the steady-state regime, which allows the identification of the time-lag as the point of intersection with the time axis.*[24]

The time-lag of $\theta = 3170$ ps leads to a $D_{confined} = 7.9\times10^{-5}$ cm^2 s^{-1}, *i.e.* in very good agreement with those obtained previously. However, it could not be applied to the free-standing membrane since statistics could not be accumulated in the steady-state.

Diffusion coefficients in all three reference bulks were evaluated as described in Sec. 5.2.3. $D_{confined}$ was found to be very similar to its corresponding D_{bulk} thus showing that the diffusion of such small weakly-interacting gas probes is neither really affected by the presence of a high-density interface nor by the changes in polyimide chain configurations and packing. In the free-standing model, gas diffusion in the low-density part of the interface is so fast, that the limiting value for $D_{free\text{-}standing}$ is only attained when the probes enter more dense regions. It was found to compare well with D_{bulk} for the 95%-density bulk system, *i.e.* about twice that in the normal-density bulk. In that more realistic case, diffusion is thus mostly governed by the lower density prevailing due to the flattened chain configurations.

5.3.2.3. Solubility coefficients in the membrane models

Widom's insertion technique (Sec. 5.2.2), using the specific parameters for the gas probes under study, was applied to both the membranes and the reference bulks. The average insertion probabilities, $\langle p_{ip}(z)\rangle$ could be analyzed in slabs as a function of the z-coordinate of the test particle. In the confined case, it is also possible to obtain independently $\langle p_{ip}(z)\rangle$ from Eq. 23 by rewriting it as $p_{ip} = (n_p m_{gas}/V_p)(k_B T/P_{gas} m_{gas})$ where m_{gas} is the mass of helium, $(n_p m_{gas}/V_p)$ is the equilibrium density of the gas probe in the polymer, and P_{gas} is the equilibrium partial pressure of the gas in the reservoir. The results from both techniques displayed in Fig. 48a are superimposable, thus showing that Widom's insertion technique is well-suited to the estimation of gas solubility in these systems. Fig. 48b gives the $\langle p_{ip}(z)\rangle$ for the free-standing model obtained from Widom's insertion technique only.

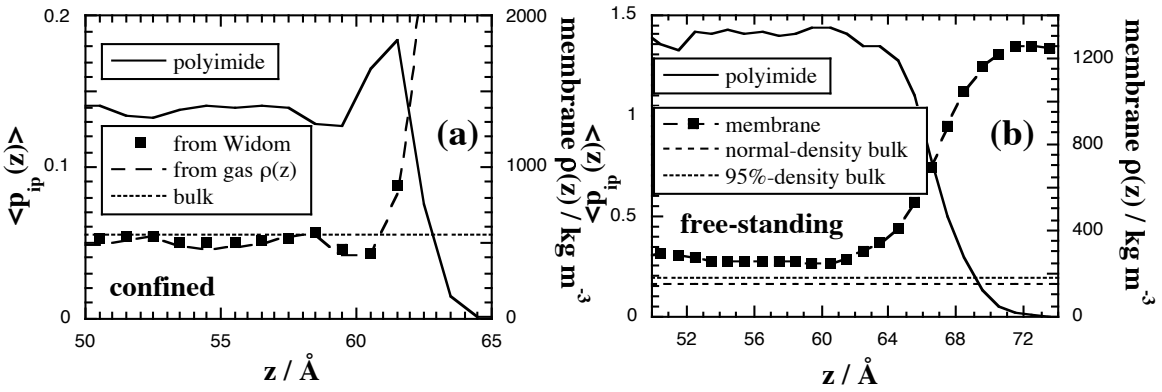

Fig. 48 *The average probabilities of insertion for the gas probes into the polymer, $<p_{ip}>$ as a function of z (left) compared to the polyimide mass densities (right) for the (a) confined and (b) free-standing models. The slab width is 1 Å and both membranes are compared to their respective reference bulk systems (short dash).*[24,25]

In the centre of the confined membrane (Fig. 48a), p_{ip} is quasi-identical to that in the reference bulk, despite the differences in chain configurations and alignments. A very slight dip in solubility is found close to the interface at a point coinciding with the inner part of the high-density peak in the polymer mass distribution. To check whether our results were not affected by U_{WCA}, Widom's insertion procedure was carried out with the realistic U_{LJ} in the membrane model using known parameters for He,[235] N_2,[212] and O_2[211]. All these tests confirmed a small drop of solubility with increasing density at the ODPA-ODA confined interface, which is insufficient to represent any real barrier to diffusion. It should be noted that the relationship between density and solubility[280] is not always straightforward. Higher density should lead to less space available for penetrants, *i.e.* lower solubility. On the other hand, high density leads to higher cohesion energy density, *i.e.* more solubility. The resulting p_{ip} is thus a compromise between these two effects.[263,281]

In the centre of the free-standing membrane (Fig. 48b), p_{ip} is approximately twice that of the normal-density reference polyimide bulk and 1.5 time higher than its 95%-density reference bulk, which must be related to the combination of both the density and the flattening of the chains. However, as the polyimide density decreases, the solubility then increases in a sigmoïdal way, reaching even values where $<p_{ip}(z)>$ are larger than 1. This reflects very

favourable interactions between the penetrants and the polymer chains at the interface which lead to adsorption of the gas probes. Consequently, in addition to faster diffusion, the low-density interface is also associated with higher solubility. This will thus even more increase permeation.

5.3.3. Perspectives

This work shows clearly that aligned and flattened conformations associated with the use of a solid wall or in a free-standing state are not likely to decrease on their own the permeation parameters, and that other factors are needed to explain the experiment/modelling discrepancies in our (ODPA/BCDA)-ODA copolyimides. We are currently testing the effect of more sophisticated helium-polymer combination rules, which have been suggested as being highly significant in these types of systems.[282] Different potentials for helium[283] could be assessed as well, but as mentioned before, oxygen and nitrogen model permeation were also found to be faster than in the associated experimental characterization.[112]

As far as the skin-effect results are concerned, it is important to note that they are valid within the specific conditions of the present models, and that they could be affected by a number of parameters, which also need to be addressed at a later stage. Although it was designed with respect to the experimental solvent-casting process, the preparation procedure of such a fully-atomistic large-scale glassy model remains non-trivial. In addition, solvent evaporation was not modelled explicitly and this could influence the chain configurations. Another open question is the size of the gas probes. As explained in the text, it was kept very small in an attempt to follow gas motion through the membrane with sufficient statistics. But, of course, it could be argued that larger probes, such as as O_2 or N_2, would modify to some small extent the structure of the rigid matrix.[249,250,259,260] With our current computational resources, this is presently a difficult problem to tackle if full electrostatic and van der Waals interactions are to be considered. Using a purely repulsive WCA potential as in the case of the confined membrane is useful but a lot less realistic. A last point for discussion is that, with hindsight, it is tempting to think that the central part of the model films could have been discarded. However, such a question could only be answered by a study of a smaller system

and it is also worth pointing out that the actual membrane model length of ~130-140 Å remains small with respect to the typical experimental dimensions of a few microns for thin-films.[108,112]

6. WATER TRANSPORT IN POLYIMIDE-BASED MEMBRANES

In addition to separation of light gases, polyimides are also promising as membranes for dehumidification of gases, air and organic vapours because of their high permeability to water vapour, H_2O.[207] Even without a specific set-up for permeation, these polymers are quite hygroscopic, which results in the absorption of up to a few percent water under ambiant environmental conditions, and can lead to a degradation of their dielectric properties.[284] We have carried out a comparative pilot study of PMDA-ODA and BCDA-ODA oligomers (chemical structures in Sec. 2.1.) in the absence and presence of 3.3% in weight of water. The latter is the water uptake at saturation by PMDA-ODA at 100% relative humidity and room temperature measured by a quartz crystal microbalance.[285] This work was undertaken at a time when our general hybrid PMC-MD procedure was not developed, and thus we chose instead to decorrelate 4-*mers* oligomers at high temperature using MD on its own. Once brought back to 300 K, these stiff oligomers (~150-200 atom *per* chain) settle into an arrested vitreous state showing little mobility afterwards, and as such, are a convenient first approximation for the real polyimides. It should also be noted that we characterized the oligomer/water interactions given an experimental estimate of the water content. While it is possible to calculate the equilibrium proportion of water in dense polymer systems at a given relative humidity using a combination of the thermodynamic integration approach and Widom's test particle insertion method,[286-288] we did not attempt this as yet.

6.1. Bulk properties

Two pure 27-molecules PMDA-ODA and BCDA-ODA oligomer bulks were decorrelated (Eqs. 9-11) at 1000 K, after which they were cooled down to 300 K. 3.3% water in weight was inserted into each pure model using the procedure described in Sec. 5.2., thus leading to two hydrated bulk models, which will be referred hereafter as the "PMDA-ODA+water" and the "BCDA-ODA+water" (Fig. 49) systems. The additional potential parameters for water were taken from the simple point-charge model, SPC/E, which provides a reasonable representation of bulk H_2O.[289] In all cases, the criterion for equilibration was that

of Suter and coworkers in their work on hydrated polymers[287,288] *i.e.* the absence of any drifts in density larger than 3×10^{-4} g cm^{-3} ps^{-1} during the last 100 ps of the equilibration procedure. Production runs were of the order of 2000 ps, while an additional SPC/E water simulation was undertaken for comparison.

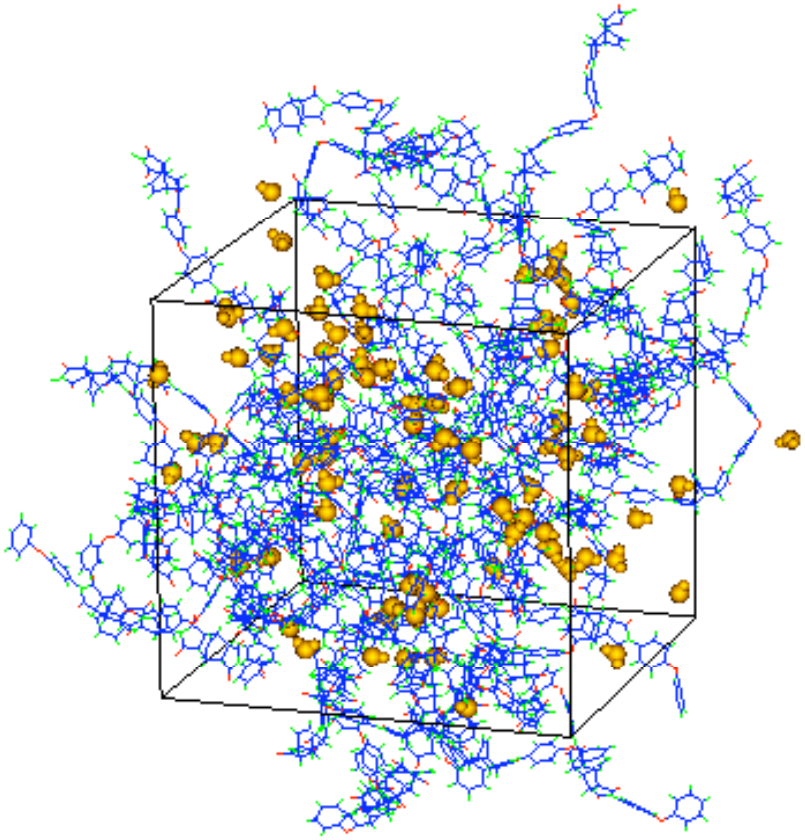

Fig. 49 *The BCDA-ODA+water simulation box. The oligomers are displayed by their wire-frames and water molecules are shown in a space-filling representation.*

Table VIII gives the average bulk properties at 300 K for the five systems under study. Linear combination rules for the volumes and the energies are not obeyed for the hydrated models. The oligomer densities are slightly lower than the long-chain experimental values of 1.395 g cm^{-3} for PMDA-ODA[290] and 1.326 g cm^{-3} for BCDA-ODA (Table V). As seen elsewhere,[291] the introduction of 3.3% water leads to a slight increase in density, which corresponds to an expansion of volume *per* water molecule of ~11.5 Å^3, i.e. very similar in both oligomers but significantly less than the 30.0 Å^3 occupied by each water in the pure liquid state. Experimentally, the molecular volume of several solvents has been shown to be

systematically smaller in polyimide matrices than in the pure state.[292] The intermolecular energies $\left\langle U_{pot}^{inter} \right\rangle$ suggest that water increases the cohesion for both oligomers, while the differences in the total potential energies $\left\langle U_{pot}^{total} \right\rangle$ allow us to estimate the changes in enthalpy ΔH_{mixing} associated with hydration by 3.3% water: ΔH_{mixing} is found to be around -4.5 kJ mol^{-1} for both systems, the $P\Delta V$ term being negligible by comparison. Enthapically at least, the simulations do predict a favourable hydration.[285]

Table VIII *Average bulk properties.* $<\rho>_{model}$ *are in g cm*$^{-3}$ *and the volumes of the MD cells* $<V>$ *in Å*^{3}*.* V_{expans} *is the volume expansion per water molecule in Å*^{3}*. The potential energies are quoted in kJ mol*$^{-1}$ *molecule*$^{-1}$*.* $<S^2>$ *are in Å*^{2}*. The figures in parentheses are linear estimates based on values for the pure components. For non-quoted error bars, see original reference.*[18]

Properties	PMDA-ODA	PMDA-ODA+water	BCDA-ODA	BCDA-ODA+water	water
$<\rho>_{model}$	1.381	1.402	1.250	1.272	0.995
$<V>$	49730	50630 (52070)	59240	60200 (61760)	7580
V_{expans}	-	11.5±0.8	-	11.4±0.9	30.0±0.1
$\left\langle U_{pot}^{total} \right\rangle$	-137.3	-175.8 (-171.0)	-345.4	-385.7 (-381.7)	-46.6
$\left\langle U_{pot}^{inter} \right\rangle$	-128.6	-166.0 (-162.3)	-118.0	-159.2 (-154.3)	-46.6
$<S^2>$	223±10	222±10	167±10	168±10	-

6.2. Polyimide structures and void-spaces

As seen from $<S^2>$ in Table V, water does not have any noticeable effect either on the configurational or the conformational characteristics of the oligomers, thus suggesting that the disruption of the chain matrix upon water uptake is rather minimal. The PMDA-ODA structures are more compact than their BCDA-ODA counterparts (Sec. 5.1.1.) and display a tendency to pack through parallel stacking of the dianhydride unit either with itself or with a

diamine unit, in agreement with both experimental *d*-spacings,[293] and the existence of charge-transfer complexes.[216] However, in all cases, water seems to have a very limited effect on chain-chain interactions.

The morphology of the void space was analyzed using the same probe-insertion procedure as described in Sec. 5.1.3., but with a probe radius of 2.45 Å, which corresponds to the closest water O…O distance found. While the percent of probe-accessible volume (*%PAV*) is 1.88% for both dry polyimides, it is only 0.87% for the PMDA-ODA+water and 1.38% for the BCDA-ODA+water systems. This suggests that the underlying distributions are actually quite different (Fig. 50):

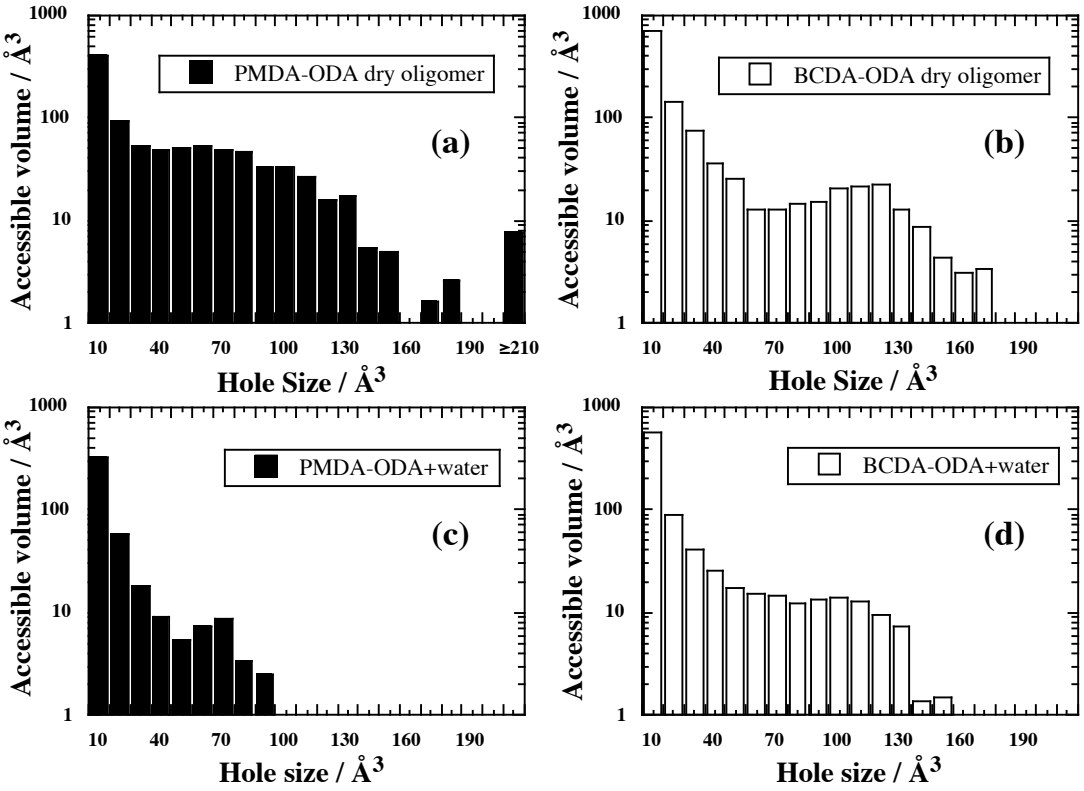

Fig. 50 *Distributions of PAV for a 2.45 Å probe with an interaction parameter of R_p = 0.70 Å as a function of the hole size. (a) and (b) are for the PMDA-ODA and BCDA-ODA dry oligomers. (c) and (d) are for the PMDA-ODA+water and BCDA-ODA+water systems.*[18]

The dry PMDA-ODA distribution (Fig. 50a) shows the monotonically decreasing form found for several polyimides[224,228] but the dry BCDA-ODA (Fig. 50b) displays a bimodal

form with more small and fewer larger holes. Following the inclusion of water, the mid-size and large holes disappear in the PMDA-ODA+water system (Fig 50c), as they are very easy to access directly. The trend is much less pronounced in the BCDA-ODA+water system (Fig 50d) where the holes are smaller and their accessibility to the water molecules more uniform.

6.3. Water structure and mobility

Radial distribution functions for oligomer-water interactions show that two sites on the chains are favoured for hydrogen-bonding coordination with water molecules, namely the ketone oxygens on the dianhydride and to a lesser extent the ether oxygens on the diamine moieties. On the other hand, water-water radial distribution functions exhibit even stronger peaks corresponding to the formation of water clusters. Fig. 51a displays the average numbers of water oxygens (*i.e.* of water molecules) around their three main types of ligands:

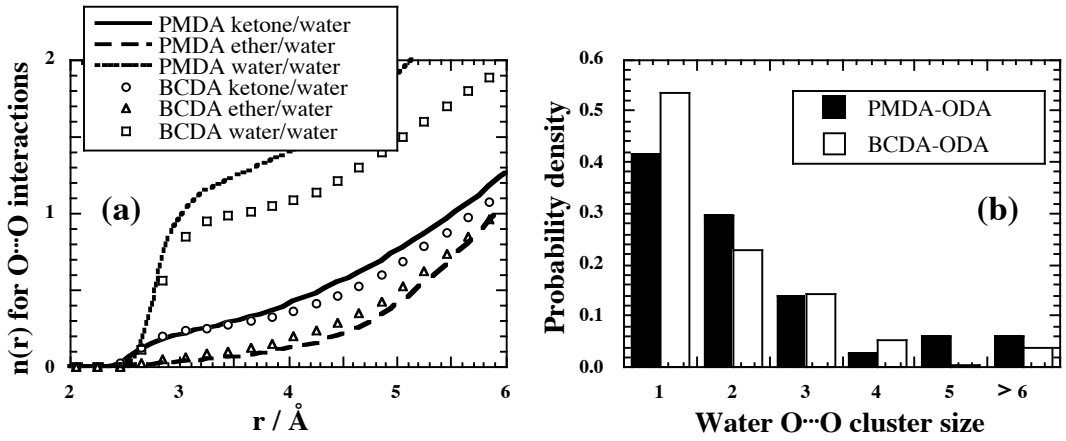

Fig. 51 *(a) Average numbers of water O as a function of distance around a ketone O, an ether O or another water O in the PMDA-ODA+water and BCDA-ODA+water simulations. (b) Histograms showing the probability densities of water clusters as a function of their size in both hydrated polyimides.*[18]

The general features are the same, *i.e.* water coordinates preferentially to water O > ketone O > ether O. Fig. 51b gives the underlying probability densities of water clusters obtained by identifying all water oxygens within 3.5 Å of another water oxygen (*i.e.* the first trough in the radial distribution functions), following the redistribution in the early stage of

both simulations. It confirms that there is a larger degree of water aggregation in the PMDA-ODA oligomer in agreement with the larger hole sizes in its void space, while smaller holes in BCDA-ODA tend to favour isolated molecules. It is thus obvious that the degree and nature of water coordination to the polymer will be dependent on the features of the void space in the different oligomers.

The existence of two basic types of water molecular sites in polyimides is in full agreement with experimental characterizations and other simulations.[294] Van Alsten et al. analyzed infrared spectra for a variety of polyimides at saturation and concluded that water exists both in an isolated form, *i.e.* hydrogen-bonded to the chain backbone, and in clusters consisting of small numbers of water molecules.[295] This two-sites picture is confirmed by dielectric relaxation and deuteron NMR studies,[296] as well as by proton, deuteron and oxygen-17 NMR.[297] It is interesting to note that another carbon-13 NMR study identified the carbonyl group of the imide ring as a preferential site for the aggregation of water molecules.[298]

Diffusion of water molecules was found to occur on the nanometer scale, but it was insufficient to obtain the crossover from the anomalous regime to Einstein diffusive behaviour at 300K.[291,299] There was thus little meaning in trying to extract the diffusion coefficient D_{water} using Einstein's equation (Eq. 25). Nevertheless the anomalous regime could be characterized using the probability density distributions of water oxygen displacement components (Eqs. 26, 27 and 28), as described in Sec. 5.2.3. The decrease of the "time-dependent" diffusion coefficients, $D_2(t)$ (Eq. 28) was consistently slightly faster in the PMDA-ODA+water than in the BCDA-ODA+water system. This is likely to be related to single water molecules which get trapped in the small holes in the BCDA-ODA structure. However, the quantitative difference between both systems remains very small and the $D_2(t)$ values at 1000 ps could be used as an upper bound of the true water diffusion coefficient in our oligomers, i.e. $D_{water} \leq 3\times10^{-7}$ cm^2 s^{-1}.

Similarly to ionic motion in polymer electrolytes (Sec. 4), some typical trajectories of individual water molecules are shown in Fig. 52a:

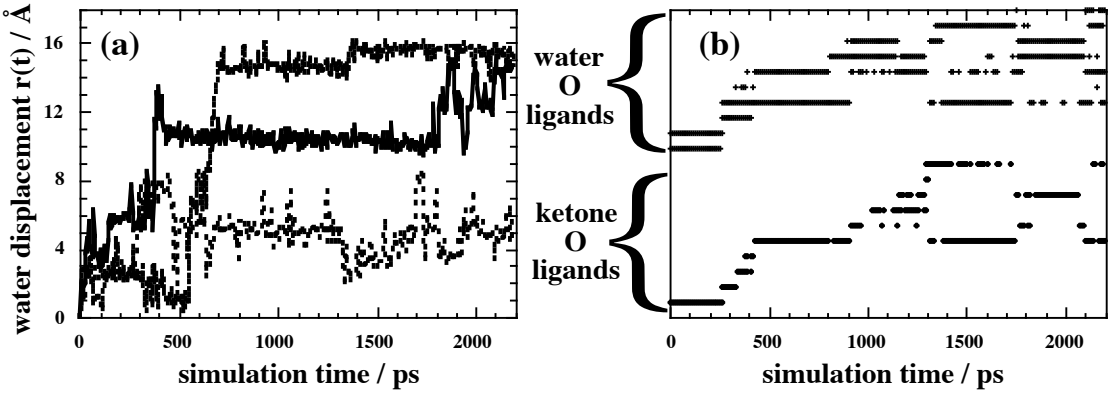

Fig. 52 *(a) Typical displacements of water molecules as a function of the simulation time. (b) Time evolution of the local environment around a particular water O undergoing motion between different sites. Dianhydride O and other water O that are found within a radius of 3.5 Å of the subject water oxygen over the 2200 ps PMDA-ODA+water simulation run are identified. Different lines indicate different ligands.*[18]

Once again, some molecules remain in a given site and fluctuate around their equilibrium positions, while others undergo jumps between different sites, thus leading to overall displacements. The hopping timescale between the different sites was found to be approximately 10-20 ps and the distance of a jump is typically 5-10 Å, *i.e.* a lot shorter than the gas penetrants (Sec. 5).

The time-evolution of the local environment around a water involves coordination to a series of different sites with an average coordination number of three oxygens for one water molecule. The water molecules that undergo significant motion are apparently mostly linked to dianhydride ketone oxygens and/or other water oxygens. Behaviour patterns include all four types of replacements in the coordination sphere of a given water oxygen, *i.e.* ketone to water, ketone to ketone, water to ketone, and water to water. An example of the progressive motion of a water molecule is displayed in Fig. 52b: it jumps between different dianhydride sites while moving either under a doublet or triplet form. It is interesting to note that water clusters easily associate and dissociate, as not less than ten other water molecules enter its coordination sphere over the analysis time. However, only doublets or triplets have enough stability to last more than a few ps, *i.e.* typically 300-500 ps. Successive dianhydride ligand

sites can either be found on the same or on different chains, since the water tends to coordinate to the closest available site in space. The possibility of a jump thus appears to be related to the presence of ketone oxygens, and to a much lesser extent to that of ether oxygens, in the near vicinity of the water molecules.

6.4. Perspectives

Despite the different geometries of the dianhydrides, hydrated PMDA-ODA and BCDA-ODA oligomers have obviously quite a few features in common. Indeed, they exhibit similar intramolecular flexibility, trends in the energy and density variations and identical probe-accessible volumes and oligomer-water interaction sites. However, they are clearly different as far as density, cohesion, intermolecular interactions, morphology of the void space and the degree of water clustering (given a 3.3% insertion of water) are concerned.

It is clear that the same approach needs to be extended to longer-chain polyimides if direct comparison between experimental and model data is to be attempted. This is currently under progress for PMDA-ODA (Kapton®), within the framework of a general combined experimental[300]-modelling project on water transport in a series of glassy polymers. In the same vein than Müller-Plathe and coworkers, a more complete study should involve several fractions of water as well as the influence of temperature on water and polymer dynamics.[291,294,299,301,302] Interesting features are the mechanisms underlying water sorption, using either specific techniques to estimate the excess chemical potential of water in bulk systems,[286-288] or a real membrane model such as that analyzed in Sec. 5. Other types of solvents could be considered as well.[303]

7. SPECIFIC INTERACTIONS BETWEEN A SILICA NANOPARTICLE AND FLEXIBLE OLIGOMERS

Polyimide-based composites are potential candidates for nanostructured reinforcements and increased mechanical properties,[304] even if research is still at its early stages.[305] However, as mentioned in Sec. 3.3., specific molecular modelling techniques are still to be developed in order for rigid long chain models to adapt to inclusions such as inorganic fillers. To our knowledge, there has only been one attempt to obtain molecular structures of polyimide/silica systems, using the aforementioned coarse-graining model for BPDA-APB[131] and a 6-Å-radius "hard-sphere" silica nanoparticle, but only as an input source towards the development of a micromechanics model.[304] In this work, we thus considered shorter flexible PEO chains, which are often used as dispersants for silica,[306,307] so that complete decorrelation of the starting structures could occur on the timescale available to MD simulations. While it is known experimentally that bridging flocculation can happen when high molecular weight PEO is used,[308-311] smaller polymers are able to saturate the silica surfaces and stabilize the systems.[312-314] This prevents agglomeration and leads to a good dispersion of the silica particles, a property that has numerous applications in material, pharmaceutical and biological fields.[315]

Many parameters influence the adsorption of PEO on the silica surface,[145-147,307,314-320] among which the end-groups for short chains of similar molecular weight.[145,149,150] In a microcalorimetric study, 9-*mers* PEO of average molecular weight 400 which only differed by their end-groups (one being dihydroxylated and the other one dimethylated), were found to exhibit significantly different adsorption isotherms.[145] The former is associated to a two-plateau adsorption curve, which has been interpreted as hydroxyl-capped PEO molecules being able to partially stand up with respect to the silica surface at maximum adsorptions, thereby allowing for the adsorption of more PEO.[145-150] On the other hand, only very weak sum frequency generation (SFG) vibrational spectroscopy signals are obtained for the dimethylated case.[151] Since the present work was initially associated to a lab project involving characterization of the PEO dispersing power by microscopy,[321] both -CH_3 for "dimethyl

PEO" and -CH_2-OH for "dihydroxyl PEO" end-groups for 9-*mers* PEO chains were considered. The following 270-chain ~22000-atom models (see Sec 3.3) were studied at 400 K: dimethyl PEO+silica, dihydroxyl PEO+silica, an equimolecular mixture of both types of PEO+silica as well as the three corresponding pure PEO melts. It should be noted that the end-group effect in pure PEO was studied by connectivity-altering MC simulations around the same time by Wick et al, using a transferable potential for phase equilibria united-atom force-field.[62]

7.1. Densities and energetic properties

The densities of all pure melts fall within the 1000-1050 kg m^{-3} range, in very good agreement with experiment[322,323] and other simulations.[62] Inserting a nanoparticle in a melt leads to a systematic increase in the total density by ~8.5-9%. However only a specific region is affected as can be seen in Fig. 53, with the radial mass densities $\rho(R)$ of both the polymer chains and the silica being plotted as a function of the distance R from the center-of-mass (COM) of the nanoparticle:

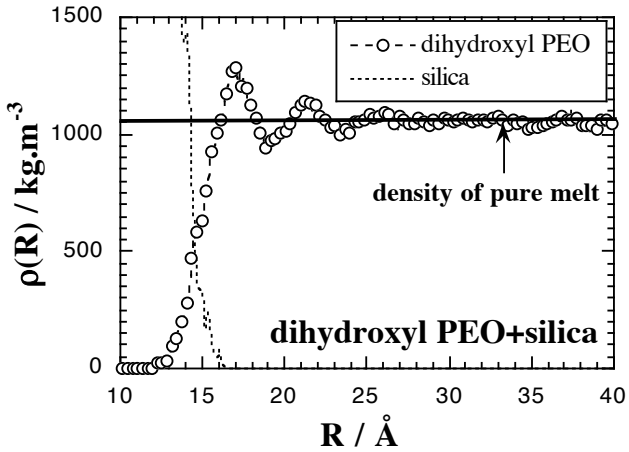

***Fig. 53**: Radial mass densities in slabs of width 0.1 Å as a function of the distance R from the silica COM in the dihydroxyl PEO+silica system.*[22]

As in the case of the free-standing planar interface (Sec. 5.3.), it is not straightforward to define the nanoparticle radius. However, it is possible to estimate the volume not occupied by silica using repeated trial insertions of the smallest probe size that cannot be inserted into pure

SiO_2. This leads to an average radius of ~15.2 Å, which is consistent with Fig. 53. Another way to estimate the radius is to associate it with the separation at half-maximum of the first peak in the pair distribution function,[141] but this is only realistic when the peaks are much sharper.

The PEO molecules close to the spherical interface are arranged in three densely packed shells and, at larger distances, the mass density eventually tends towards the pure melt value. Layering is well-known in these systems and is directly related to the nature of polymer-surface interactions, *i.e.* well-defined for strongly attractive systems and much less-defined at rough interfaces with weaker polymer-surface interactions.[133,134,137,139,141-144,271,324] The higher mass-densities are found for those oligomers which are at the immediate vicinity of the particle, and some parts of the flexible PEO can even access the rough regions of the silica coverage. As seen in Fig. 53, the structural influence of the nanoparticle spans an approximate range of ~15 Å. The main difference between both types of PEO end-groups is a small shoulder at low R for dihydroxyl PEO (visible at larger resolutions), which will be later characterized with radial distribution functions.

The average intermolecular energies for PEO-silica interactions can be found in Table IX, resolved into their van der Waals (LJ) and their electrostatic (coul) components:

Table IX *The total, Lennard-Jones and coulombic intermolecular PEO-silica potential energies are in kJ per mole of PEO monomer (±0.03 kJ mol^{-1} mon^{-1}). The estimated changes in enthalpy ΔH_{mixing} are also in kJ mol^{-1} mon^{-1}.*

Polymer	**dimethyl PEO**	**dihydroxyl PEO**	**equimolar mixture**
$\left\langle U_{pot}^{inter} \right\rangle$	-2.04	-2.41	-2.23
$\left\langle U_{LJ}^{inter} \right\rangle$	-1.75	-1.86	-1.79
$\left\langle U_{coul}^{inter} \right\rangle$	-0.29	-0.55	-0.44
ΔH_{mixing}	-1.56	-1.90	-1.69

While the silica-silica energy is almost totally electrostatic and remains unchanged, the PEO-PEO energy is found to slightly decrease when inserting the nanoparticle. This is compensated for by the added PEO-silica attractions (Table IX), which originate from ~80% van der Waals and ~20% electrostatic interactions. However, the hydroxyl end-groups added electrostatic interactions are almost doubled with respect to the dimethyl counterparts, thus suggesting as experimentally[145-148] the existence of specific features for this end-group at the immediate interface. The equimolar system always displays an intermediate behaviour.

The change in enthalpy associated with mixing PEO and silica, ΔH_{mixing}, could be estimated by $\Delta U_{PEO\text{-}silica}$ minus the sum of $\Delta U_{pure\text{-}PEO}$ and $\Delta U_{nanoparticle}$, the $P\Delta V$ term being negligible (Table IX). The mixing enthalpy of 9-*mers* PEO with silica has been reported from microcalorimetry measurements as being around -1.5 to -1.8 kJ mol^{-1} mon^{-1},[145] which provides some verification of the parameters used here for the PEO-silica interactions.

7.2. Chain structures

Neither the end-groups nor the presence of the nanoparticle have a large effect on the *average* conformational and configurational properties of the PEO oligomers. The fact that the overall chain dimensions are almost independent of the presence of the nanoparticle has already been noted,[133-135,138,139,141,143] and the structural effect of the monomers close to the surface is thought to be overwhelmed by the rest of the melt.[139] On the other hand, chain structures are expected to be at least distorted close to the interface, and partly dependent on the end-groups.[145-148]

As before,[4,6,7,9,14,89,196] the PEO backbone torsions are consistent with the *gauche* effect,[89,196] albeit with minor adjustments in the first density layer, thus indicating that effective surface coverage is not only related to end-groups. The methyl end-torsions C-O-C-CH_3 are mostly *trans* in the melt, but tend to adopt more *gauche* conformations in the immediate vicinity of the filler for steric reasons. On the other hand, the successive O-C-C-OH and C-C-O-H end-torsions of dihydroxyl PEO are always found in approximately equal proportions either in $gauche^+gauche^-$ or in $gauche^-gauche^+$ states. This feature is independent

of the presence of the nanoparticle and is related to a strongly favoured intramolecular 1···5 interaction between the hydroxyl H and the first backbone O ether in dihydroxyl PEO. It has been identified elsewhere as the main cause for the end-capping effect on pure PEO volumetric properties.[62]

Figure 54a displays a radial dependence curve of $<S^2>$ as a function of the distance R to the silica COM. It suggests that only right at the interface itself is there a strong effect on chain configurations with a tendency towards elongation. In addition, the variation of the perpendicular component, $<S_\perp^2>$, shows that the chains are "flattened" against the nanoparticle surface for a range corresponding to at least the width of the first layer (Fig. 54a):

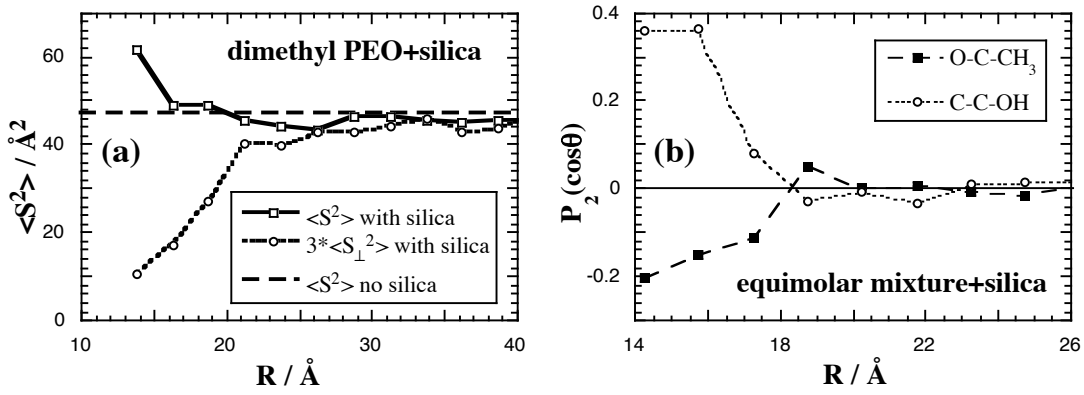

Fig. 54 *(a) Mean-square radius of gyration $<S^2>$ (squares) and its component perpendicular to the surface of the nanoparticle (circles) as a function of R along with the pure dimethyl PEO melt (line). The slab width is 2.5 Å. (b) P_2 Legendre functions for the end-groups in the equimolecular mixture of both PEO+silica system with a resolution of 1.5 Å.*[22]

These structural variations are confirmed by the P_2 Legendre functions (Eq. 32), which display a clear correspondence between backbone angles and the PEO layers found in the mass density curve. The angle are aligned randomly in trough regions of $\rho(R)$, while they tend towards a parallel alignement with respect to the silica surface in high-density regions, which obviously favours packing.[114,133,143,271] Fig. 54b compares methyl-terminated and hydroxyl-terminated angles. The former tend toward parallel alignments with respect to the silica

surface whereas the latter are more perpendicular to the surface. The model thus appears to reproduce the experimental hypothesis that hydroxyl end-groups allow the PEO molecules to partially "stand up" with respect to the silica surface.[114,133,143]

Specific structural features with respect to the silica COM can be analyzed using $g_{COM...z}(R)$ radial distribution functions between the COM and a given atom type z (Fig. 55a):

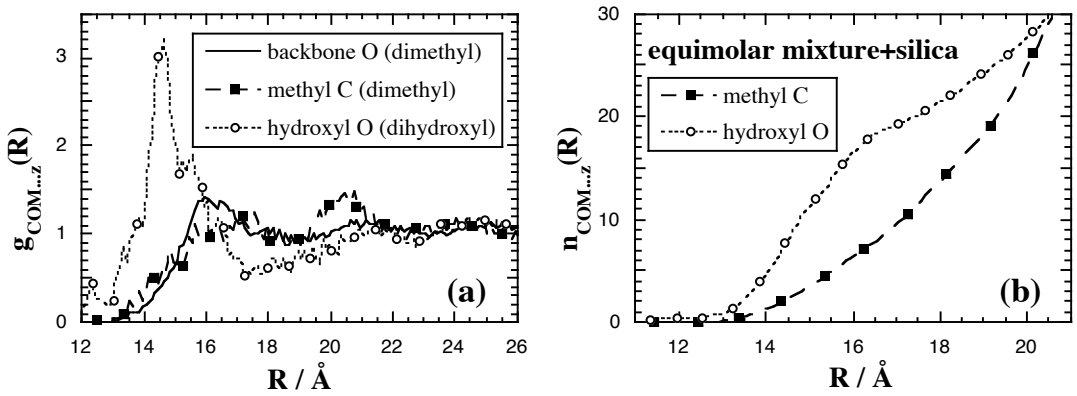

Fig. 55 *(a) Radial distribution functions for both two types of end-groups and PEO backbone oxygens with respect to the silica COM. (b) Average number of end-group atoms found at a distance R from the silica COM in the equimolar mixture.*[22]

The backbone $g_{COM...z}(R)$ correspond almost exactly to the PEO layers, *i.e* their maxima and minima fall in the high- and low-density regions, respectively. The methyl carbons $g_{COM...z}(R)$ are hardly differentiated, which suggests that there is little specific affinity for this end-group on the silica surface. On the contrary, the hydroxyl oxygens $g_{COM...z}(R)$ exhibit a very strong peak associated to the small mass density shoulder. Upon integration of the $g_{COM...z}(R)$ curves, Figure 55b reveals that there are far more hydroxyl than methyl end-groups in the vicinity of the nanoparticle in the equimolar PEO mixture+silica system, with the closer to the particle surface, the more pronounced the relative increased affinity for hydroxyl end-groups.

The $g(r)$ functions can also be calculated for selected pairs of PEO *vs* nanoparticle atom types. As expected, the closest peaks in the $g(r)$ functions are found for interactions between PEO atoms and silanol hydrogens or oxygens. They are shown in Fig. 56a for dimethyl PEO+silica and in Fig. 56b for dihydroxyl PEO+silica:

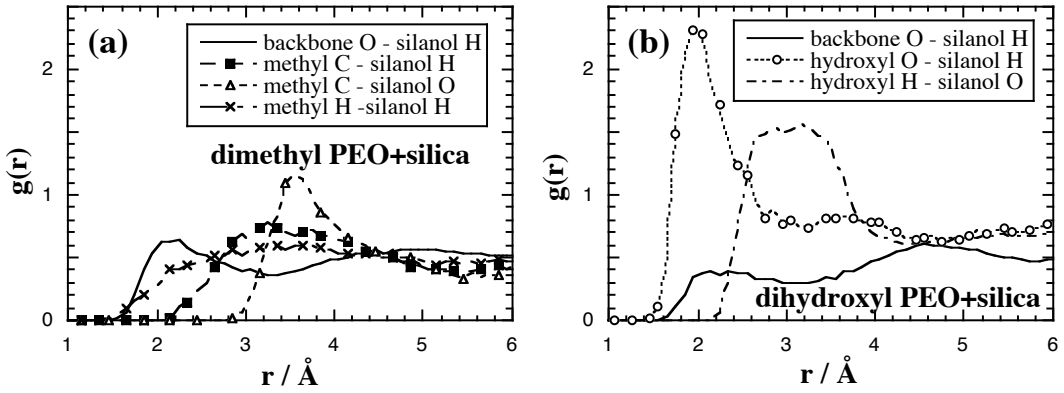

Fig. 56 *Radial distributions functions between silica and PEO atoms as a function of their distances r. (a) shows the main structures at the dimethyl PEO-silica interface and (b) the same at the dihydroxyl PEO-silica interface.*[22]

Figure 56a displays the limited structuring of methyl-terminated PEO at the interface. The nearest interactions are those of backbone oxygens with the silanol hydrogens which correspond to hydrogen bonding. For steric reasons, the -CH_3 groups will not get as deep into the surface, although the small H are able to come in fairly close contact to the silanol hydrogens. This is explained by the only major peak found in these systems representing preferential interactions between the negatively-charged silanol oxygens and the positively-charged methyl carbon. In SFG vibrational spectroscopy experiments, it was concluded that either the chains have a random structure or the CH_2 and CH_3 groups lie down at the interface.[151] Our simulations would suggest the latter as being more probable, although the actual structuring remains fairly weak.

On the other hand, hydroxyl-terminated PEO at the interface is far more structured (Figure 56b). It is clear that the main interactions involve the hydroxyl oxygens with the silanol hydrogens, thus confirming their major role at the PEO-silica interface.[308,312,325] Backbone O play much less of a role in the total hydrogen-bonding capability and the trough of the hydroxyl O-silanol H radial distribution function (2.8 Å) can be considered as the upper limit for the formation of hydrogen bonds. Another interesting feature is that the peak related to the interactions between the hydroxyl H and silanol O is smoother and found at larger distances. These atoms are thus prevented from forming hydrogen bonds by the more

attractive hydroxyl O-silanol H interactions. This results in the hydroxyl H being pushed away from the surface with respect to the hydroxyl O.

The underlying H-bonding dynamics are found to be very complicated with many different silanol H visited, and in several cases, temporary multiplicity (Table X):

Table X *Percentages of average residence times for hydrogen-bonding "complexes" formed by hydroxyl O and silanol H at the interface*

	silanol H involved in		**hydroxyl O involved in**			
t / ps	**1 H-bond**	**2 H-bonds**	**1 H-bond**	**2 H-bonds**	**3 H-bonds**	**4 H-bonds**
< 5	58	89	66	75	82	100
[5,10[	18	7	17	16	13	-
[10,15[	9	3	7	4	2	-
[15,20[	5	-	4	2	3	-
[20,25[	3	1	2	1	-	-
[25,30[	2	-	1	1	-	-
> 30	5	-	3	1	-	-

The most stable complexes are those where a single silanol H and a single hydroxyl O are bonded together. As soon as the multiplicity increases, steric repulsions become important and complexes are very short-lived, *i.e.* < 5 ps for most of them, although they are able to reform fairly fast. As can be expected, the simultaneous coordination between a hydroxyl O and three or four silanol H often involves geminal $=Si(OH)_2$ groups on the silica surface. However, they can also occur with single bonded ≡SiOH groups, thus suggesting that those interactions are more dependent on where the silanol H are situated rather than on which surface silicon they are bonded to. The molecules are able to form loops, as both -OH ends of a PEO oligomer can be found in the coordination sphere of the same silanol H, albeit very rarely at the same time. The main structural peak displayed in Figure 56b is thus underlined by strong dynamical changes. The overall picture that emerges is summarized in Fig. 57:

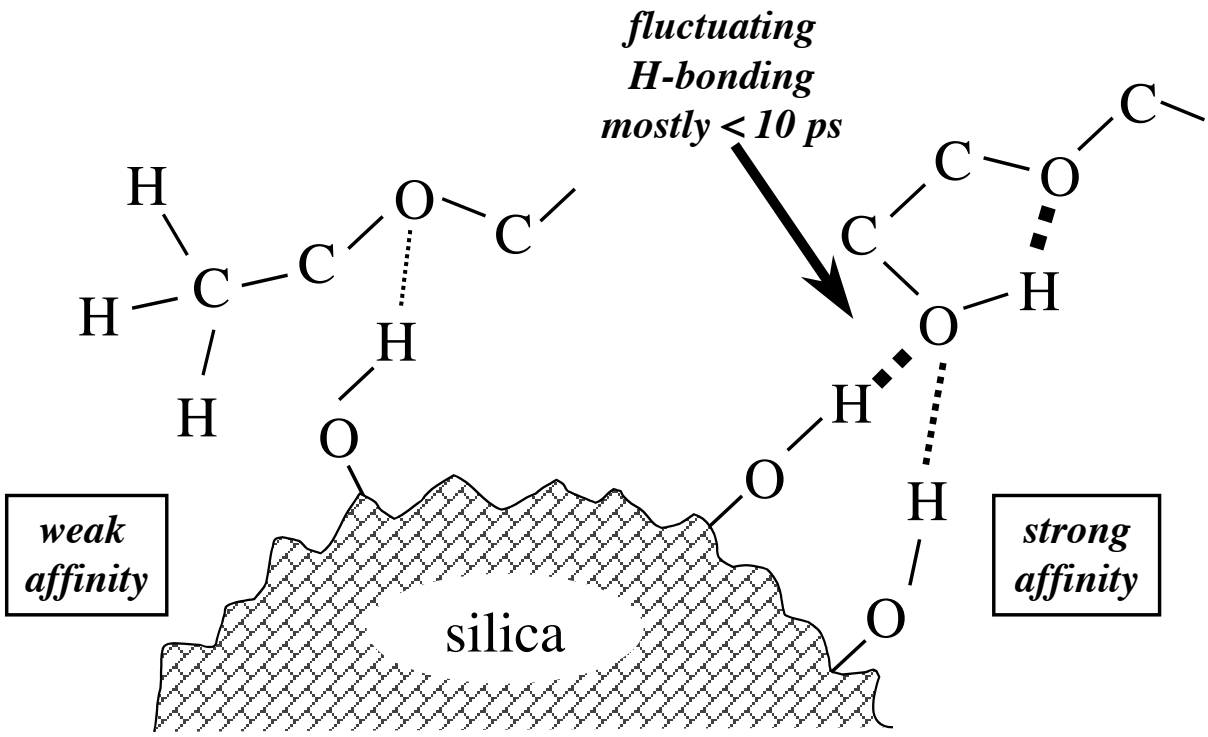

Fig. 57 *A schematic representation of the atomic interactions at a PEO-silica interface.*

7.3. Chain dynamics

Like most other simulations,[133,134,138,139,141,143,324] the chain MSDs are affected by the filler and the dynamics generally slowed down by ~20%. This also agrees with experiment, where the relaxation dynamics of PEO were found to be slower in the presence of silica nanoparticles.[326]

The MSDs can be calculated as a function of *R* for a given time-interval in order to characterize the actual effect of the interface on the translational dynamics (Fig. 58a). For all species concerned, the mobility is obviously quite reduced at the interface, which is typical of strongly adsorbed chains.[143,271,327] The methyl end-groups always seem to be more mobile than the hydroxyl[62] which, despite the dynamic exchanges in the hydrogen-bonding sphere noted above, have a tendency to remain in the immediate vicinity of the filler. The rare backbone O moieties which come within this sphere of influence are also immobilized by the silica nanoparticle through hydrogen bonds (Fig. 58a):

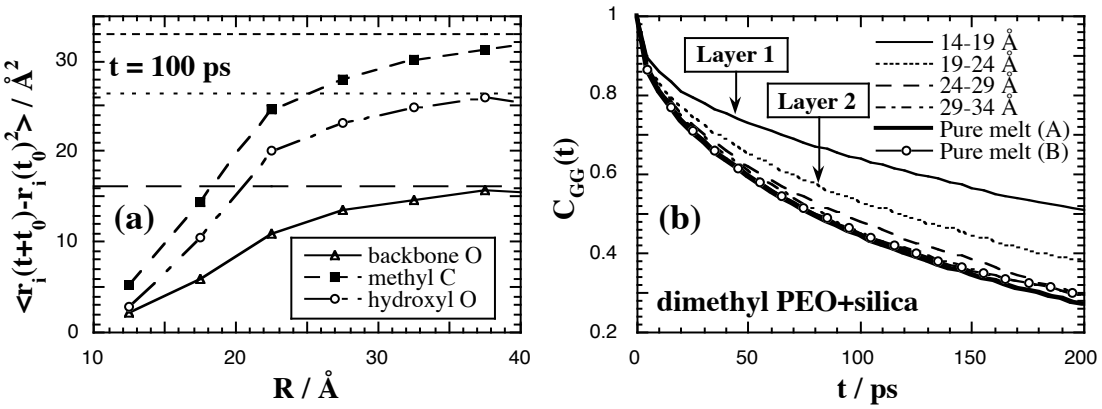

Fig. 58 *(a) Typical MSDs as a function of R over 100 ps. The slab width is 5 Å and the pure melt values are indicated by straight lines. (b) $C_{GG}(t)$ functions for four zones situated at different distances from the silica COM in the dimethyl PEO+silica system. The same function for the pure melt has been obtained in two different ways:- (A) using the indiscriminate averaging of all angles and (B) averaging only over angles which remain in the same spherical layers of thickness 5 Å.*[22]

To try and evaluate the possible effects of the presence of the nanoparticle on the dynamics of backbone torsional modes, correlation functions, $C_{TT}(t)$ (Eq. 9) for C-C-O-C and $C_{GG}(t)$ (Eq. 15) for O-C-C-O torsions were calculated and found to fit well to the stretched exponential (Kohlrausch-Williams-Watts) functional form for $C_{AA}(t)$ (AA = either TT or GG):

$$C_{AA}(t) = exp\left(-\left(\frac{t}{\alpha}\right)^{\beta}\right) \tag{37}$$

Best fit values for α and β were obtained using non-linear least squares regression and the associated relaxation times from the analytic time integral of the stretched exponential :

$$\tau_{AA} = \int_0^{\infty} \exp\left(-\left(\frac{t}{\alpha}\right)^{\beta}\right) dt = \frac{\alpha}{\beta}\,\Gamma\left(\frac{1}{\beta}\right) \tag{38}$$

where the Γ function was estimated using a standard numerical technique.[328] All C-O-C-C τ_{TT} fall in the range ~10-25 ps and the O-C-C-O τ_{GG} in the range ~170-320 ps, but they increase when the silica nanoparticle is added and when -CH_3 end groups are replaced by -OH.

The relaxation functions were also calculated as a function of R,[143,324] by identifying those angles in radial shells of 5 Å thickness. As expected, angles closer to the nanoparticle

remained noticeably longer in the same layer than those further away. Fig. 58b shows dimethyl PEO O-C-C-O $C_{GG}(t)$ functions for four different regions around the silica COM compared to the bulk data. Conformational relaxation is significantly slowed down in the first layer. Indeed, the τ_{GG} relaxation time of the first layer (~1000 ps) is at least four times longer than the value of ~230 ps for the pure melt. The second layer is also clearly affected but certainly to a lesser extent than the first, τ_{GG} ~250 ps. Considering the regions between 24 and 34 Å, it can be said that there is a systematic tendency for a slight slowing down also. Beyond that distance though, the conformational relaxation is indistinguishable from the limiting results for the pure melt.

As seen in the case of the planar interfaces (Sec 5.3.1.3), the dynamic effect of the silica on the flexible PEO oligomers displayed in Figure 58 spans a larger distance than the actual structural changes. It eventually returns to the pure melts values around 30 Å from the interface, thus showing that the dynamical sphere of influence is about twice as large as the structural one.

7.4. Perspectives

This study is well representative of the current possibilities and difficulties encountered when applying fully-atomistic molecular dynamics simulations to oligomer-nanoparticle systems. Although the preparation procedure is complex and time-consuming, a lot of information can be obtained in order to complement experimental evidence.

In a related project,[329] we have tried to complete this study by adding water to the PEO and PEO-silica systems, since it is known to compete with PEO for the silanols.[151,325] However, at the temperature under study (400 K), water and PEO were found to phase-separate in the models. While this is actually a known experimental phenomenon in PEO solutions over 350 K,[330] we did not anticipate that the PEO+water+silica models would react accordingly so rapidly. These simulations could be carried out at lower temperatures, but the decorrelation procedure will obviously require a lot longer than a few nanoseconds.

Even though only one chain length has been studied here, previous results for chain melts at planar interfaces[114] suggest strongly that the range of influence of the nanoparticle will not change significantly if longer chains were used. It should be possible to carry out these simulations using slightly longer PEO chains, but once again relaxation times increase rapidly with chain length rendering the attainment of equilibrium for significantly longer chains rather costly in terms of CPU time. Further analyses could also relate to the dynamic equilibria of PEO adsorption and desorption at the surface, such as what was reported recently in the case of coarse-grained bead-spring models.[271]

8. CONCLUSIONS

The present manuscript describes a series of fully-atomistic simulations carried out over the last ten years, which involve polymer-based materials and the transport of small selected species. Most of these projects can be strengthened by following some of the aforementioned suggestions. Indeed, with respect to the mid-nineties, the constant increase in computing power and the development of new methodologies has already led to significant steps forward in the size and complexity of problems that can now be studied. This is of course especially relevant to the case of glassy polymers.

One such example is water-transport, which is currently under study for long-chain polyimides (Kapton®) and polysulfones in order to be directly confronted to experimental evidence.[300] These simulations will naturally be carried out on a much longer timescale than the work reported in Sec. 6. Another fascinating penetrant is CO_2 which exhibits particularly high solubilities in polymers and is thought to affect both chain structures and dynamics. It can even lubricate motions of the matrix and thus lead to the "plasticization phenomenon".[331] A recent paper has shown using Monte Carlo simulations that the carbonyl oxygen in carbonate polyethers is the main reason for the increased CO_2-philicity of these macrolecules.[332] In the same vein, *ab initio* molecular orbital calculations of CO_2 and fluorinated compounds have suggested that there is an important quadrupole-dipole interaction between the gas and accessible fluorine sites.[333] Following CO_2 sorption/diffusion in dense bulk or membrane models of fluorinated polyimides would certainly bring out much information on the capacity of these molecules to act as gas-separation membranes. Indeed, the situation is quite complicated since the direct correlation between free-volume and the CO_2 diffusion coefficient, which is often encountered, is not obeyed for all polyimides.[334-336] In addition, the performances are known to be strongly affected by the chemical nature of the diamine, such as, for example, the presence of polar groups,[337] branching,[338] and even the meta- or para-connection with respect to the dianhydride.[339-341]

Finally, we are well-aware of the possibilities offered by multiscale simulations, which are themselves constantly evolving.[67,68,342-344] Recent simulations, which were used to study the entanglement length of bisphenol-A-polycarbonate (BPA-PC), allowed the effective timescale which can be reached by simulation to be extended by several orders of magnitude, thus reaching well into the experimentally accessible regime.[345] In addition, chemical details were reintroduced by inverse-mapping of their coarse-grained BPA-PC models in order to obtain both well-equilibrated atomistically-detailed melts and realistic long-time trajectories.[346] We are very interested by the possibilities to extend these approaches to our polyimide matrices.

REFERENCES

(1) Allen, M. P.; Tildesley, D. J. *Computer Simulation of Liquids*; Clarendon Press: Oxford, England, 1987.
(2) Frenkel, D.; Klein, M.; Parrinello, M.; Smit, B. *Understanding Molecular Simulation*, 2nd ed.; Academic Press: San Diego, CA and London, 2002.
(3) Neyertz, S.; Brown, D.; Thomas, J. O. *J. Chem. Phys.* **1994**, *101*, 10064-10073.
(4) Neyertz, S.; Brown, D. *J. Chem. Phys.* **1995**, *102*, 9725-9735.
(5) Neyertz, S.; Brown, D.; Thomas, J. O. *Electrochimica Acta* **1995**, *40*, 2063-2069.
(6) Neyertz, S.; Brown, D.; Thomas, J. O. *Computational Polym. Sci.* **1995**, *5*, 107-120.
(7) Neyertz, S.; Ph-D Thesis, University of Uppsala, 1995.
(8) Brown, D.; Neyertz, S. *Mol. Phys.* **1995**, *84*, 577-595.
(9) Neyertz, S.; Brown, D. *J. Chem. Phys.* **1996**, *104*, 3797-3809.
(10) Neyertz, S.; Brown, D. *J. Chem. Phys.* **1996**, *104*, 10063.
(11) Neyertz, S.; Brown, D.; Clarke, J. H. R. *J. Chem. Phys.* **1996**, *105*, 2076-2088.
(12) Neyertz, S.; Brown, D. *Electrochimica Acta* **1998**, *43*, 1343-1347.
(13) Neyertz, S.; Pizzi, A.; Merlin, A.; Maigret, B.; Brown, D.; Deglise, X. *J. Applied Polym. Sci.* **2000**, *78*, 1939-1946.
(14) Neyertz, S.; Brown, D.; Colombini, D.; Albérola, N. D.; Merle, G. *Macromolecules* **2000**, *33*, 1361-1369.
(15) Neyertz, S.; Brown, D. *J. Chem. Phys.* **2001**, *115*, 708-717.
(16) Neyertz, S.; Douanne, A.; Bas, C.; Albérola, N. D. *Polyimides and High Performance Polymers* **2001**, 133-140.
(17) Pinel, E.; Brown, D.; Bas, C.; Mercier, R.; Albérola, N. D.; Neyertz, S. *Macromolecules* **2002**, *35*, 10198-10209.
(18) Neyertz, S.; Brown, D.; Douanne, A.; Bas, C.; Albérola, N. D. *J. Phys. Chem. B.* **2002**, *106*, 4617-4631.
(19) Vouyovitch, L.; Brown, D.; Neyertz, S.; Gallot, B. *Soft Materials* **2002**, *1*, 93-113.
(20) Pinel, E.; Brown, D.; Bas, C.; Mercier, R.; Sanchez, J.; Neyertz, S. *Polyimides and High Performance Polymers* **2003**, 107-116.
(21) Neyertz, S.; Brown, D. *Macromolecules* **2004**, *37*, 10109-10122.
(22) Barbier, D.; Brown, D.; Grillet, A.-C.; Neyertz, S. *Macromolecules* **2004**, *37*, 4695-4710.
(23) Queyroy, S.; Neyertz, S.; Brown, D.; Müller-Plathe, F. *Macromolecules* **2004**, *37*, 7338-7350.
(24) Neyertz, S.; Douanne, A.; Brown, D. *Macromolecules* **2005**, *38*, 10286-10298.
(25) Neyertz, S.; Douanne, A.; Brown, D. *J. Memb. Sci.* **2006**, *in press*.
(26) Armand, M. B.; Chabagno, J. M.; Duclot, M. J. In *Fast Ion Transport in Solids*; Vashishta, P.; Mundy, J. N.; Shenoy, G. K., Eds.; North-Holland: New York, 1979; p 131.
(27) Neyertz, S.; Chabé, J.; Gébel, G.; Brown, D. *in preparation*
(28) Kreuer, K.-D.; Paddison, S. J.; Spohr, E.; Schuster, M. *Chem. Rev.* **2004**, *104*, 4637-4678.
(29) Ohya, H.; Kudryavtsev, V. V.; Semenova, S. I. *Polyimide membranes - Applications, Fabrication and Properties*; copublished by Kodansha Ltd and Gordon and Breach Science Publishers S.A.: Tokyo and Amsterdam, 1996.
(30) Hammonds, K. D.; Ryckaert, J.-P. *Comput. Phys. Comm.* **1991**, *62*, 336-351.
(31) Matsuura, H.; Fukuhara, K. *J. Polym. Sci. Part B : Polym. Phys.* **1986**, *24*, 1383.

(32) Rappé, A. K.; Casewit, C. J.; Colwell, K. S.; Goddard, W. A., III; Skiff, W. M. *J. Am. Chem. Soc.* **1992**, *114*, 10024-10035.
(33) Ewald, P. P. *Ann. Phys.* **1921**, *64*, 253-287.
(34) Smith, W. *Comput. Phys. Comm.* **1992**, *67*, 392.
(35) Sagui, C.; Darden, T. *J. Chem. Phys.* **2001**, *114*, 6578-6591.
(36) Beckers, J. V. L.; Lowe, C. P.; de Leeuw, S. W. *Mol. Sim.* **1998**, *20*, 369-383.
(37) Brandt, A. *Math. Comput.* **1977**, *31*, 333-390.
(38) Frisch, M. J.; Trucks, G. W.; Schlegel, H. B.; Scuseria, G. E.; Robb, M. A.; Cheeseman, J. R.; Zakrzewski, V. G.; Montgomery Jr., J. A.; Stratmann, R. E.; Burant, J. C.; Dapprich, S.; Millam, J. M.; Daniels, A. D.; Kudin, K. N.; Strain, M. C.; Farkas, O.; Tomasi, J.; Barone, V.; Cossi, M.; Cammi, R.; Mennucci, B.; Pomelli, C.; C. Adamo; Clifford, S.; Ochterski, J.; Petersson, G. A.; Ayala, P. Y.; Cui, Q.; Morokuma, K.; Malick, D. K.; Rabuck, A. D.; Raghavachari, K.; Foresman, J. B.; Cioslowski, J.; Ortiz, J. V.; Baboul, A. G.; Stefanov, B. B.; Liu, G.; Liashenko, A.; Piskorz, P.; Komaromi, I.; Gomperts, R.; Martin, R. L.; Fox, D. J.; Keith, T.; Al-Laham, M. A.; Peng, C. Y.; Nanayakkara, A.; Gonzalez, C.; Challacombe, M.; Gill, P. M. W.; Johnson, B.; Chen, W.; Wong, M. W.; Andres, J. L.; Gonzalez, C.; Head-Gordon, M.; Replogle, E. S.; Pople, J. A. *Gaussian 98; Gaussian Inc.; Pittsburgh, PA, 1998.* **1998**.
(39) Singh, U. C.; Kollman, P. A. *J. Comput. Chem.* **1984**, *5*, 129.
(40) Brown, D. *The gmq User Manual Version 3: available at http://www.lmops.univ-savoie.fr/brown/gmq.html* **1999**.
(41) Brown, D.; Maigret, B. *Speedup* **1999**, *12*, 33-40.
(42) Humphrey, W.; Dalke, A.; Schulten, K. "*VMD - Visual Molecular Dynamics*" *J. Molec. Graphics* **1996**, *14*, 33-38.
(43) Ferry, J. D. *Viscoelastic Properties of Polymers*, 3rd ed.; Wiley: New York, 1980.
(44) Theodorou, D. N.; Suter, U. W. *Macromolecules* **1985**, *18*, 1467-1478.
(45) Boyd, R. H.; Pant, P. V. K. *Macromolecules* **1991**, *24*, 6325.
(46) Greenfield, M. L.; Theodorou, D. N. *Macromolecules* **2001**, *34*, 8541-8553.
(47) Pant, P. V. K.; Theodorou, D. N. *Macromolecules* **1995**, *28*, 7224-7234.
(48) Harmandaris, V. A.; Mavrantzas, V. G.; Theodorou, D. N. *Macromolecules* **1998**, *31*, 7934-7943.
(49) Mavrantzas, V. G.; Boone, T. D.; Zervopoulou, E.; Theodorou, D. N. *Macromolecules* **1999**, *32*, 5072-5096.
(50) Harmandaris, V. A.; Mavrantzas, V. G.; Theodorou, D. N. *Macromolecules* **2000**, *33*, 8062-8076.
(51) Mavrantzas, V. G.; Theodorou, D. N. *Macromol. Theory Sim.* **2000**, *9*, 500-515.
(52) Faller, R.; Müller-Plathe, F.; Doxastakis, M.; Theodorou, D. *Macromolecules* **2001**, *34*, 1436-1448.
(53) Doxastakis, M.; Mavrantzas, V. G.; Theodorou, D. N. *J. Chem. Phys.* **2001**, *115*, 11339-11351.
(54) Doxastakis, M.; Mavrantzas, V. G.; Theodorou, D. N. *J. Chem. Phys.* **2001**, *115*, 11352-11361.
(55) Uhlherr, A.; Mavrantzas, V. G.; Doxastakis, M.; Theodorou, D. N. *Macromolecules* **2001**, *34*, 8554-8568.
(56) Zervopoulo, E.; Mavrantzas, V. G.; Theodorou, D. N. *J. Chem. Phys.* **2001**, *115*, 2860-2875.
(57) Karayiannis, N. C.; Giannousaki, A. E.; Mavrantzas, V. G.; Theodorou, D. N. *J. Chem. Phys.* **2002**, *117*, 5465-5479.

(58) Harmandaris, V. A.; Mavrantzas, V. G.; Theodorou, D. N.; Kröger, M.; Ramirez, J.; Öttinger, H. C.; Vlassopoulos, D. *Macromolecules* **2003**, *36*, 1376-1387.
(59) Karayiannis, N. C.; Giannousaki, A. E.; Mavrantzas, V. G. *J. Chem. Phys.* **2003**, *118*, 2451-2454.
(60) Doxastakis, M.; Theodorou, D. N.; Fytas, G.; Kremer, F.; Faller, R.; Muller, P. F.; Hadjichristidis, N. *J. Chem. Phys.* **2003**, *119*, 6883-6894.
(61) Gestoso, P.; Nicol, E.; Doxastakis, M.; Theodorou, D. N. *Macromolecules* **2003**, *36*, 6925-6938.
(62) Wick, C. D.; Theodorou, D. N. *Macromolecules* **2004**, *37*, 7026-7033.
(63) Tsolou, G.; Mavrantzas, V. G.; Theodorou, D. N. *Macromolecules* **2005**, *38*, 1478-1492.
(64) Peristeras, L. D.; Economou, I. G.; Theodorou, D. N. *Macromolecules* **2005**, *38*, 386-397.
(65) Sok, R. M.; Berendsen, H. J. C.; van Gunsteren, W. F. *J. Chem. Phys.* **1992**, *96*, 4699.
(66) Kotelyanskii, M. J.; Wagner, N. J.; Paulaitis, M. E. *Macromolecules* **1996**, *29*, 8497-8506.
(67) Kremer, K.; Müller-Plathe, F. *Mol. Sim.* **2002**, *28*, 729-750.
(68) Müller-Plathe, F. *ChemPhysChem* **2002**, *3*, 754-769.
(69) Brown, D.; Clarke, J. H. R.; Okuda, M.; Yamazaki, T. *J. Chem. Phys.* **1994**, *100*, 1684-1692.
(70) Brown, D.; Clarke, J. H. R.; Okuda, M.; Yamazaki, T. *J. Chem. Phys.* **1994**, *100*, 6011-6018.
(71) Brown, D.; Clarke, J. H. R.; Okuda, M.; Yamazaki, T. *J. Chem. Phys.* **1996**, *104*, 2078-2082.
(72) Smith, G. D.; Yoon, D. Y.; Jaffe, R. L. *Macromolecules* **1993**, *26*, 5213.
(73) Rapold, R. F.; Suter, U. W. *Macromol. Theory Sim.* **1994**, *3*, 1-17.
(74) Flory, P. J. *The Statistical Mechanics of Chain Molecules*; Hanser Publishers: New York, 1988.
(75) Lal, M. *Mol. Phys.* **1969**, *17*, 57-64.
(76) Baschnagel, J.; Qin, K.; Paul, W.; Binder, K. *Macromolecules* **1992**, *25*, 3117-3124.
(77) Almarza, N. G.; Enciso, J.; Alonso, J.; Bermejo, F. J. *Mol. Phys.* **1990**, *70*, 485-504.
(78) Marceau, S.; Ph-D Thesis, University of Savoie, 2003.
(79) Queyroy, S.; Ph-D Thesis, University of Savoie, 2004.
(80) Metropolis, N.; Rosenbluth, A. W.; Rosenbluth, M. N.; Teller, A. H.; Teller, E. *J. Chem. Phys.* **1953**, *21*, 1087-1092.
(81) Hofmann, D.; Heuchel, M.; Yampolskii, Y.; Khotimskii, V.; Shantarovich, V. *Macromolecules* **2002**, *35*, 2129-2140.
(82) Fincham, D. *Mol. Sim.* **1994**, *13*, 1-19.
(83) Berendsen, H. J. C.; Postma, J. P. M.; van Gunsteren, W. F.; DiNola, A.; Haak, J. R. *J. Chem. Phys.* **1984**, *81*, 3684-3690.
(84) Auhl, R.; Everaers, R.; Grest, G. S.; Kremer, K.; Plimpton, S. J. *J. Chem. Phys.* **2003**, *119*, 12718-12728.
(85) Brown, D.; Clarke, J. H. R. *Comput. Phys. Comm.* **1991**, *62*, 360-369.
(86) Brown, D.; Clarke, J. H. R. *J. Chem. Phys.* **1990**, *93*, 4117-4122.
(87) Brown, D.; Clarke, J. H. R. *J. Chem. Phys.* **1990**, *94*, 4684.
(88) Smith, G. D.; Yoon, D. Y.; Jaffe, R. L.; Colby, R. H.; Krishnamoorti, R.; Fetters, L. J. *Macromolecules* **1996**, *29*, 3462-3469.
(89) Müller-Plathe, F. *Acta Polym.* **1994**, *45*, 259-293.

(90) Hofmann, D.; Fritz, L.; Ulbrich, J.; Paul, D. *Comp. Theor. Polym. Sci.* **2000**, *10*, 419-436.
(91) Hofmann, D.; Fritz, L.; Ulbrich, J.; Schepers, C.; Böhning, M. *Macromol. Theory Sim.* **2000**, *9*, 293-327.
(92) Hofmann, D.; Ulbrich, J.; Fritsch, D.; Paul, D. *Polymer* **1996**, *37*, 4773-4785.
(93) Hofmann, D.; Fritz, L.; Ulbrich, J.; Paul, D. *Polymer* **1997**, *38*, 6145-6155.
(94) Heuchel, M.; Hofmann, D. *Desalination* **2002**, *144*, 67-72.
(95) Heuchel, M.; Hofmann, D.; Pullumbi, P. *Macromolecules* **2004**, *37*, 201-214.
(96) Pandey, P.; Chauhan, R. S. *Prog. Polym. Sci.* **2001**, *26*, 853-893.
(97) Eastmond, G. C.; Page, P. C. B.; Paprotny, J.; Richards, R. E.; Shaunak, R. *Polymer* **1993**, *34*, 667-670.
(98) Joly, C.; Le Cerf, D.; Chappey, C.; Langevin, D.; Muller, G. *Sep. Purif. Tech.* **1999**, *16*, 47-54.
(99) Kawakami, H.; Mikawa, M.; Nagaoka, S. *J. Memb. Sci.* **1996**, *118*, 223-230.
(100) O'Brien, K. C.; Koros, W. J.; Husk, G. R. *Polym. Eng. Sci.* **1987**, *27*, 211-217.
(101) Natarajan, U.; Mattice, W. L. *J. Memb. Sci.* **1998**, *146*, 135-142.
(102) Clancy, T. C.; Mattice, W. L. *Comp. Theor. Polym. Sci.* **1999**, *9*, 261-270.
(103) Chang, J.; Han, J.; Yang, L.; Jaffe, R. L.; Yoon, D. Y. *J. Chem. Phys.* **2001**, *115*, 2831-2840.
(104) Doruker, P.; Mattice, W. L. *Macromolecules* **1998**, *31*, 1418-1426.
(105) Ayyagari, C.; Bedrov, D. *Polymer* **2004**, *45*, 4549-4558.
(106) Kikuchi, H.; Kuwajima, S.; Fukuda, M. *J. Chem. Phys.* **2001**, *115*, 6258-6265.
(107) Kikuchi, H.; Kuwajima, S.; Fukuda, M. *Chem. Phys. Lett.* **2002**, *358*, 466-472.
(108) Pinel, E.; Ph-D Thesis, University of Savoie, 2001.
(109) Pinel, E.; Bas, C.; Neyertz, S.; Albérola, N. D.; Petiaud, R.; Mercier, R. *Polymer* **2002**, *43*, 1983-1992.
(110) Pinel, E.; Barthe, M.-F.; De Baerdemaeker, J.; Mercier, R.; Neyertz, S.; Albérola, N. D.; Bas, C. *J. Polym. Sci.: Part B: Polym. Phys.* **2003**, *41*, 2998-3010.
(111) Pinel, E.; Mercier, R.; Sanchez-Marcano, J. G.; Neyertz, S.; Albérola, N. D.; Bas, C. *C. R. Chimie* **2003**, *6*.
(112) Bas, C.; Mercier, R.; Sanchez-Marcano, J.; Neyertz, S.; Albérola, N. D.; Pinel, E. *J. Polym. Sci.: Part B: Polym. Phys.* **2005**, *43*, 2413-2426.
(113) Ten Brinke, G.; Ausserre, D.; Hadziioannou, G. *J. Chem. Phys.* **1988**, *89*, 4374-4380.
(114) Bitsanis, I.; Hadziioannou, G. *J. Chem. Phys.* **1990**, *92*, 3827-3847.
(115) Vacatello, M. *Macromol. Theory Sim.* **2001**, *10*, 187-195.
(116) Kumar, S. K.; Vacatello, M.; Yoon, D. Y. *Macromolecules* **1990**, *23*, 2189-2197.
(117) Vacatello, M. *Macromol. Theory Sim.* **2002**, *11*, 53-57.
(118) Mischler, C.; Baschnagel, J.; Binder, K. *Advances in Colloid and Interface Science* **2001**, *94*, 197-227.
(119) Mansfield, K. F.; Theodorou, D. N. *Macromolecules* **1991**, *24*, 4295-4309.
(120) Mansfield, K. F.; Theodorou, D. N. *Macromolecules* **1991**, *24*, 6283-6294.
(121) Rallabandi, P. S.; Ford, D. M. *J. Memb. Sci.* **2000**, *171*, 239-252.
(122) Mansfield, K. F.; Theodorou, D. N. *Macromolecules* **1990**, *23*, 4430-4445.
(123) Jang, J. H.; Mattice, W. L. *Polymer* **1999**, *40*, 4685-4694.
(124) Jang, J. H.; Ozisik, R.; Mattice, W. L. *Macromolecules* **2000**, *33*, 7663-7671.
(125) Clancy, T. C.; Jang, J. H.; Dhinojwala, A.; Mattice, W. L. *J. Phys. Chem. B* **2001**, *105*, 11493-11497.
(126) Doruker, P.; Mattice, W. L. *Macromol. Theory Sim.* **2001**, *10*, 363-367.
(127) Jain, T. S.; de Pablo, J. J. *Macromolecules* **2002**, *35*, 2167-2176.

(128) Xu, G.; Mattice, W. L. *J. Chem. Phys.* **2003**, *118*, 5241-5247.
(129) Kikuchi, H.; Fukura, M. *KGK Kautschuk Gummi Kunststoffe* **2004**, *57*, 416-422.
(130) Jang, J. H.; Mattice, W. L. *Polymer* **1999**, *40*, 1911-1914.
(131) Clancy, T. C. *Polymer* **2004**, *45*, 7001-7010.
(132) Frankland, S. J. V.; Harik, V. M.; Odegard, G. M.; Brenner, D. W.; Gates, T. S. *Compos. Sci. Tech.* **2003**, *63*, 1655-1661.
(133) Vacatello, M. *Macromolecules* **2001**, *34*, 1946-1952.
(134) Vacatello, M. *Macromol. Theory Sim.* **2002**, *11*, 501-512.
(135) Vacatello, M. *Macromolecules* **2002**, *35*, 8191-8193.
(136) Vacatello, M. *Macromolecules* **2003**, *36*, 3411-3416.
(137) Vacatello, M. *Macromol. Theory Sim.* **2003**, *12*, 86-91.
(138) Starr, F. W.; Schrøder, T. B.; Glotzer, S. C. *Phys. Rev. E* **2001**, *64*, 021802.
(139) Starr, F. W.; Schrøder, T. B.; Glotzer, S. C. *Macromolecules* **2002**, *35*, 4481-4492.
(140) Starr, F.-W.; Douglas, J.-F.; Glotzer, S.-C. *J. Chem. Phys.* **2003**, *119*, 1777-1788.
(141) Smith, G.-D.; Bedrov, D.; Li, L.; Byutner, O. *J. Chem. Phys.* **2002**, *117*, 9478-9489.
(142) Smith, J. S.; Bedrov, D.; Smith, G. D. *Compos. Sci. Tech.* **2003**, *63*, 1599-1605.
(143) Brown, D.; Mélé, P.; Marceau, S.; Albérola, N. D. *Macromolecules* **2003**, *36*, 1395-1406.
(144) Brown, D.; Marceau, S.; Mélé, P.; Albérola, N. D. In *Proceedings of Eurofillers 2003, Sep 8-11*; Martínez, J. M. M., Ed.; The University of Alicante, Alicante, Spain, 2003.
(145) Trens, P.; Denoyel, R. *Langmuir* **1993**, *9*, 519-522.
(146) Bjelopavlic, M.; Singh, P. K.; El-Shall, H.; Moudgil, B. M. *J. Colloid Interface Sci.* **2000**, *226*, 159-165.
(147) Zaman, A. A.; Bjelopavlic, M.; Moudgil, B. M. *J. Colloid Interface Sci.* **2000**, *226*, 290-298.
(148) Zaman, A. A. *Colloid Polym. Sci.* **2000**, *278*, 1187-1197.
(149) Fu, Z.; Santore, M. M. *Langmuir* **1998**, *14*, 4300-4307.
(150) Huang, Y.; Santore, M. M. *Langmuir* **2002**, *18*, 2158-2165.
(151) Chen, C.-Y.; Even, M. A.; Wang, J.; Chen, Z. *Macromolecules* **2002**, *35*, 9130-9135.
(152) Badro, J.; Gillet, P.; Barrat, J.-L. *Europhys. Lett.* **1998**, *42*, 643-648.
(153) Van Beest, B. W. H.; Kramer, G. J.; van Santen, R. A. *Phys. Rev. Lett.* **1990**, *64*, 1955-1958.
(154) Brodka, A.; Zerda, T. W. *J. Chem. Phys.* **1996**, *104*, 6319-6326.
(155) Wypych, G. *Handbook of Fillers*, 2nd ed.; ChemTec Publishing & William Andrew Inc.: Toronto, Ontario, Canada and Norwich, NY, USA, 1999.
(156) Zhuravlev, L. T. *Colloids Surf. A: Physicochem. Eng. Aspects* **2000**, *173*, 1-38.
(157) Takahashi, Y.; Tadokoro, H. *Macromolecules* **1973**, *6*, 672-675.
(158) Chatani, Y.; Okamura, S. *Polymer* **1987**, *28*, 1815-1820.
(159) Fratini, A. V.; Cross, E. M.; Whitaker, R. B.; Adams, W. W. *Polymer* **1986**, *27*, 861-865.
(160) Iannelli, P. *Macromolecules* **1993**, *26*, 2309-2314.
(161) Weeks, J. J.; Clark, E. S.; Eby, R. K. *Polymer* **1981**, *22*, 1480-1486.
(162) Sugiyama, J., private communication ,1996.
(163) Kony, D.; Damm, W.; Stoll, S.; van Gunsteren, W. F. *J. Comput. Chem.* **2002**, *23*, 1416-1429.
(164) Fell, H. J.; Samuelsen, E. J.; Mårdalen, J.; Carlsen, P. H. J. *Synth. Met.* **1994**, *63*, 157-161.
(165) Mårdalen, J.; Samuelsen, E. J.; Gautun, O. R.; Carlsen, P. H. *Synth. Met.* **1992**, *48*, 1-18.

(166) Mårdalen, J.; Fell, H. J.; Samuelsen, E. J.; Bakken, E.; Carlsen, P. H. J.; Andersson, M. R. *Macromol. Chem. Phys.* **1995**, *196*, 553-565.
(167) Chen, T.-A.; Wu, X.; Rieke, R. D. *J. Am. Chem. Soc.* **1995**, *117*, 233-244.
(168) Clark, M.; Cramer III, R. D.; van Opdenbosch, N. *J. Comput. Chem.* **1989**, *10*, 982-1012.
(169) Vincent, C. A. *Prog. Solid State Chem.* **1987**, *17*, 145-261.
(170) Ratner, M. A.; Shriver, D. F. *Chem. Rev.* **1988**, *88*, 109-124.
(171) Gray, F. M. *Solid Polymer Electrolytes, Fundamentals and Technological Applications*; VCH: New York, 1991.
(172) Bruce, P. G.; Vincent, C. A. *J. Chem. Soc. Faraday Trans.* **1993**, *89*, 3187.
(173) Shriver, D. F.; Bruce, P. G. In *Solid State Electrochemistry*; Bruce, P. G., Ed.; Cambridge University Press: Cambridge, 1995; pp 95-118.
(174) Bruce, P. G.; Gray, F. M. In *Solid State Electrochemistry*; Bruce, P. G., Ed.; Cambridge University Press: Cambridge, 1995; pp 119-162.
(175) Gejji, S. P.; Tegenfeldt, J.; Lindgren, J. *Chem. Phys. Lett.* **1994**, *226*, 427-432.
(176) Huq, R.; Farrington, G. C.; Koksbang, R.; Tonder, P. E. *Solid State Ionics* **1992**, *57*, 277-283.
(177) MacCallum, J. R.; Smith, M. J.; Vincent, C. A. *Solid State Ionics* **1984**, *11*, 307.
(178) Booth, C.; Nicholas, C. V.; Wilson, D. J. In *Polymer Electrolyte Reviews-2*; MacCallum, J. R.; Vincent, C. A., Eds.; Elsevier: London, 1989; pp 229-254.
(179) Watanabe, M.; Ogata, N. In *Polymer Electrolyte Reviews-1*; MacCallum, J. R.; Vincent, C. A., Eds.; Elsevier: London, 1987; pp 39-68.
(180) MacCallum, J. R.; Vincent, C. A. In *Polymer Electrolyte Reviews-1*; MacCallum, J. R.; Vincent, C. A., Eds.; Elsevier: London, 1987; pp 23-37.
(181) Torell, L. M.; Schantz, S. In *Polymer Electrolyte Reviews-2*; MacCallum, J. R.; Vincent, C. A., Eds.; Elsevier: London, 1989.
(182) Wendsjö, Å.; Lindgren, J.; Thomas, J. O.; Farrington, G. C. *Solid State Ionics* **1992**, *53-56*, 1077-1082.
(183) Johansson, A.; Wendsjö, Å.; Tegenfeldt, J. *Electrochimica Acta* **1992**, *37*, 1487-1489.
(184) Farrington, G. C.; Linford, R. G. In *Polymer Electrolyte Reviews-2*; R., M. J.; A., V. C., Eds.; Elsevier: London, 1989; pp 255-284.
(185) Johansson, A.; Tegenfeldt, J. *Solid State Ionics* **1993**, *67*, 115-121.
(186) Lauenstein, Å.; Johansson, A.; Tegenfeldt, J. *J. Electrochem. Soc.* **1994**, *141*, 1819-1823.
(187) Yang, H.; Farrington, G. C. *J. Polym. Sci.: Part B: Polym. Phys.* **1993**, *31*, 157-163.
(188) Archer, W. L.; Armstrong, R. D. *Electrochim. Acta* **1980**, *25*, 1689.
(189) Müller-Plathe, F.; van Gunsteren, W. F. *J. Chem. Phys.* **1995**, *103*, 4745-4756.
(190) Müller-Plathe, F.; Liu, H.; van Gunsteren, W. F. *Comput. Polym. Sci.* **1995**.
(191) Ferreira, B. A.; Müller-Plathe, F.; Bernardes, A. T.; de Almeida, W. B. *Solid state ionics* **2002**, *147*, 361-366.
(192) Roe, R. J. *J. Phys. Chem.* **1968**, *72*, 2013.
(193) Van Krevelen, D. W. *Properties of polymers : their correlation with chemical structure; their numerical estimation and prediction from additive group contributions*, 3rd completely revised ed.; Elsevier: Amsterdam, 1990.
(194) Mark, J. E.; Flory, P. J. *J. Am. Chem. Soc.* **1965**, *87*, 1415.
(195) Abe, A.; Mark, J. E. *J. Am. Chem. Soc.* **1976**, *98*, 6468-6476.
(196) Müller-Plathe, F.; van Gunsteren, W. F. *Macromolecules* **1994**, *27*, 6040-6045.
(197) Killis, A.; Le Nest, J. F.; Cheradame, H.; Gandini, A. *Makromol. Chem.* **1982**, *183*, 2835.

(198) Ratner, M. A. In *Polymer Electrolyte Reviews-1*; MacCallum, J. R.; Vincent, C. A., Eds.; Elsevier: London, 1987; pp 173-236.
(199) Greenbaum, S. G. *Solid State Ionics* **1985**, *15*, 259-262.
(200) Wendsjö, Å. Ph-D Thesis, University of Uppsala, 1992.
(201) Dale, J. *Isr. J. Chem.* **1980**, *20*, 3.
(202) Gokel, G. W., Ed. *Crown Ethers and Cryptands*; The Royal Society of Chemistry: Cambridge, 1991.
(203) Fauteux, D.; Lupien, M. D.; Robitaille, C. D. *J. Electrochem. Soc.:Electrochemical Sci. Tech.* **1987**, *134*, 2761-2767.
(204) Chadwick, A. V.; Hanmer, P.; Coppola, L.; Ranieri, G.; Terenzi, M. *Solid State Ionics* **1994**, *72*, 147-151.
(205) Kakihana, M.; Schantz, S.; Torell, L. M. *J. Chem. Phys.* **1990**, *92*, 6271.
(206) Mehta, M. A.; Lightfoot, P.; Bruce, P. G. *Chem. of Materials* **1993**, *5*, 1338.
(207) *Polyimides: fundamentals and applications*; Marcel Dekker, Inc.: New York, 1996.
(208) Paul, D. R.; Yampolskii, Y. P., Eds. *Polymeric Gas Separation Membranes*; CRC Press: Boca Raton, FL, USA, 1994.
(209) McHattie, J. S.; Koros, W. J.; Paul, D. R. *Polymer* **1991**, *32*, 2618.
(210) Chen, K. M.; Wang, T. H.; King, J. S. *J. Applied Polym. Sci.* **1993**, *48*, 291-297.
(211) Fisher, J.; Lago, S. *J. Chem. Phys.* **1983**, *78*, 5750-5758.
(212) Cheung, P. S. Y.; Powles, J. G. *Mol. Phys.* **1975**, *30*, 921-949.
(213) Kang, J. W.; Choi, K.; Jo, W. H.; Hsu, S. L. *Polymer* **1998**, *39*, 7079-7087.
(214) Kotov, B. V. *Russian J. Phys. Chem.* **1988**, *62*, 1408-1417.
(215) LaFemina, J. P.; Arjavalingam, G.; Houghman, G. *J. Chem. Phys.* **1989**, *90*, 5154.
(216) Salley, J. M.; Frank, C. W. In *Polyimides: Fundamental and Applications*; Ghosh, M. K.; Mittal, K. L., Eds., 1996; p 279.
(217) Dinan, F. J.; Schwartz, W. T.; Wolfe, R. A.; Hojnicki, D. S.; Clair, T. S.; Pratt, J. R. *J. Polym. Sci: Part A: Polym. Chem.* **1992**, *30*, 111-118.
(218) Ando, S.; Matsuura, T.; Sasaki, S. *Polym. J.* **1997**, *29*, 69-76.
(219) Wachsman, E. D.; Frank, C. W. *Polymer* **1988**, *29*, 1191-1197.
(220) Viallat, A.; Bom, R. P.; Cohen-Addad, J.-P. *Polymer* **1994**, *35*, 2730-2736.
(221) Bondi, A. *Physical Properties of Molecular Crystals, Liquids and Gases*; John Wiley &Sons: New York, 1968.
(222) Tao, S. J. *J. Chem. Phys.* **1972**, *56*, 5499.
(223) Schrader, D. M.; Jean, Y. C. *Positron and Positronium Chemistry*; Elsevier: Amsterdam, 1988.
(224) Kruse, J.; Kanzow, J.; Rätzke, K.; Faupel, F.; Heuchel, M.; Frahn, J.; Hofmann, D. *Macromolecules* **2005**, *38*, 9638-9643.
(225) Yu, W. C.; Sung, C. *Macromolecules* **1988**, *21*, 365-371.
(226) Greenfield, M. L.; Theodorou, D. N. *Macromolecules* **1993**, *26*, 5461-5472.
(227) Lee, S.; Mattice, W. L. *Comp. Theor. Polym. Sci.* **1999**, *9*, 57-61.
(228) Nagel, C.; Schmidtke, E.; Günther-Schade, K.; Hofmann, D.; Fritsch, D. *Macromolecules* **2000**, *33*, 2242-2248.
(229) Schmitz, H.; Müller-Plathe, F. *J. Chem. Phys.* **2000**, *112*, 1040-1045.
(230) Raptis, V. E.; Economou, I. G.; Theodorou, D. N.; Petrou, J.; Petropoulos, J. H. *Macromolecules* **2004**, *37*, 1102-1112.
(231) Kim, T. H.; Koros, W. J.; Husk, G. R.; O'Brien, K. C. *J. Memb. Sci.* **1988**, *37*, 45-62.
(232) Kim, T. H.; Koros, W. J.; Husk, G. R. *Separation Sci. Tech.* **1988**, *23*, 1611-1626.
(233) Hougham, G.; Tesoro, G.; Viehbeck, A. *Macromolecules* **1996**, *29*, 3453-3456.
(234) Simpson, J. O.; St-Clair, A. K. *Thin Solid Films* **1997**, *308-309*, 480-485.

(235) Lee, J. F.; Sears, F. W.; Turcotte, D. L. *Statistical thermodynamics, 2nd ed.*; Addison-Wesley: Reading, MA, 1973.
(236) Gusev, A. A.; Müller-Plathe, F.; van Gunsteren, W. F.; Suter, U. W. *Advances in Polym. Sci.* **1994**, *116*, 207-247.
(237) Greenfield, M. L.; Theodorou, D. N. *Macromolecules* **1998**, *31*, 7068-7090.
(238) Müller-Plathe, F.; Rogers, S. C.; van Gunsteren, W. F. *Macromolecules* **1992**, *25*, 6722-6724.
(239) Müller-Plathe, F. *J. Chem. Phys.* **1992**, *96*, 3200-3205.
(240) Müller-Plathe, F.; Rogers, S. C.; van Gunsteren, W. F. *J. Chem. Phys.* **1993**, *98*, 9895-9904.
(241) Koros, W. J.; Paul, D. R.; Rocha, A. A. *J. Polym. Sci., Polym. Phys. Ed.* **1976**, *14*, 687-702.
(242) Paul, D. R.; Koros, W. J. *J. Polym. Sci., Polym. Phys. Ed.* **1976**, *14*, 675-685.
(243) Widom, B. *J. Chem. Phys.* **1963**, *39*, 2808-2812.
(244) Tanaka, K.; Kita, H.; Okano, M.; Okamoto, K. I. *Polymer* **1992**, *33*, 585-592.
(245) Tanaka, K.; Osada, Y.; Kita, H.; Okamoto, K.-I. *J. Polym. Sci.: Part B: Polym. Phys.* **1995**, *33*, 1907-1915.
(246) Coleman, M. R.; Koros, W. J. *J. Memb. Sci.* **1990**, *50*, 285-297.
(247) Ayala, D.; Lozano, A. E.; De Abajo, J.; García-Perez, C.; De la Campa, J. G.; Peinemann, K.-V.; Freeman, B. D.; Prabhakar, R. *J. Memb. Sci.* **2003**, *215*, 61-73.
(248) Saiz, E.; Gonzalez, M. M. L.; Riande, E.; Guzman, J.; Compan, V. *Phys. Chem. Chem. Phys.* **2003**, *5*, 2862-2868.
(249) Stern, S. A. *J. Memb. Sci.* **1994**, *94*, 1-65.
(250) Yamamoto, H.; Mi, Y.; Stern, S. A.; St-Clair, A. K. *J. Polym. Sci., Part B: Polym. Phys.* **1990**, *28*, 2291-2304.
(251) Cuthbert, T. R.; Wagner, N. J.; Paulaitis, M. E.; Murgia, G.; D'Aguanno, B. *Macromolecules* **1999**, *32*, 5017-5028.
(252) Müller-Plathe, F.; Rogers, S. C.; van Gunsteren, W. F. *Chem. Phys. Lett.* **1992**, *199*, 237-243.
(253) Boshoff, J. H. D.; Lobo, R. F.; Wagner, N. J. *Macromolecules* **2001**, *34*, 6107-6116.
(254) McQuarrie, D. A. *Statistical Mechanics*; Harper and Row: New York, 1976.
(255) Gray-Weale, A. A.; Henchman, R. H.; Gilbert, R. G.; Greenfield, M. L.; Theodorou, D. N. *Macromolecules* **1997**, *30*, 7296-7306.
(256) Li, Y.; Wang, X.; Ding, M.; Xu, J. *J. Applied Polym. Sci.* **1996**, *61*, 741-748.
(257) Weber, H.; Paul, W. *Phys. Rev. E* **1996**, *54*, 3999-4007.
(258) Cuthbert, T. R.; Wagner, N. J.; Paulaitis, M. E. *Macromolecules* **1997**, *30*, 3058-3065.
(259) Jia, L.; Xu, J. *Polym. J.* **1991**, *23*, 417-425.
(260) Li, Y.; Ding, M.; Xu, J. *Macromol. Chem. Phys.* **1997**, *198*, 2769-2778.
(261) Suzuki, T.; Yamada, Y.; Tsujita, Y. *Polymer* **2004**, *45*, 7167-7171.
(262) Mensitieri, G.; Del Nobile, M. A.; Monetta, T.; Nicodemo, L.; Bellucci, F. *J. Memb. Sci.* **1994**, *89*, 131-141.
(263) Shishatskii, A. M.; Yampolskii, Y. P.; Peinemann, K.-V. *J. Memb. Sci.* **1996**, *112*, 275-285.
(264) Kawakami, H.; Mikawa, M.; Nagaoka, S. *J. Memb. Sci.* **1997**, *137*, 241-250.
(265) Kawakami, H.; Mikawa, M.; Nagaoka, S. *Macromolecules* **1998**, *31*, 6636-6638.
(266) McCaig, M. S.; Paul, D. R. *Polymer* **2000**, *41*, 629-637.
(267) McCaig, M. S.; Paul, D. R.; Barlow, J. W. *Polymer* **2000**, *41*, 639-648.
(268) Pfromm, P. H.; Koros, W. J. *Polymer* **1995**, *36*, 2379-2387.
(269) Huang, Y.; Paul, D. R. *Polymer* **2004**, *45*, 8377-8393.

(270) Dimitrakopoulos, C. D.; Kowalczyk, S. P. *Thin Solid Films* **1997**, *295*, 162-168.
(271) Smith, K. A.; Vladkov, M.; Barrat, J.-L. *Macromolecules* **2005**, *38*, 571-580.
(272) Helfand, E.; Tagami, Y. *J. Chem. Phys.* **1972**, *56*, 3592-3601.
(273) Helfand, E.; Tagami, Y. *J. Chem. Phys.* **1972**, *57*, 1812-1813.
(274) Izumisawa, S.; Jhon, M. S. *J. Chem. Phys.* **2002**, *117*, 3972-3977.
(275) Torres, J. A.; Nealey, P. F.; De Pablo, J. J. *Phys. Rev. Lett.* **2000**, *85*, 3221-3224.
(276) Crank, J. C. *The Mathematics of Diffusion*; Oxford University Press: Oxford, 1979 (2nd edition).
(277) Tsige, M.; Grest, G. S. *J. Chem. Phys.* **2004**, *120*, 2989-2995.
(278) Klopffer, M. H.; Flaconnèche, B. *Oil & Gas Sci. Tech. - Rev. IFP* **2001**, *56*, 223-244.
(279) Flaconnèche, B.; Martin, J.; Klopffer, M. H. *Oil & Gas Sci. Tech. - Rev. IFP* **2001**, *56*, 245-259.
(280) Van der Vegt, N. F. A.; Briels, W. J.; Wessling, M.; Strathmann, H. *J. Chem. Phys.* **1996**, *105*, 8849-8857.
(281) Van der Vegt, N. F. A. *J. Memb. Sci.* **2002**, *205*, 125-139.
(282) Halgren, T. A. *J. Am. Chem. Soc.* **1992**, *114*, 7827-7843.
(283) Barrat, J.-L.; Vos, W. L. *J. Chem. Phys.* **1992**, *97*, 5707-5712.
(284) Dlubek, G.; Buchhold, R.; Hubner, C.; Nakladal, A. *Macromolecules* **1999**, *32*, 2348-2355.
(285) Moylan, C. R.; Best, M. E.; Ree, M. *J. Polym. Sci.: Part B: Polym. Phys.* **1991**, *29*, 87-92.
(286) Knopp, B.; Suter, U. W. *Macromolecules* **1997**, *30*, 6114-6119.
(287) Knopp, B.; Suter, U. W.; Gusev, A. A. *Macromolecules* **1997**, *30*, 6107-6113.
(288) Nick, B.; Suter, U. W. *Comput. Theor. Polym. Sci.* **2001**, *11*, 49-55.
(289) Berendsen, H. J. C.; Grigera, J. R.; Straatsma, T. P. *J. Phys. Chem.* **1987**, *91*, 6269.
(290) Ronova, I. A.; Rozhkov, E. M.; Alentiev, A. Y.; Yampolskii, Y. P. *Macromol. Theory Sim.* **2003**, *12*, 425-439.
(291) Goudeau, S.; Charlot, M.; Vergelati, C.; Müller-Plathe, F. *Macromolecules* **2004**, *37*, 8072-8081.
(292) Lim, B. S.; Nowick, A. S.; Lee, K.-W.; Viehbeck, A. *J. Polym. Sci.: Part B: Polym. Phys.* **1993**, *31*, 545-555.
(293) Bas, C.; Albérola, N. D.; Tamagna, C.; Pascal, T. *CR Acad. Sci.* **1999**, *t327, Série IIb*, 1095-1100.
(294) Müller-Plathe, F. *J. Chem. Phys.* **1998**, *108*, 8252-8263.
(295) Van Alsten, J. G.; Coburn, J. C. *Macromolecules* **1994**, *27*, 3746-3752.
(296) Xu, X. L.; Yuehui, Y.; Zixin, L.; Lizhi, C.; Fang, F.; Zuyao, Z.; Shichang, Z.; Gendi, D.; Guanqun, X. *Nuclear Instruments & Methods in Physics Research, Section B (Beam Interactions with Materials and Atoms)* **1991**, *B59-b60*, 1267-1270.
(297) Li, S. Z.; Chen, R. S.; Greenbaum, S. G. *J. Polym. Sci.: Part B: Polym. Phys.* **1995**, *33*.
(298) Waters, J. F.; Likavec, W. R.; Ritchey, W. M. *J. Applied Polym. Sci.* **1994**, *53*, 59-70.
(299) Goudeau, S.; Charlot, M.; Müller-Plathe, F. *J. Phys. Chem. B* **2004**, *108*, 18779-18788.
(300) Gaudichet-Maurin, E.; Ph-D Thesis, ENSAM-Paris, 2005.
(301) Müller-Plathe, F.; van Gunsteren, W. F. *Polymer Guildford* **1997**, *38*, 2259-2268.
(302) Müller-Plathe, F. *J. Membrane Sci.* **1998**, *141*, 147-154.
(303) Hahn, O.; Mooney, D. A.; Müller-Plathe, F.; Kremer, K. *J. Chem. Phys.* **1999**, *111*, 6061-6068.
(304) Odegard, G. M.; Clancy, T. C.; Gates, T. S. *Polymer* **2005**, *46*, 553-562.

(305) Shantalii, T. A.; Karpova, I. L.; Dragan, K. S.; Privalko, E. G.; Privalko, V. P. *Sci. Tech. of Advanced Mat.* **2003**, *4*, 115-119.
(306) Napper, D. H. *Polymeric Stabilization of Colloidal Dispersions*; Academic Press, New York, 1983.
(307) Fleer, G. J.; Stuart, M. A. C.; Scheutjens, J. M. H. M.; Cosgrove, T.; Vincent, B. *Polymers at Interfaces*; Chapman and Hall, London, 1993.
(308) Mathur, S.; Brij, M.-M. *J. Colloid Interface Sci.* **1997**, *196*, 92-98.
(309) Lafuma, F.; Wong, K.; Cabane, B. *J. Colloid Interface Sci.* **1991**, *143*, 9-21.
(310) Liu, S. F.; Legrand, V.; Gourmand, M.; Lafuma, F.; Audebert, R. *Colloids Surf. A: Physicochem. Eng. Aspects* **1996**, *111*, 139-146 [137 p.].
(311) Chaplain, V.; Janex, M. L.; Lafuma, F.; Graillat, C.; Audebert, R. *Colloid Polym. Sci.* **1995**, *273*, 984-993.
(312) Van der Beek, G. P.; Cohen Stuart, M. A.; Cosgrove, T. *Langmuir* **1991**, *7*, 327.
(313) Van der Beek, G. P.; Cohen Stuart, M. A.; Fleer, G. J.; Hofman, J. E. *Macromolecules* **1991**, *24*, 6600-6611.
(314) Cosgrove, T.; Griffiths, P. C.; Lloyd, P. M. *Langmuir* **1995**, *11*, 1457-1463.
(315) Neel, O.; Ducouret, G.; Lafuma, F. *J. Colloid Interface Sci.* **2000**, *230*, 244-253.
(316) Dijt, J. C.; Stuart, M. A. C.; Fleer, G. J. *Macromolecules* **1994**, *27*, 3219-3228.
(317) Griffiths, P. C.; Stilbs, P. *Langmuir* **1995**, *11*, 898-904.
(318) Fu, Z.; Santore, M. M. *Macromolecules* **1998**, *31*, 7014-7022.
(319) Wind, B.; Killmann, E. *Colloid Polym. Sci.* **1998**, *276*, 903-912.
(320) Mubarekyan, E.; Santore, M.-M. *Macromolecules* **2001**, *34*, 4978-4986.
(321) Barbier, D. In *DEA report*; University of Savoie, 2003.
(322) Eliassi, A.; Modarress, H.; Mansoori, G. A. *J. Chem. Eng. Data* **1998**, *43*, 719-721.
(323) *Polymer Handbook (3rd Edition)*; Wiley-Interscience: New York, 1989.
(324) Borodin, O.; Smith, G. D.; Bandyopadhyaya, R.; Byutner, O. *Macromolecules* **2003**, *36*, 7873-7883.
(325) Hasan, F. B.; Huang, D. D. *J. Colloid Interface Sci.* **1997**, *190*, 161-170.
(326) Zhang, Q.; Archer, L. A. *Langmuir* **2002**, *18*, 10435-10442.
(327) Costantino, M. L.; Fiore, G. B. *Medical Engineering & Physics* **1997**, *19*, 157-163.
(328) Lanczos, C. *SIAM J. Numer. Anal.* **1964**, *B1*, 86–96.
(329) Barbier, C. In *Master M2 report*; University of Savoie, 2005.
(330) Fisher, V.; Borchard , W. *J. Phys. Chem. B* **2000**, *104*, 4463-4470.
(331) Lin, H.; Wagner, E. V.; Freeman, B. D.; Toy, L. G.; Gupta, R. P. *Science* **2006**, *311*, 639-642.
(332) Wick, C. D.; Siepmann, J. I.; Theodorou, D. N. *J. Am. Chem. Soc.* **2005**, *127*, 12338-12342.
(333) Fried, J. R.; Hu, N. *Polymer* **2003**, *44*, 4363-4372.
(334) Hirayama, Y.; Yoshinaga, T.; Kusuki, Y.; Ninomiya, K.; Sakakibara, T.; Tamari, T. *J. Memb. Sci.* **1996**, *111*, 169-182.
(335) Thran, A.; Kroll, G.; Faupel, F. *J. Polym. Sci.: Part B: Polym. Phys.* **1999**, *37*, 3344-3358.
(336) Bos, A.; Pünt, I. G. M.; Wessling, M.; Strathmann, H. *J. Memb. Sci.* **1999**, *155*, 67-78.
(337) Kim, K.-J.; Park, S.-H.; So, W.-W.; Ahn, D.-J.; Moon, S.-J. *J. Memb. Sci.* **2003**, *211*, 41-49.
(338) Stern, S. A.; Liu, Y.; Feld, W. A. *J. Polym. Sci.: Part B: Polym. Phys.* **1993**, *31*, 939-951.
(339) Robeson, L. M.; Smith, C. D.; Langsam, M. *J. Memb. Sci.* **1997**, *132*, 33-54.
(340) Alentiev, A. Y.; Loza, K. A.; Yampolskii, Y. P. *J. Memb. Sci.* **2000**, *167*, 91-106.

(341) Aitken, C. L.; Koros, W. J.; Paul, D. R. *Macromolecules* **1992**, *25*, 3424-3434.
(342) Baschnagel, J.; Binder, K.; Doruker, P.; Gusev, A. A.; Hahn, O.; Kremer, K.; Mattice, W. L.; Müller-Plathe, F.; Murat, M.; Paul, W.; Santos, S.; Suter, U. W.; Tries, V. *Advances Polym. Sci.* **2000**, *152*, 41-156.
(343) Reith, D.; Meyer, H.; Müller-Plathe, F. *Macromolecules* **2001**, *34*, 2335-2345.
(344) Faller, R.; Müller-Plathe, F. *Polymer Guildford* **2002**, *43*, 621-628.
(345) León, S.; van der Vegt, N. F. A.; Delle Site, L.; Kremer, K. *Macromolecules* **2005**, *38*, 8078-8092.
(346) Hess, B.; León, S.; van der Vegt, N. F. A.; Kremer, K. *Soft Matter* **2006**, *accepted*.